**Title**

3D Modeling of Pulse-Echo Ultrasonic Data and Drilling of Impact-Damaged Composite Laminates for Injection Repair



**ISBN**

9798190935868

**Author**

Valerio, Christopher

**Publication Date**

2026-09-15

Peer reviewed|Thesis/dissertation

UNIVERSITY OF CALIFORNIA SAN DIEGO

# 3D Modeling of Pulse-Echo Ultrasonic Data and Drilling of Impact-Damaged Composite Laminates for Injection Repair

A Thesis submitted in partial satisfaction of the requirements
for the degree Master of Science

Structural Engineering

by

Christopher Valerio

Committee in charge:

Professor Hyonny Kim, Chair
Professor Francesco Lanza Di Scalea
Professor Kenneth Loh

2026

The Thesis of Christopher Valerio is approved, and it is acceptable in quality and form for publication on microfilm and electronically.

University of California San Diego

2026

# DEDICATION

In memory of my two grandmothers, María del Socorro Farfán Pucheta and María del Socorro Martínez López, who survived the unimaginable and raised their families in spite of it all

May they rest in peace.

TABLE OF CONTENTS

LIST OF FIGURES

# LIST OF TABLES

LIST OF ABBREVIATIONS

| | |
|---|---|
| BVID | Barely Visible Impact Damage |
| CAD | Computer Aided Design |
| CFRP | Carbon Fiber Reinforced Polymers |
| GFRPP | Glass Fiber Reinforced Polypropylene |
| DID | Drilling Induced Damage |
| HVI | High Velocity Impact |
| LVI | Low Velocity Impact |
| DNB | Damage Network Branch |
| NDE | Nondestructive Evaluation |
| PZT | Piezoelectric Transducer |
| PEUT | Pulse-Echo Ultrasonic Testing |
| TDR | Tapered Drill-Reamer |
| TOF | Time of Flight |
| $\Delta$TOF | Time of Flight Difference |

ACKNOWLEDGEMENTS

First and foremost, I would like to thank you, Professor Hyonny Kim, for your unwavering support. Thank you for welcoming me into your laboratory in the summer of 2024 when I was still figuring things out and for your continued support thereafter. Thank you for believing in me when I needed it most — this thesis would not have been possible without you. More importantly, thank you for being a truly exceptional mentor, of a kind that is increasingly rare. Your patience and ability to bring the best out of me are qualities I hope to carry with me for the rest of my life and use them when my time to mentor others comes. There is so much more I could thank you for, but above all, thank you for being such a genuine and caring person — not just with me, but with everyone in the team.

I would also like to thank Hiruni Perera. Hiruni, thank you for your continued support throughout the course of this work. Thank you for allowing me to contribute to your project and for mentoring me when I was just getting started. In particular, thank you for always being so kind, thoughtful, and supportive. You have a way of viewing life with a rare and refreshing honesty that I deeply admire. Thank you for guiding me and treating me as a member of your team during my time at the Materials Lab at the Fleet Readiness Center Southwest (FRCSW). The conversations we have shared have been truly meaningful. Thank you for being a great mentor and a great friend.

To Alyssa Zamora. Alyssa, thank you for being a great leader. Your flexibility and honest feedback allowed me to get the most out of my internship at the Materials Lab. Thank you for everything you taught me during my time as an intern and for allowing me to visit the lab on a few occasions afterward. Your support and collaboration were paramount in the development of this work, and I cannot thank you enough. Your curiosity and commitment are qualities I hope to carry with me for the rest of my life. Similarly, I would like to thank the rest of the team at the Materials

Lab at FRCSW. Thank you, Steve Pacheco, Marco Martínez, Omar Medina, Luis Sánchez, John Schneider, Nick Candrella, Clarissa O'Malley, and everyone else on the team who made my time at as in intern memorable.

I would also like to thank Mac Delaney. Thank you for teaching me how to use the C-scanner and for sharing your knowledge of ultrasonic testing. It is important to acknowledge that a significant portion of this work builds upon your work on pulse-echo ultrasonic testing. Thank you for trusting me and, more importantly, thank you for always being so helpful. I cannot count how many times I asked you to walk me through the C-scanner, and every time you were as thorough and patient as the first — qualities I hope to embody as a mentor myself. Similarly, I would like to thank Jessica Chan for her work on 3D modeling of pulse-echo ultrasonic testing. Jessica, your ingenuity has prevailed throughout the years and your work paved the way for promising advances in the world of composites.

Moreover, I would like to thank everyone in the composite research group at UC San Diego. Saeed, although not directly involved in this research, you have taught me countless things that supported my work over the years, and for that I am truly grateful. Jusung and Kelly, dream team! Thank you for your patience and flexibility in accommodating my tight schedule during our hail impact project; more importantly, however, thank you for your friendship — it has been an honor working with you. Finally, thank you, Mathew Tu, for your resourcefulness and kindness; I am glad to count you as a colleague and friend.

Thank you to Professor Francesco Lanza Di Scalea and Professor Kenneth Loh for their willingness to be in my defense committee.

Above all, thank you to my family. Dad, Mom, Karla, Roberto, Ximena, Sofia, Yahel, Lia, Ricardo, Grandma Soco, and Grandma Coco, thank you for always believing in me.

ABSTRACT OF THE THESIS

3D Modeling of Pulse-Echo Ultrasonic Data and Drilling of Impact-Damaged Composite Laminates for Injection Repair

by

Christopher Valerio

Master of Science in Structural Engineering

University of California San Diego, 2026

Professor Hyonny Kim, Chair

One of the most common types of damage in composite laminates is delamination. This type of damage occurs when the plies within the material separate, reducing the strength and, if ignored, possibly leading to structural failure. The repair of these materials is costly and limited by tool availability, which motivated the adaptation of a repair technique known as injection repair

for strength-restoring applications. The goal of this work is twofold: first, to develop a data processing and visualization computational tool that generates three-dimensional maps and delamination density plots from ultrasonic pulse-echo C-scan data, which would be used to assist in identifying percolation pathways within an damaged composite material; and second, to develop a drilling process that produces favorable hole geometry for resin penetration into delaminations while minimizing drilling-induced damage and debris accumulation. The drilling process incorporates carefully selected drilling tools to achieve the desired geometry, tailored drilling parameters to prevent further damage, and a customized vacuum jig for debris mitigation. In parallel, the computational code uses C-scan data to generate three-dimensional maps of internal damage. Moreover, when both front- and back-side C-scan data are available, the code combines them into a single hybrid three-dimensional reconstruction. This three-dimensional data reconstruction also enables identification of the damage network branches within the composite via delamination density maps. The delamination network branches serve as optimal hole locations for resin injection, while the developed drilling methods help mitigate drilling-induced damage and debris contamination, thereby improving percolation efficiency and contributing to the development of injection repair.

# CHAPTER 1: INTRODUCTION

## 1.1 Scope

The scope of this work is to provide an intuitive way of visualizing internal damage on impacted laminated composites by creating plots that highlight key features of a damage network. Additionally, this work aims to provide a description of the tools, settings, and setup used for the drilling of impacted carbon fiber reinforced polymer (CFRP) composites to mitigate drilling-induced damage and debris contamination. Injection repair consists of five main steps, illustrated in Figure 1.1, namely: 1) performing non-destructive evaluations on the impacted composite — in this case, ultrasonic pulse-echo testing, 2) processing the ultrasonic testing data to generate maps of damage inside the composite, 3) using the processed 3D hybrid data to make engineered decisions on hole placement, 4) drilling the parts based on the sketched layouts, and 5) injecting the drilled composites with a repair resin.

This thesis provides novel contributions to steps 2, 3, and 4 in the repair process in pursuit of optimizing drilling and hole placement to contribute to the adaptation and qualification of injection repair for structural applications. Notably, the work presented in this thesis does not prove that injection repair successfully restores strength and refills delaminations; instead, it provides scientifically derived practical and analytical improvements to the repair process that represent an advancement over current practices. The drilled and scanned composite specimens were fabricated and impacted to resemble a section of a real aircraft airframe damaged during service, which inherently consists of varying laminate layups and impact damage distributions, such that the drilling, scanning, and injection repair experiments are more directly translatable into real-world applications.

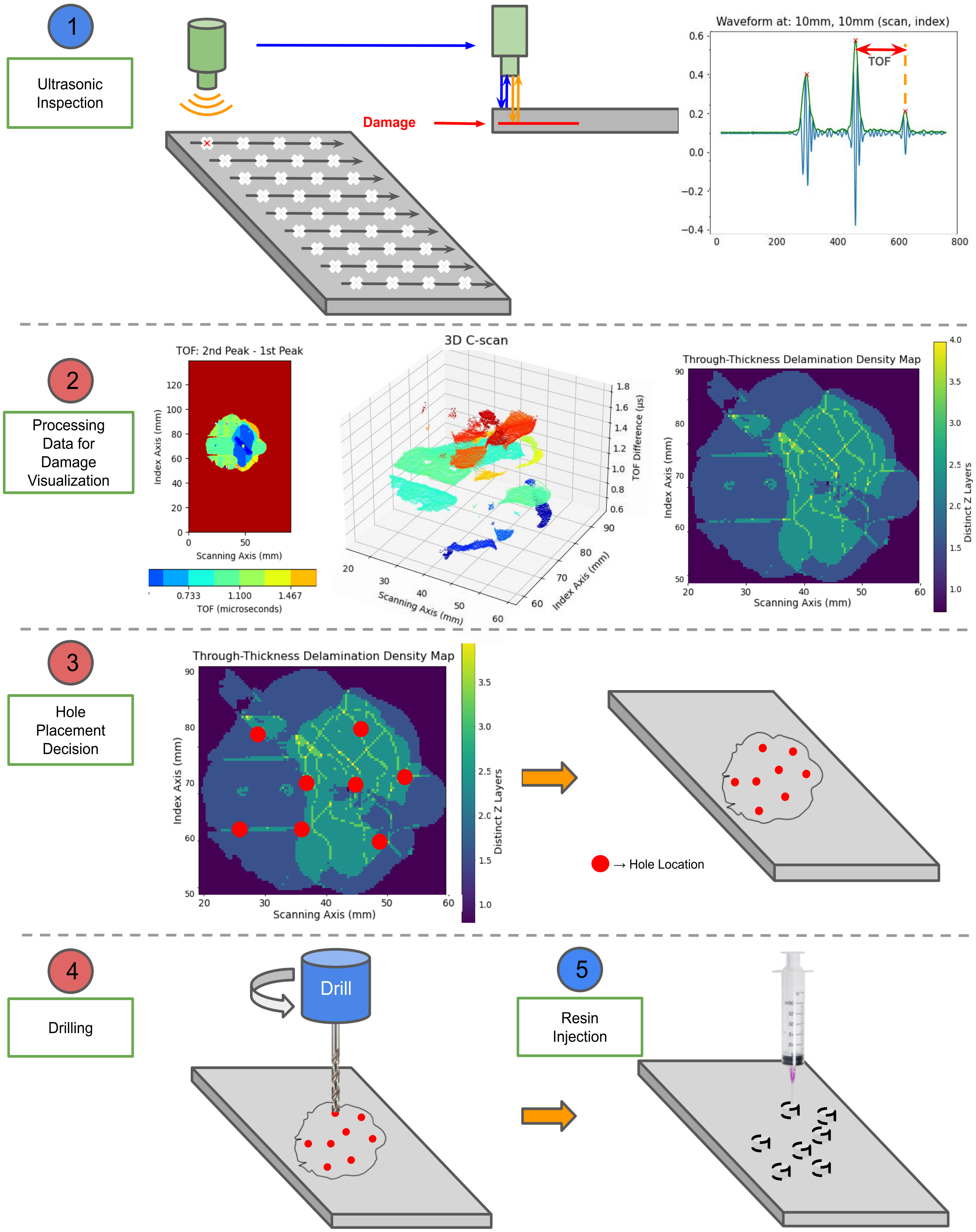


Figure 1.1 Ultrasound data visualization informed injection repair overview steps.

## 1.2 Motivation

The most common repair methods for damaged composite structures are flush-type bonded scarf patch repairs and bolted joints. However, these repair types — bonded repairs in particular — require specialized tools and a high level of analysis that are not always available, especially during field operations where personnel may lack the necessary technical and practical skills to perform such repairs. Considering this, injection repair presents an alternative: a fast, simple, and reliable method that can be carried out with readily accessible tools and requires comparatively lower technical expertise. However, injection repair is not yet considered as a structural repair, as there is insufficient scientific evidence of the method's efficacy in refilling delaminations and restoring strength.

This gap has brought scientists together in a collaborative effort toward qualifying injection repair for structural applications. The drilling experiments presented in this thesis were performed to provide a better understanding of the tools and settings used in order to optimize hole quality for injection, while the development of the Python code was conducted to advance the understanding of pulse-echo ultrasonic testing methods and to produce visualizations of delamination networks within impacted composite materials. Notably, the work presented in this thesis, while relevant across a range of applications, places particular emphasis on advancing injection repair toward strength-restoring qualification.

## 1.3 Background

Laminated composites possess high strength-to-weight properties that make them ideal for aerospace applications where weight reduction is critical. However, despite their outstanding mechanical performance, these materials present several disadvantages, including processing and damage complexity. Due to their anisotropic nature, composites are susceptible to out-of-plane loading conditions such as impact loads. Particularly, laminated composites are prone to a type of damage known as delamination, occurring when adjacent plies within the composite separate, creating severe stress concentrations and reducing the overall strength of a structure.

Because of their poor response to transverse loading, drilling of composite materials presents significant challenges. Unlike isotropic and homogeneous materials, the mechanical behavior of composites under drilling can give rise to drilling-induced defects such as ply peel-up and ply push-down (Wei et al., 2013), demonstrated in Figure 1.2. Additionally, other common damage types may appear, including matrix cracking, ply collapse, fraying, and burrs. Figure 1.3 shows examples of drilled hole cross-sections exhibiting signs of drilling-induced damage.

When transverse impact does occur, it often manifests as Barely Visible Impact Damage (BVID), meaning it cannot be readily detected from the surface via visual inspection (Chan, 2023). Therefore, nondestructive evaluation (NDE) techniques are required to locate damage within a composite and facilitate preventative repairs. One powerful NDE technique is pulse-echo ultrasonic testing, in which an ultrasonic wave is transmitted by a piezoelectric transducer (PZT) through a structure and reflected to the sensor upon reaching either the back surface or any internal imperfection (e.g., delamination). This reflection occurs due to a phenomenon known as impedance mismatch, which takes place when the dynamic stiffness of two adjacent materials differs significantly. In pulse-echo ultrasonic testing, the impedance mismatch typically occurs between the scanned material and air/vacuum. By measuring the time-of-flight (TOF) — the time required for the wave to travel and return to the PZT — color-coded plots can be generated to illustrate the spatial distribution of potential damage, which corresponds to reduced TOF values, as shown in Figure 1.4.

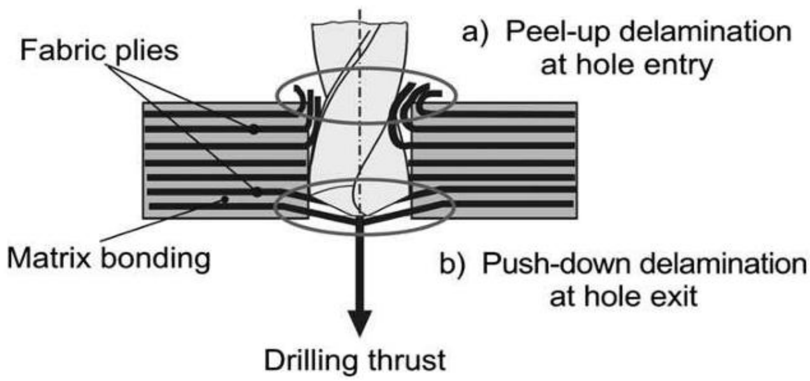


Figure 1.2 Drilling-induced composite delamination: a) ply peel-up, and b) ply push-down (Wei et al., 2013).

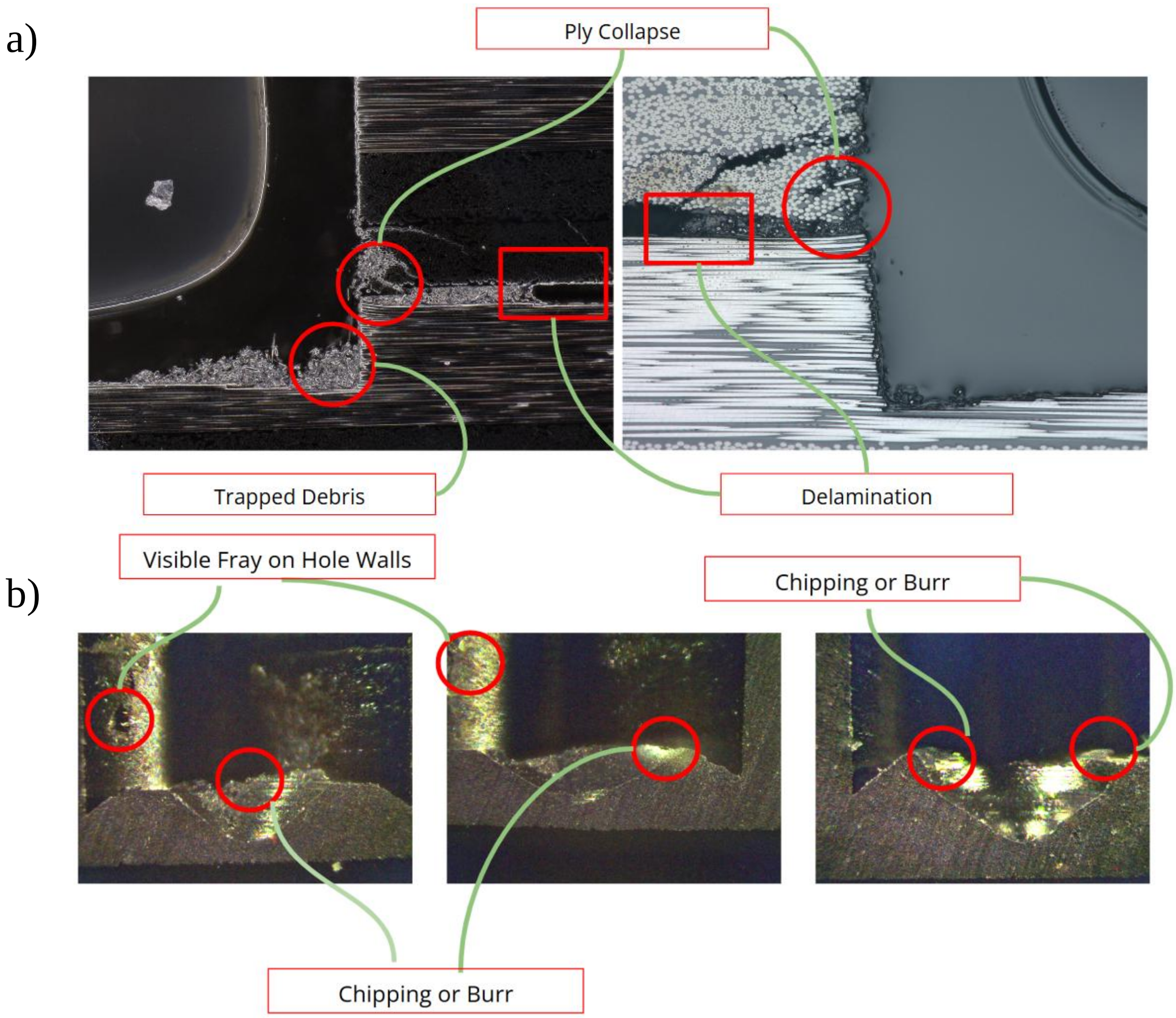


Figure 1.3 Drilling-induced defects: a) Ply collapse and debris buildup, and b) surface finish defects (Photos by Alyssa Zamora and Christopher Valerio).

a)

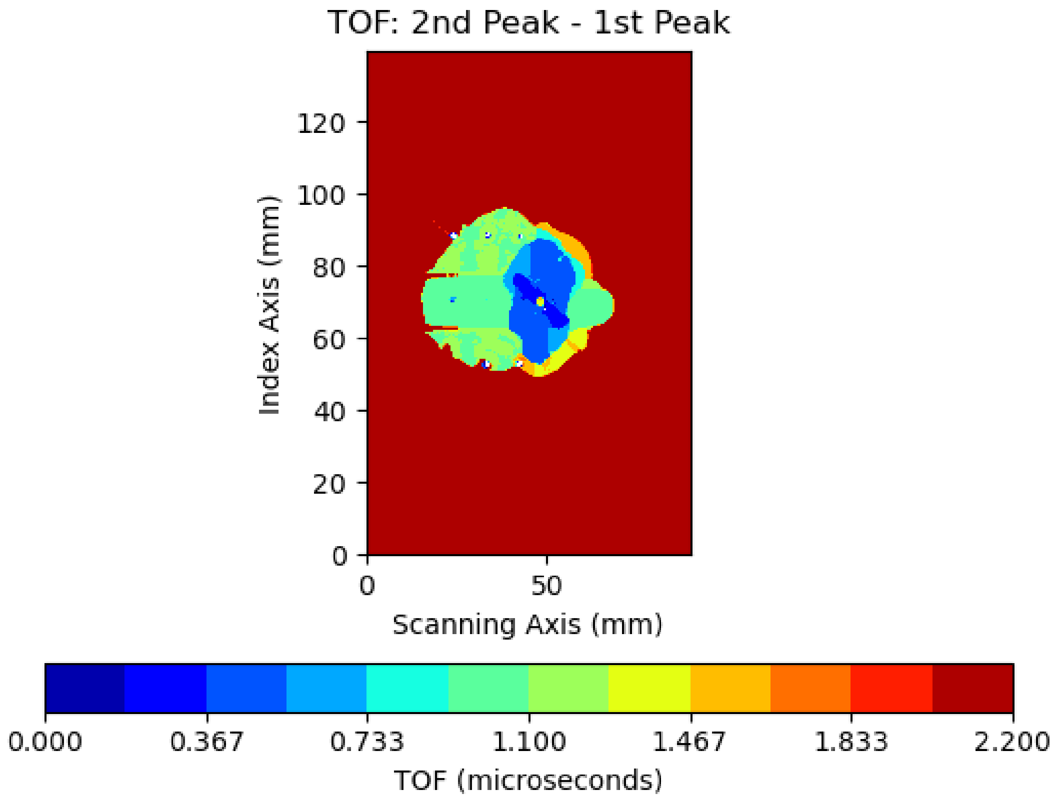


b)

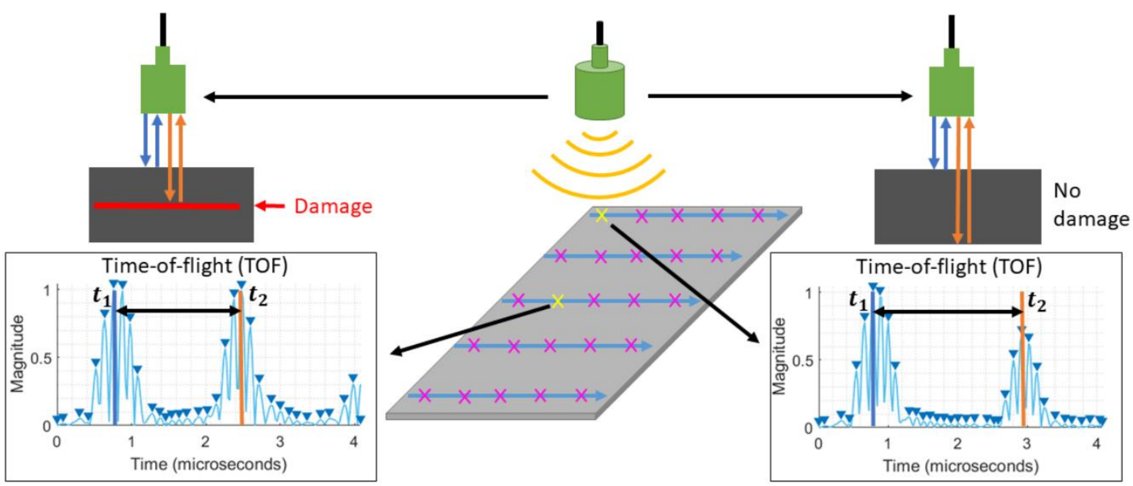


Figure 1.4 Pulse-echo ultrasonic testing: a) 2D C-Scan plot, b) pulse-echo ultrasonic testing diagram (Chan, 2023).

## 1.4 Previous Work

Previous work has been done by other researchers to help improve the injection repair method for structural applications. Justin Massey developed a new quantitative internal surface cleaning, preparation, and repair process for delaminated composite materials to address questions about quantifying the removal of internal contamination, strength restoration, and ideal repair resin fill percentage (Massey, 2023). Massey conducted injection repair experiments on lab-delaminated coupons, evaluating different hole patterns and depths, and suggested further drilling experiments using reamer bits to reduce drilling debris. In a complementary effort, Hiruni Perera (2025) conducted a comprehensive investigation into commercially available off-the-shelf epoxies with low viscosity and suitable service temperature. Perera characterized and compared the material and mechanical properties of several resins including shear strength, glass transition temperature (Tg), viscosity, and porosity. Both Massey and Perera set the foundation for the development of injection repair for structural applications, which utilizes standards established by Massey and the repair resin selected by Perera.

In parallel, Jessica Chan (2022) developed a MATLAB code that processes ultrasonic pulse-echo C-scans, using unique characteristics to create a map of boundaries where the damage changes from one layer to another. Chan's code is also able to generate 3D reconstructions of delamination and, if available, combine front and back side C-scans into a hybrid C-scan. Two of the biggest challenges Chan faced in the development of the hybrid scans were damage selection and data alignment which she solved with laborious segmentation techniques and manual data shifts, respectively. The development of the Python code in this thesis was inspired by Chan's work with the goal of optimizing damage selection, data alignment, runtime, and ultimately use the 3D reconstructions to aid with the placement of holes for injection repair.

## 1.5 Literature Review

### 1.5.1 Taper Drill-Reamer for Composite Drilling

As suggested by Massey (2023), a taper drill-reamer (TDR) poses promising characteristics to reduce debris generation, improve surface finish, and most importantly, minimize drilling-induced delamination. Liu and Li (2021) explored a scale-modeling method to simulate the structural mechanical responses and dynamic failure behavior of CFRP composites under drilling with a TDR. The results from their study align with other literature, which indicate the strong effect of feed rate in the minimization of thrust force, torque, burr, and delamination formation. Furthermore, Liu and Huang (2024) performed response surface regression models for parameter optimization, showing that minimum thrust force using a TDR is achieved at high spindle speeds (4,879 rpm) and low feed rates (34.04 mm/min), as shown in Figure 1.5.

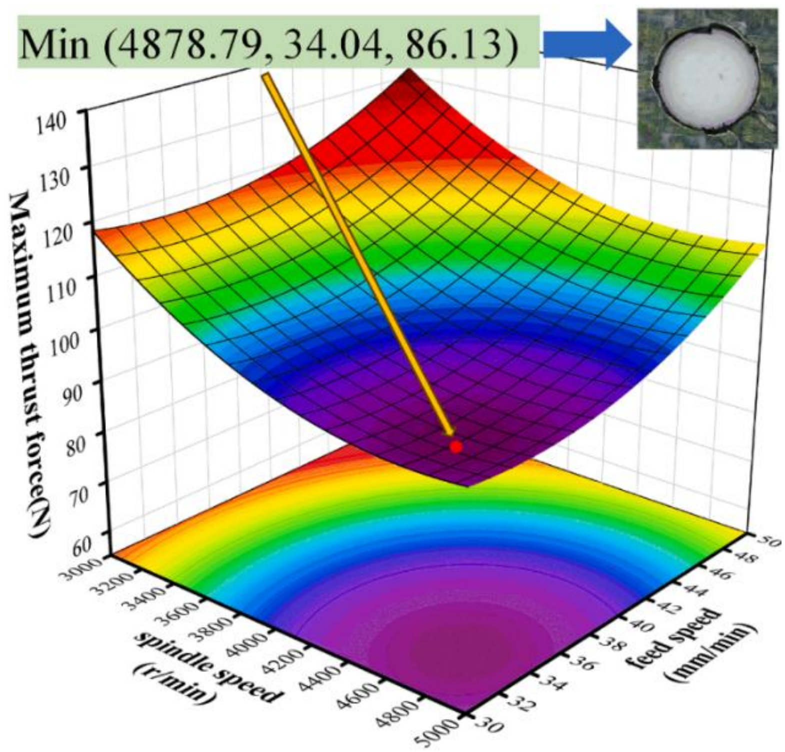


Figure 1.5 Response surface of maximum thrust for a TDR (Liu & Huang, 2024).

### 1.5.2 Vacuum Assisted Debris Mitigation

Bi (2010) addressed the common issue of debris contamination during the drilling of composite materials. In his study, Bi conducted the design and analysis of automatic dust extraction devices, culminating in a hood mounted on the spindle of a drill press. The dust extraction performance was evaluated using a fluid dynamics model in the software COSMOSFloWorks, demonstrating that full enclosure of the drilling area leads to effective dust extraction and that the size of the outlet hole has the most significant impact on extraction performance. Bi's designs, while effective, are not practical for field applications where most drilling operations are performed with handheld drills. For this reason, the work presented in this thesis offers an alternative design that does not require attachment to a drill press spindle, allowing it to be used on any surface and independently of the drilling tool.

# CHAPTER 2: 3D MODELING OF ULTRASONIC DATA

The work presented in this thesis explores the advancement of a non-destructive evaluation (NDE) technique called pulse-echo ultrasonic testing (PEUT) for the identification of internal damage in impacted composites and its application in the injection repair process. More specifically, this thesis presents novel contributions to the processing and visualization of PEUT data, including unique selection, filtering, and alignment methods. Furthermore, this work introduces three-dimensional plots of delaminations, and a novel visualization method called a delamination density map, which highlights the delamination network branches (DNBs) that may serve as optimal injection regions by maximizing the number of delaminations reached per injection point. Figure 2.1 shows the typical workflow in PEUT for injection repair, where two-dimensional data is projected in three dimensions for each front and back scans, to then combine them for a hybrid reconstruction of the damage network, which is ultimately used to extract the DNBs.

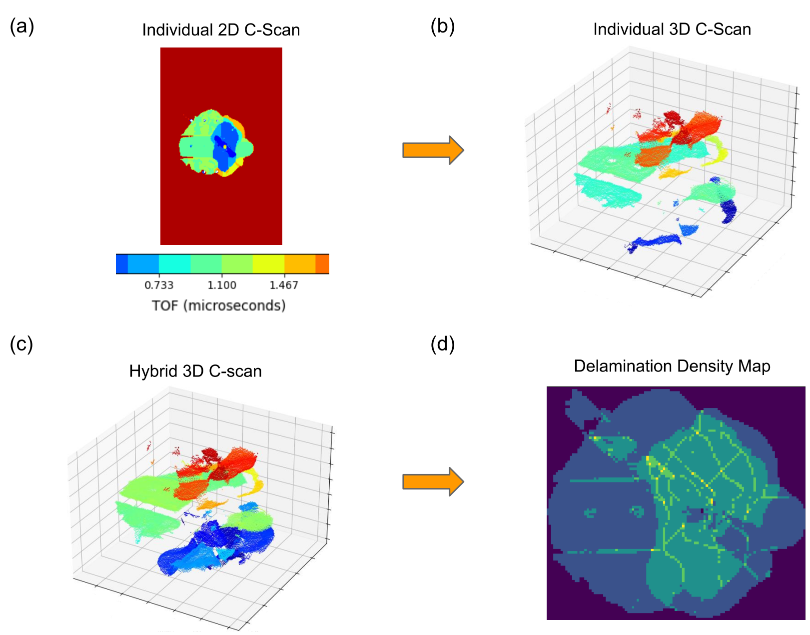


Figure 2.1 Python code plots: (a) Individual 2D C-scan, (b) individual 3D C-scan, (c) hybrid 3D C-scan, and (d) delamination density plot.

## 2.1 Pulse-Echo Ultrasonic Testing for Impacted Composites

### 2.1.1 Impact Damage in Composites

Composites, particularly laminates, are synergistic materials composed of a reinforcement (i.e., carbon fiber), an interface, and a matrix (i.e., thermoset epoxy), which are meticulously combined and processed to achieve composite material properties that surpass those of each component individually. Although composites possess very high strength-to-weight properties, each component in isolation exhibits poor mechanical characteristics — the matrix being brittle, and the bare fibers being strong yet limited to tension in the longitudinal direction. It is precisely the brittleness of the polymer matrix that promotes crack propagation and delamination growth and contributes to the material's limited energy absorption capacity. Moreover, the cohesive nature of the ply interface is what gives rise to delaminations after impact (Sun & Saleh, 2024).

Damage in composites is categorized into five levels based on severity and detectability, as defined by Advisory Circular AC 20-107B (Federal Aviation Administration, 2009). Category 1 damage includes barely visible impact damage (BVID) and manufacturing-induced defects such as very small delaminations, porosity, and surface scratches. BVID is most caused by low velocity impact (LVI) events. The size of BVID and the velocity threshold of LVI are not strictly defined, as these thresholds vary across manufacturers and research institutions. According to Sun and Saleh (2024), when the resulting failure modes include matrix cracking and delamination, the event is characteristic of LVI, and when the failure modes include fiber breakage and penetration, the event is characteristic of high velocity impact (HVI). However, this assumption is not always true because LVI and HVI each can cause delamination, fiber breakage, and penetration depending on the event conditions. Furthermore, BVID, illustrated in Figure 2.2, cannot be identified from the surface, and requires the use of advanced inspection methods known as NDE. This is, precisely, the type of damage that can be fixed with injection repair.

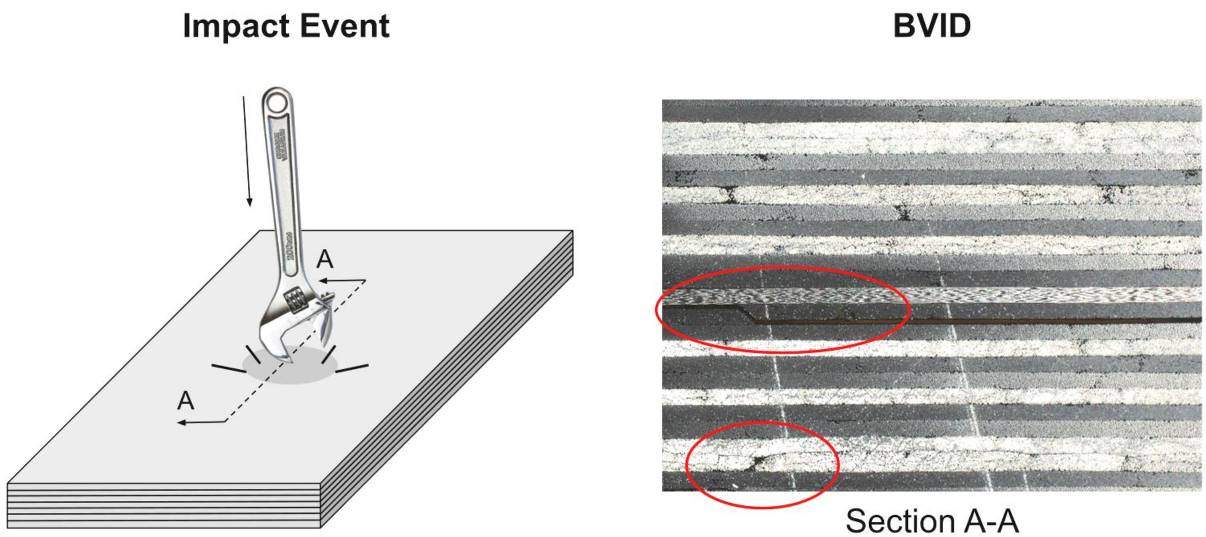


Figure 2.2 Low velocity impact (LVI) representation. Damage circled in red (image by C. Valerio).

*2.1.1.1 Failure Mode Mechanics*

Matrix cracking and delamination has been shown by Sun and Saleh (2024) to occur in conjunction. A [90/0/90] laminate provides a simplified illustration of how matrix cracks initiate and propagate. When the impactor contacts the upper layer of the laminate, elevated shear stresses develop at the periphery of the impacted area. The stiffness mismatch between the matrix and the fibers produces shear stress concentrations that induce 45° shear cracks in the upper layers and vertical cracks in the bottom layers owing to flexural deformation, as seen in Figure 2.3 (Sun and Saleh, 2024). This cracking is driven by locally generated interlaminar shear stresses ($\sigma_{13}$) that are significantly greater than the transverse ($\sigma_{33}$) and longitudinal ($\sigma_{11}$) stress components.

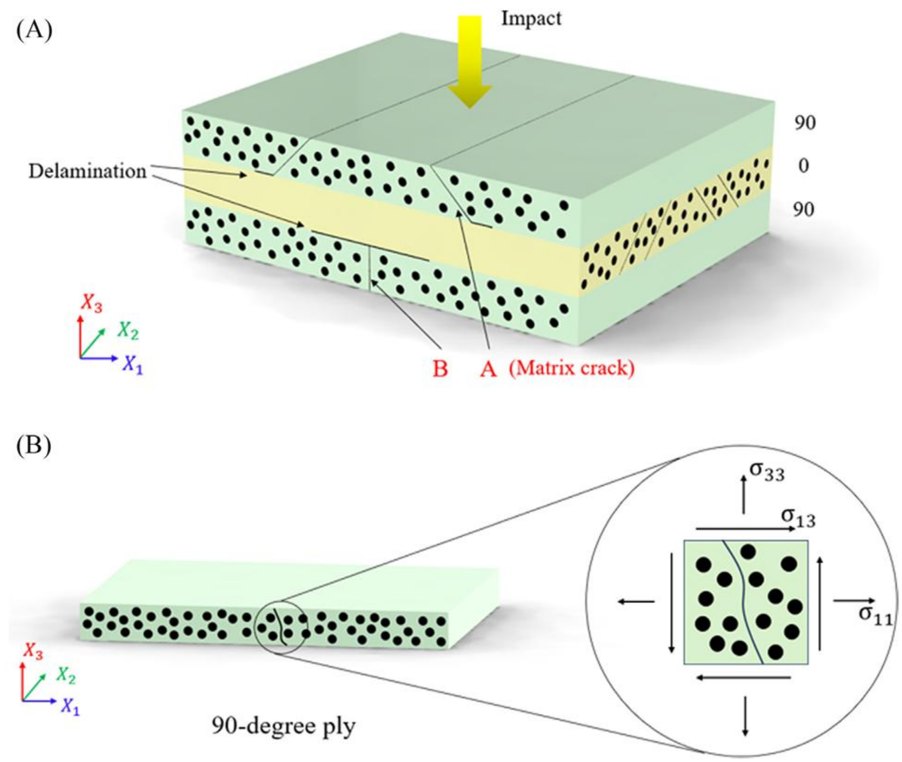


Figure 2.3 Mechanism of crack initiation under impact: (A) matrix cracks in an impacted 0/90/0 composite laminate, and (B) major stress components contributing to the matrix cracking in the 90-degree ply (Sun & Saleh, 2024).

The same interlaminar shear stress that drives matrix cracking also promotes debonding between adjacent plies. Delamination is fundamentally governed by the stiffness mismatch between plies of differing orientations — the greater the mismatch, the more severe the delamination growth potential. This is most pronounced in 0°/90° stacking sequences, which are considered the worst-case configuration for interlaminar stress concentration and is reflected in the lower delamination initiation thresholds observed in layups with a higher proportion of 0°/90° ply interfaces (Sun & Saleh, 2024). More specifically, delamination is initiated by the normal stress at the tip of a matrix crack, consistent with a Mode I fracture process. As the crack propagates along the ply interface, high interlaminar shear stresses develop and Mode II fracture becomes the dominant mechanism, as illustrated in Figure 2.4 (Sun & Saleh, 2024).

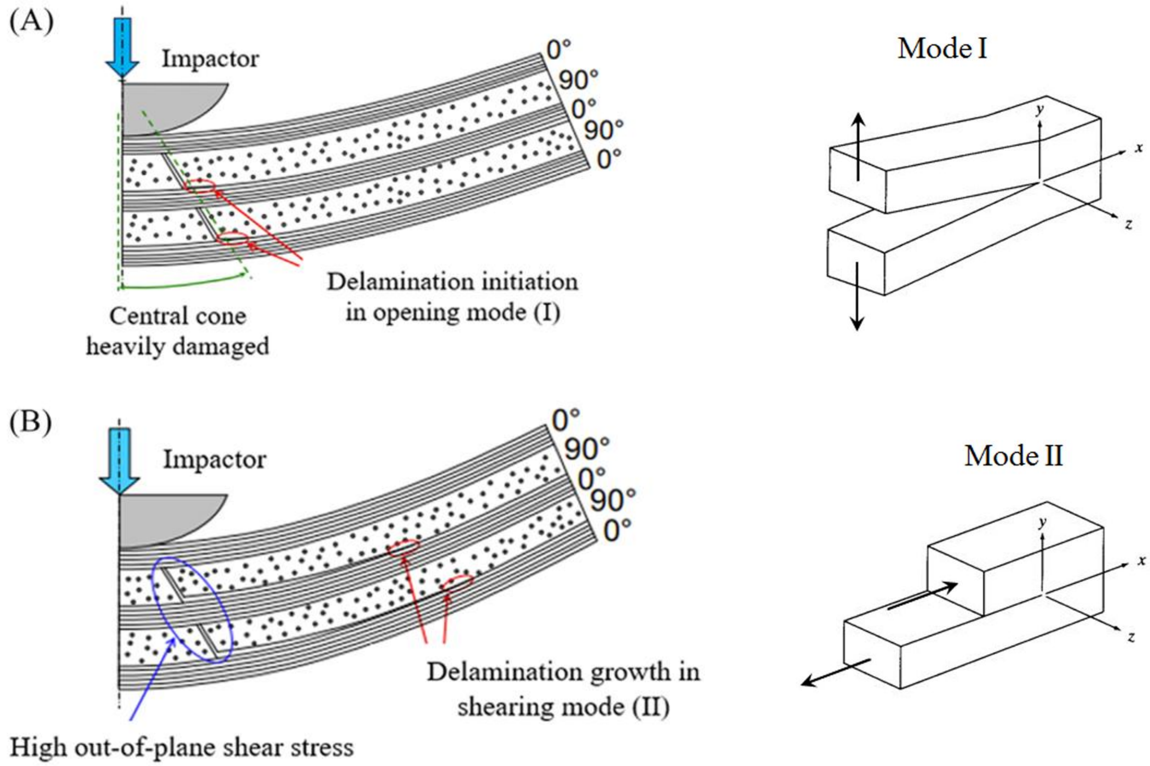


Figure 2.4 Typical patterns of delamination during impact loading: (A) delamination initiation, and (B) delamination propagation (Sun & Saleh, 2024).

### 2.1.2 Pulse-Echo Ultrasonic Testing

Pulse-echo ultrasonic testing is one of the most commonly used (NDE) methods for composites due to its ability to clearly reveal the size, shape, and depth of delaminations. PEUT utilizes acoustic energy to detect and characterize internal discontinuities and defects within a material. This is achieved by measuring the key features of an ultrasonic pulse emitted by a piezoelectric transducer (PZT), which propagates through the material before reflecting back to the sensor from either the back wall of the structure or an internal defect, as illustrated in Figure 2.5 (Zhao & Khatibi, 2023).

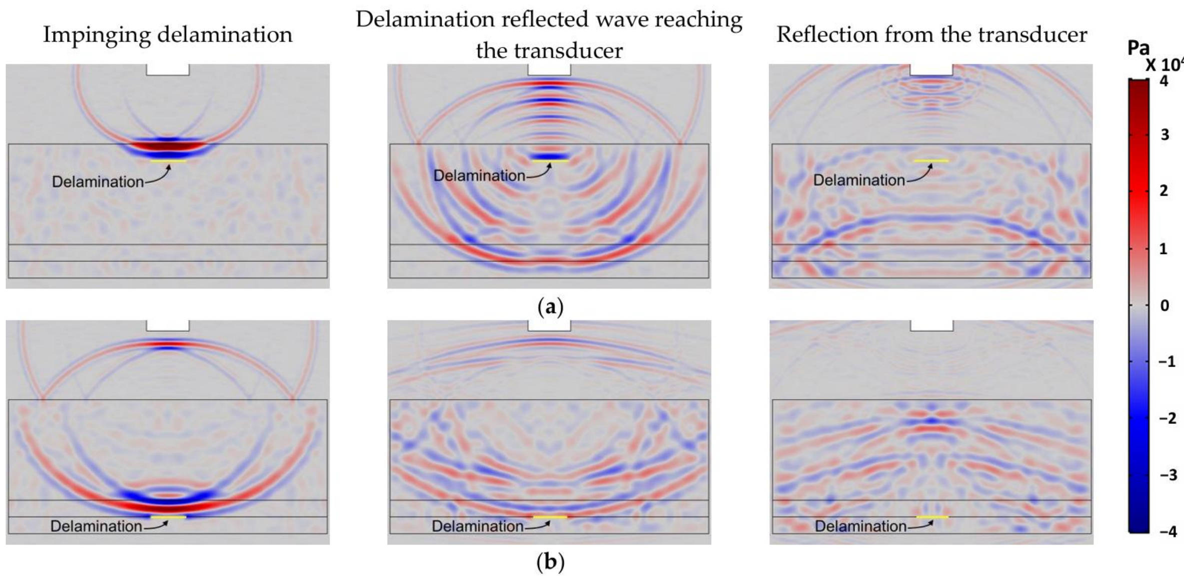


Figure 2.5 Pressure profile showing the source and reflected signals from (a) a shallow delamination, and (b) a deep delamination at various times using a PEUT model on COMSOL Multiphysics 6.0 (Zhao & Khatibi, 2023).

An ultrasonic wave is a traveling harmonic wave with a characteristic frequency typically above 20 kHz. In bulk solids, a wave is divided into two components: 1) a longitudinal wave (p-wave) where particles move parallel to the wave, and 2) a shear wave (s-wave) where particles move perpendicular to the wave. PEUT involves longitudinal waves that travel through a material where the PZT acts as both the transmitter and the receiver. The PZT contains a highly sensitive, smart piezoelectric material that reacts to the strain caused by the wave in a sinusoidal motion and creates a voltage that generates a waveform signal, shown in Figure 2.6, (a). As the PZT moves across the surface of a structure, it gathers a series of individual waveforms, which are the foundation of ultrasonic testing.  An A-scan, shown in Figure 2.6, (b), represents the quantitative measurement of a specific characteristic of the waveform signal, such as amplitude or time of flight (TOF).

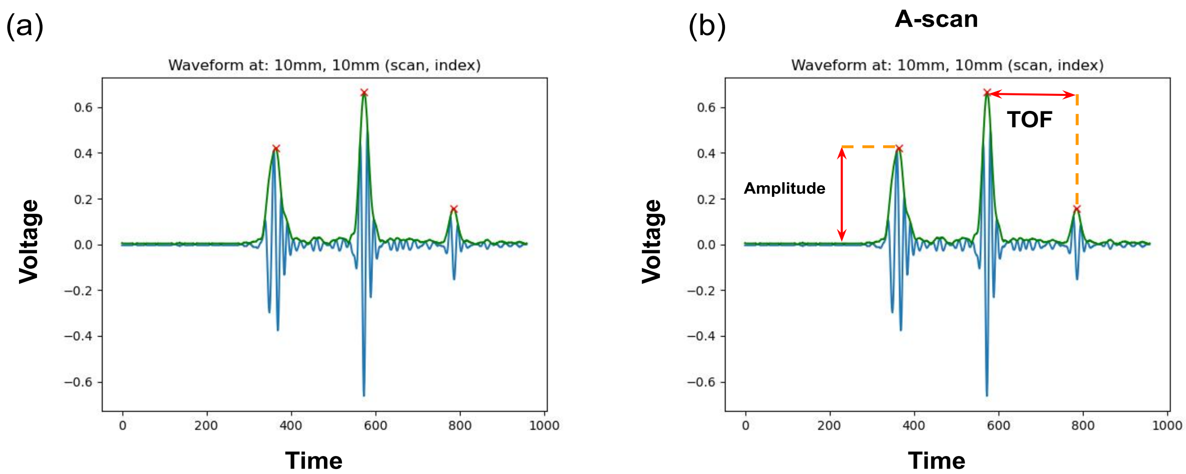


Figure 2.6 Pulse-echo ultrasonic testing: (a) Plot of a waveform from a piezoelectric transducer, and (b) A-scan measurements.

Furthermore, the distance to an internal defect can be derived as well by simply multiplying the acoustic wave speed of the scanned material by the total travel time of the pulse. Since the total transit time involves the pulse traveling to the defect and back, the distance from the surface of the test material to the internal discontinuity is divided by two, as follows:

$$d = \frac{1}{2} * v * t \quad \text{Eq. 1}$$

where d is the distance from the surface to the discontinuity in the test material, v is the sound wave velocity of the material in the direction of the wave's travel path, and t is the transit time (i.e., TOF).

B-scans and C-scans are simply the combination of multiple A-scans across a specific distance, as illustrated in Figure 2.7. In summary, an A-scan is a point measurement, a B-scan is a line measurement, and a C-scan is a 2D measurement of a certain wave feature that varies depending on geometry and internal defects. The work presented in this thesis explores the versatility of PEUT by manipulating the waveform packages and developing novel ways of visualizing the data for a more intuitive understanding of impact damage in composite structures.

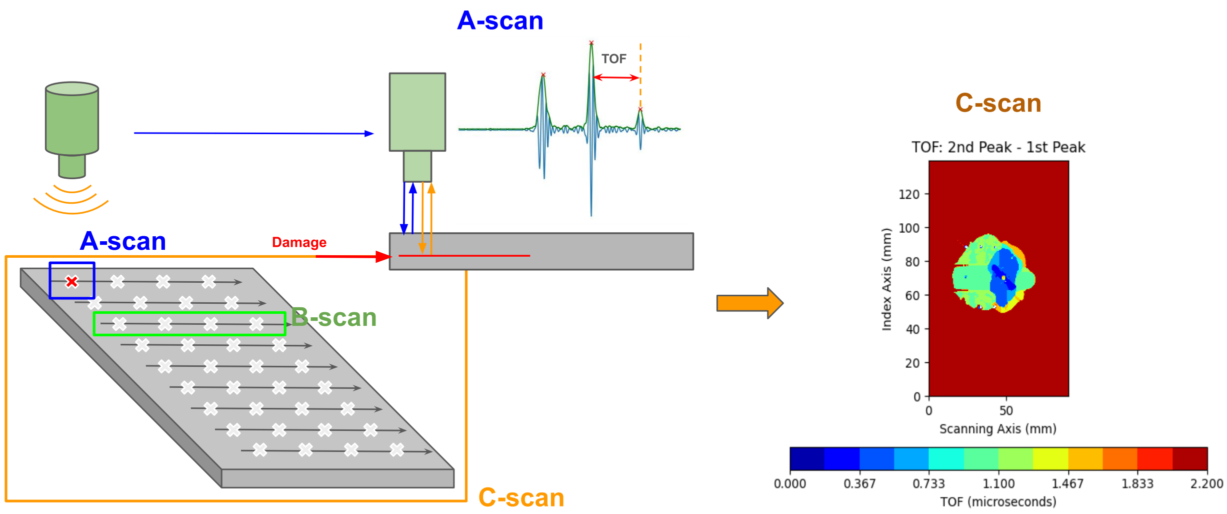


Figure 2.7 Pulse-echo ultrasonic testing diagram.

## 2.2 3D Modeling Python Code for NDE Visualization

### 2.2.1 Code Overview

Reconstructing C-scan data into three-dimensional plots of time of flight or depth offers advantages for the advancement of pulse-echo ultrasonic testing and the interpretation of its datasets. By projecting C-scan data in three dimensions, delamination layers are clearly visualized, data outliers are readily identified, delamination interfaces are more precisely localized, and defect depth is more directly interpretable. The work presented in this thesis involves the development of a Python code that filters, segments, and extracts damage data from C-scan waveform datasets to generate three-dimensional plots of delaminations, hybrid three-dimensional plots when both front-side and back-side scan data are available, and delamination network branch maps, referred to hereafter as density maps. This Python code is organized into functions that each perform a distinct role within the processing workflow. Figure 2.8 presents the main functions of the code, arranged sequentially from top to bottom at the center of the figure. The functions shown to the right are helper functions, which perform supporting operations and are called within the main functions. The figure also illustrates representative output plots generated by each function. Overall, the development of the hybrid plots presents a solution to a fundamental limitation of PEUT known as the shadowing effect, and the density maps highlight the DNBs that may serve as optimal injection regions by maximizing the number of delaminations reached per injection point.

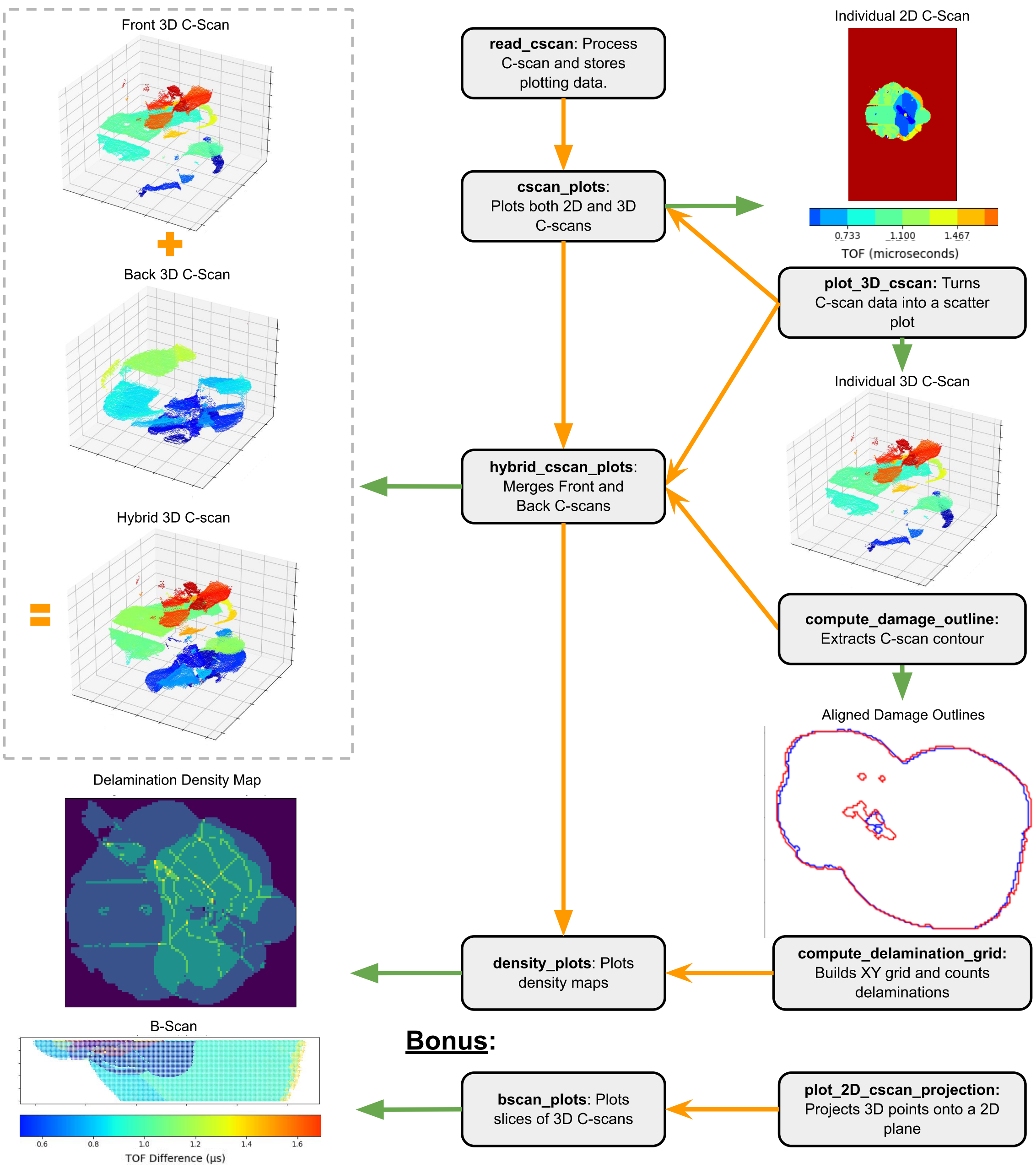


Figure 2.8 NDE visualization code flowchart.

### 2.2.2 File Input Requirements

The input file type required by the Python code must be a character-delimited file, such as a comma-separated values (.csv), text (.txt), or data (.dat) file. In this research, when the data is acquired using a Pocket UT device, it will be stored in proprietary .csc files, which must be converted to a compatible file format prior to processing. Additionally, data files exported from the Pocket UT always contain a header comprising instrument settings and acquisition metadata, which does not form part of the scan data. The code disregards this header and processes only the scan data, starting at row 50 of the .csv file, where the first value contains the row (index number) of the scan, the second value contains the column (scanning number), and the remaining values contain the A-scan waveform data for the corresponding scan point, as shown in Figure 2.9.

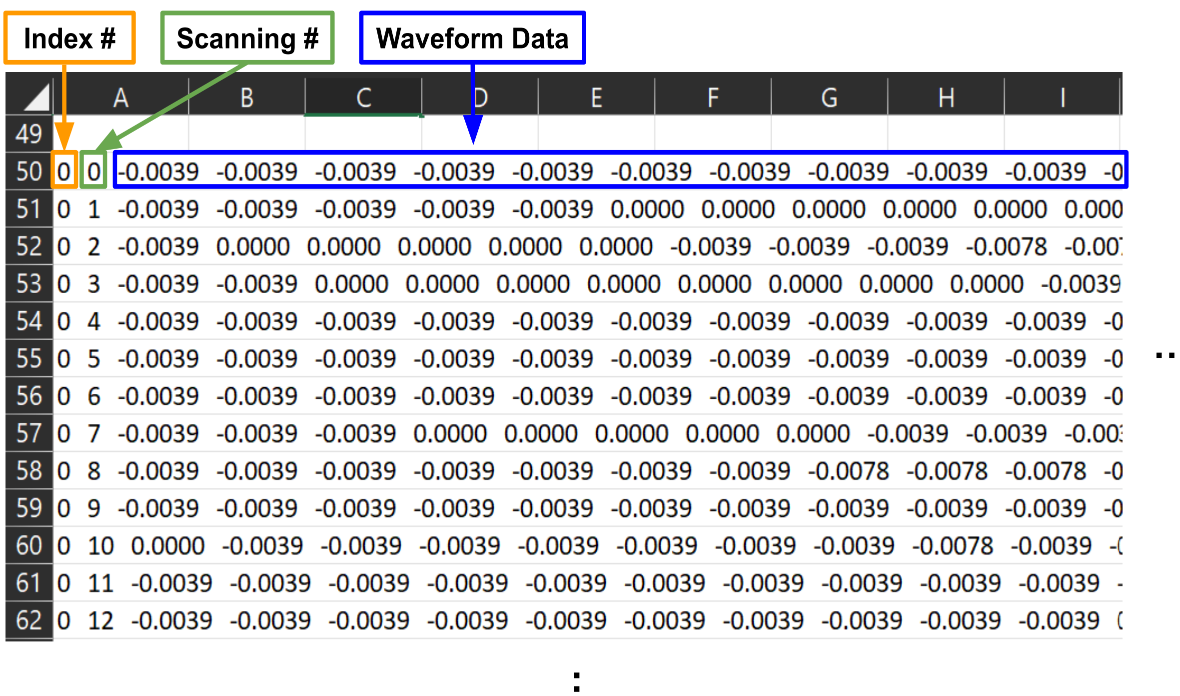


| | A | | B | C | D | E | F | G | H | I | | | |
|---|---|---|---|---|---|---|---|---|---|---|---|---|---|
| 49 | | | | | | | | | | | | | |
| 50 | 0 | 0 | -0.0039 | -0.0039 | -0.0039 | -0.0039 | -0.0039 | -0.0039 | -0.0039 | -0.0039 | -0.0039 | -0.0039 | -0 |
| 51 | 0 | 1 | -0.0039 | -0.0039 | -0.0039 | -0.0039 | -0.0039 | 0.0000 | 0.0000 | 0.0000 | 0.0000 | 0.0000 | 0.000 |
| 52 | 0 | 2 | -0.0039 | 0.0000 | 0.0000 | 0.0000 | 0.0000 | 0.0000 | -0.0039 | -0.0039 | -0.0039 | -0.0078 | -0.00 |
| 53 | 0 | 3 | -0.0039 | -0.0039 | 0.0000 | 0.0000 | 0.0000 | 0.0000 | 0.0000 | 0.0000 | 0.0000 | 0.0000 | -0.0039 |
| 54 | 0 | 4 | -0.0039 | -0.0039 | -0.0039 | -0.0039 | -0.0039 | -0.0039 | -0.0039 | -0.0039 | -0.0039 | -0.0039 | -0 |
| 55 | 0 | 5 | -0.0039 | -0.0039 | -0.0039 | -0.0039 | -0.0039 | -0.0039 | -0.0039 | -0.0039 | -0.0039 | -0.0039 | -0 |
| 56 | 0 | 6 | -0.0039 | -0.0039 | -0.0039 | -0.0039 | -0.0039 | -0.0039 | -0.0039 | -0.0039 | -0.0039 | -0.0039 | -0 |
| 57 | 0 | 7 | -0.0039 | -0.0039 | -0.0039 | 0.0000 | 0.0000 | 0.0000 | 0.0000 | 0.0000 | -0.0039 | -0.0039 | -0.00 |
| 58 | 0 | 8 | -0.0039 | -0.0039 | -0.0039 | -0.0039 | -0.0039 | -0.0039 | -0.0039 | -0.0078 | -0.0078 | -0.0078 | -0 |
| 59 | 0 | 9 | -0.0039 | -0.0039 | -0.0039 | -0.0039 | -0.0039 | -0.0039 | -0.0039 | -0.0039 | -0.0039 | -0.0039 | -0 |
| 60 | 0 | 10 | 0.0000 | -0.0039 | -0.0039 | -0.0039 | -0.0039 | -0.0039 | -0.0039 | -0.0039 | -0.0078 | -0.0039 | -( |
| 61 | 0 | 11 | -0.0039 | -0.0039 | -0.0039 | -0.0039 | -0.0039 | -0.0039 | -0.0039 | -0.0039 | -0.0039 | -0.0039 | - |
| 62 | 0 | 12 | -0.0039 | -0.0039 | -0.0039 | -0.0039 | -0.0039 | -0.0039 | -0.0039 | -0.0039 | -0.0039 | -0.0039 | ( |

Figure 2.9 .csv file.

### 2.2.3 Data Processing – `read_cscan()`

This function is adapted from a previous MATLAB C-scan processing tool developed by Jessica Chan (2022). In this work, Mac Delaney's (2026) translation of the tool into Python is used. The `read_cscan()` function serves as the data processing stage of the ultrasonic C-scan analysis workflow. It imports the raw ultrasonic waveform data exported by the Pocket UT, extracts the acquisition parameters (e.g., sampling frequency and scan resolution), and processes every A-scan independently to identify a useful signal feature. More specifically, a wave envelope is generated using a Hilbert transform-based peak detection algorithm, which produces an analytical signal that enables surface reflections to be reduced into signal feature measurements, as shown in Figure 2.10. The Hilbert transform can be expressed as:

$$x_a = F^{-1}(F(x)2U) \qquad \text{Eq. 2}$$

where x is the input signal in the time domain, $x_a$ is the analytical signal in the time domain, F is the Fourier transformation, and U is the unit step function (Delaney, 2026).

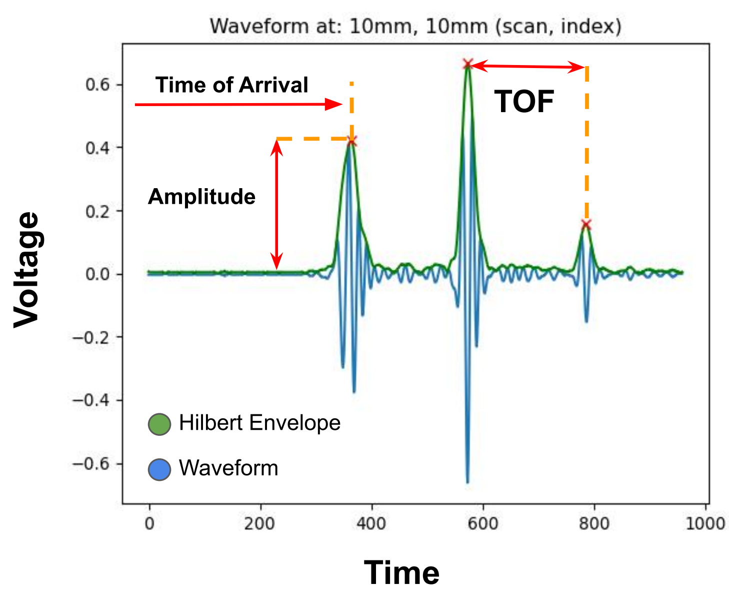


Figure 2.10 A-scan waveform package breakdown.

From these detected peaks, the function computes several spatial inspection parameters, including the first echo time-of-arrival (TOA), the TOF difference (ΔTOF) between successive reflections, the amplitudes of the first and second echoes, and the amplitude ratio between them. These quantities are then organized into two-dimensional matrices corresponding to the physical scanning and indexing coordinates of the specimen, thereby generating the datasets required for subsequent C-scan plotting. Finally, both the processed inspection parameters and the original waveform data are saved into two separate binary pickle (.pk) files — a Python-native format for efficient data storage — providing an efficient intermediate format for downstream plotting, three-dimensional reconstruction, and further ultrasonic analysis, which is repeatedly used in the throughout the workflow of the code.

### 2.2.4 Plot Generation – `cscan_plots()`

The function `cscan_plots()` provides a set of 2D plots with useful information about the scanned structure including amplitude, amplitude ratio, surface contour, damage threshold, damage area, and time of flight. However, as the emphasis of this work, the function has the option to generate a 3D reconstruction of any 2D C-scan. This is controlled by setting the variable *three_d* equal to "True" in the function's input, as shown in Figure 2.11.

```
def cscan_plots(pkfile, save_processed=True, tof1plot = 1, tofdplot = 1, dmg = 1,
                dent = 1, amp1plot = 1, amp2plot = 1, amp3plot = 1, contplot = 1,
                sect_cut = -1, cont_range = [-1.5,1.5], thk = 3.292, Front = False,
                three_d = True, Ready = True):
```

Figure 2.11 `cscan_plots()` input variables: 3D plot activation.

Doing so creates a 3D scatter plot of delaminations from the same data used for the ΔTOF 2D plot. Furthermore, the 3D scatter plot values are rearranged depending on whether the scan is performed from the front or the back surface of the structure. If the scan is done on the front surface, the values are mirrored in the vertical direction to match the true spatial location of the defects. This is because high values of ΔTOF indicate damage closer to the back surface and low values of ΔTOF indicate damage closer to the top surface, but the plot's z-axis shows values from lowest to highest in the vertical direction, as shown in Figure 2.12. This feature must be activated by the user by setting the variable *Front* equal to "True" in the function's input, as illustrated in Figure 2.13.

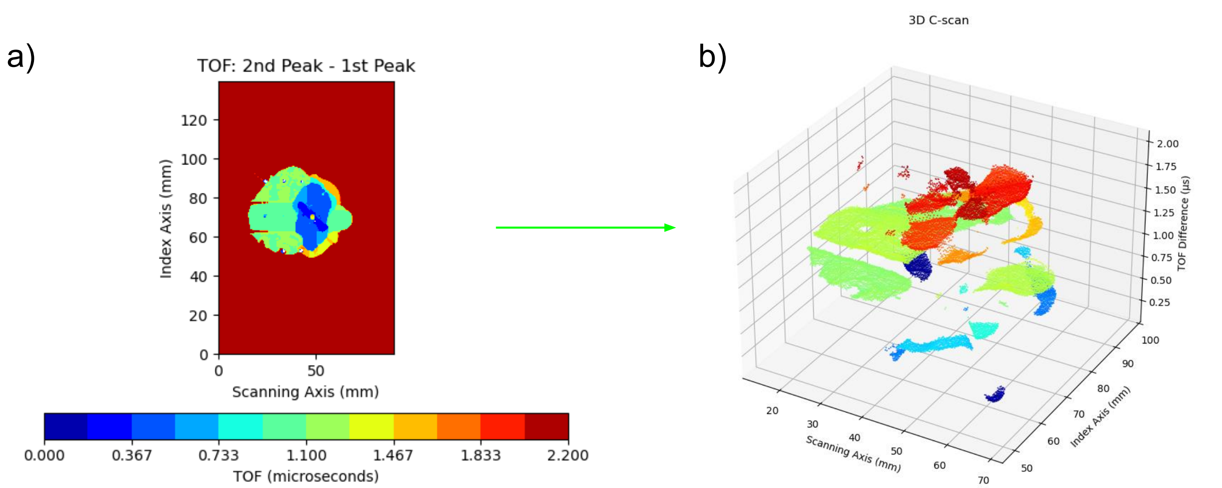


Figure 2.12 3D Reconstruction of a **Front** C-scan: a) 2D C-scan plot of ΔTOF, and b) 3D projection of damage.

```
def cscan_plots(pkfile, save_processed=True, tof1plot = 1, tofdplot = 1, dmg = 1,
                dent = 1, amp1plot = 1, amp2plot = 1, amp3plot = 1, contplot = 1,
                sect_cut = -1, cont_range = [-1.5,1.5], thk = 3.292, Front = True,
                three_d = True, Ready = True):
```

Figure 2.13 `cscan_plots()` input variables: Front values permutation activation.

Because each C-scan is fundamentally different, the user must iteratively select the thresholds that determine how much of the C-scan data is actual readings of damage. In this case, the user can set the variable *Ready* to “False”, as shown in Figure 2.14, (a), which will force the code to only plot the top view of the 3D reconstruction along with its original 2D version such that a visual comparison of the damage map can be conducted before plotting and saving the final 3D plots. For each iteration, the user must choose a maximum coefficient, a minimum coefficient, and a radius of damage, which control how much of the data is being included as damage. More details on data selection in Section 2.2.4.2.


Figure 2.14 Example of a 3D plot with non-optimal data selection coefficients: (a) data selection coefficients, and (b) example of a top view of a 3D C-scan showing excess data caused by excessively large thresholds.

Once the ideal coefficients and radius have been identified, the user can set the variable *Ready* to “True” and the code will generate the whole package of plots, which includes both all the 2D plots and the final isometric, top, and front side views of the 3D scatter plot, shown in Figure 2.15, useful for the spatial visualization of delaminations within the composite.

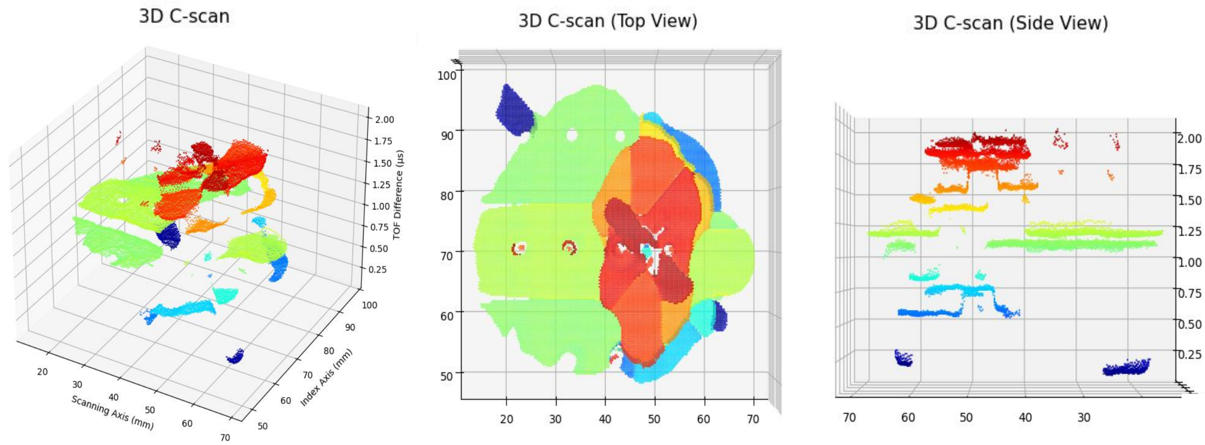


Figure 2.15. 3D C-scan outputs from `cscan_plots()` function.

#### *2.2.4.1 Data Filtering*

Before any plot is generated, the code performs an automatic filtering of the entire C-scan dataset by applying a statistical thresholding method based on the 95th percentile. A percentile is a statistical value below which a given percentage of data falls; applying the 95th percentile therefore retains only those values at or below 95% of a certain threshold, effectively excluding the top 5% as outliers. This threshold is defined as the ΔTOF value corresponding to the total thickness of the structure. Notably, when the damage area is considerably smaller than the surrounding pristine material, the total thickness can be estimated as the mode of the ΔTOF data, since undamaged material dominates the scan area. To find the thickness, the code generates a histogram of the ΔTOF data and identifies the most frequently occurring value, which is then defined as the thickness of the specimen. Applying the 95th percentile with respect to this thickness eliminates extreme outliers, as seen in Figure 2.16, and redefines the upper bound of the ΔTOF range as the maximum allowable ΔTOF value (tofd_max). These outliers typically arise from abnormal signal reflections in zones with sharp edges or geometric discontinuities.

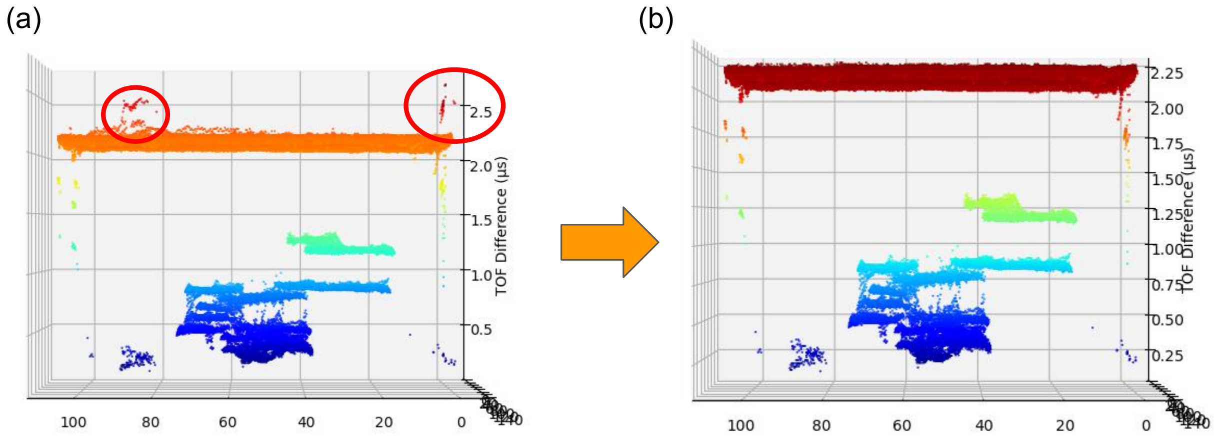


Figure 2.16 95th percentile threshold application: (a) C-scan data set with outliers, (b) C-scan data set after 95th percentile filtering.

#### *2.2.4.2 Data Selection and Plotting of 3D C-Scans –* `plot_3D_cscan()`

After loading the .pk files, filtering the data, and calculating the desired values, the helper function `plot_3D_cscan()` is called within `cscan_plots()`, which generates the 3D C-scans. The `plot_3D_cscan()` function was developed to reconstruct and visualize internal delamination damage as a three-dimensional point cloud from ultrasonic pulse-echo C-scan data. The function provides a flexible framework that can either process raw ΔTOF measurements prior to visualization or directly display previously processed spatial coordinates (X, Y, Z)—this dual-mode capability allows this helper function to be used for both individual C-scans and hybrid scans, respectively.

The function accepts two different forms of input. In the first mode, the function receives the original scan coordinates together with the ΔTOF (or depth, see Section 2.2.5.2) matrix and its corresponding maximum and minimum values. In this configuration, the function performs damage extraction before constructing the three-dimensional representation. In the second mode, previously processed Cartesian coordinates (X, Y, Z) are supplied directly, bypassing all data selection operations. This option is primarily intended for hybrid C-scans or other datasets that have already undergone damage filtering and segmentation, as explained in Section 2.2.5. When original ΔTOF data are provided, the first step consists of reconstructing the scan into a Cartesian grid using the indexing-axis (x-axis) and scanning-axis (y-axis) coordinates. The ΔTOF measurements are stored as the vertical coordinate (z-axis), thereby assigning every ultrasonic measurement a unique three-dimensional position. Before storing the data, upper and lower threshold values are applied to eliminate surface measurements, which are defined as user-adjustable fractions of the maximum and minimum ΔTOF values as follows:

$$Threshold_{upper} = C_{max} * \Delta\mathrm{TOF}_{max} \quad \text{Eq. 3}$$

$$Threshold_{lower} = C_{min} * \Delta\mathrm{TOF}_{min} \quad \text{Eq. 4}$$

where $C_{max}$ and $C_{min}$ are empirical threshold coefficients selected by the user. Any measurement whose ΔTOF value lies above the upper threshold or below the lower threshold is classified as a reflection from either the front or back surface of the specimen and replaced with a NaN value. This selection process removes most of the front- and back-wall echoes while preserving the intermediate ΔTOF values associated with internal delaminations. Because laminate geometry and attenuation vary between specimens, these threshold coefficients remain user-adjustable, allowing the selection process to be tailored for different datasets.

Following thresholding, a binary mask is generated in which all remaining valid ΔTOF measurements are assigned a value of one while discarded points remain undefined. Subsequently, connected-component labeling is applied to this binary mask to identify individual data clusters. Each cluster represents a potential delamination or a collection of residual artifacts that survived the thresholding process. For every cluster, the centroid is assumed to be the mean of the values in the x and y direction, computed in image coordinates, as seen in Equations 5 and 6:

$$x_c = \frac{1}{N}\sum_{i=1}^{N} x_i \quad \text{Eq. 5}$$

$$y_c = \frac{1}{N}\sum_{i=1}^{N} y_i \qquad \text{Eq. 6}$$

where N is the number of pixels belonging to the cluster.

Furthermore, the Euclidean distance, denoted by Equation 7, between each centroid and the geometric center of the scanned panel is evaluated,

$$d = \sqrt{(x_c - x_0)^2 + (y_c - y_0)^2} \qquad \text{Eq. 7}$$

where ($x_0$, $y_0$) denotes the center of the scan. Only clusters whose centroid lies within a user-defined radius are retained for visualization. This procedure exploits prior knowledge that impact damage is intentionally introduced near the center of the specimen, allowing peripheral artifacts and isolated noise clusters to be automatically rejected without requiring manual segmentation. Alternatively, if the impact damage is at an arbitrary point on the structure, perform the scan around the impact area to artificially center the damage zone. After applying both the thresholds and the cluster radius, the damage network will be successfully isolated, as seen in Figure 2.17. The retained regions are subsequently used to construct a damage mask that isolates only the ultrasonic measurements associated with the impact damage. All remaining measurements outside this mask are discarded.

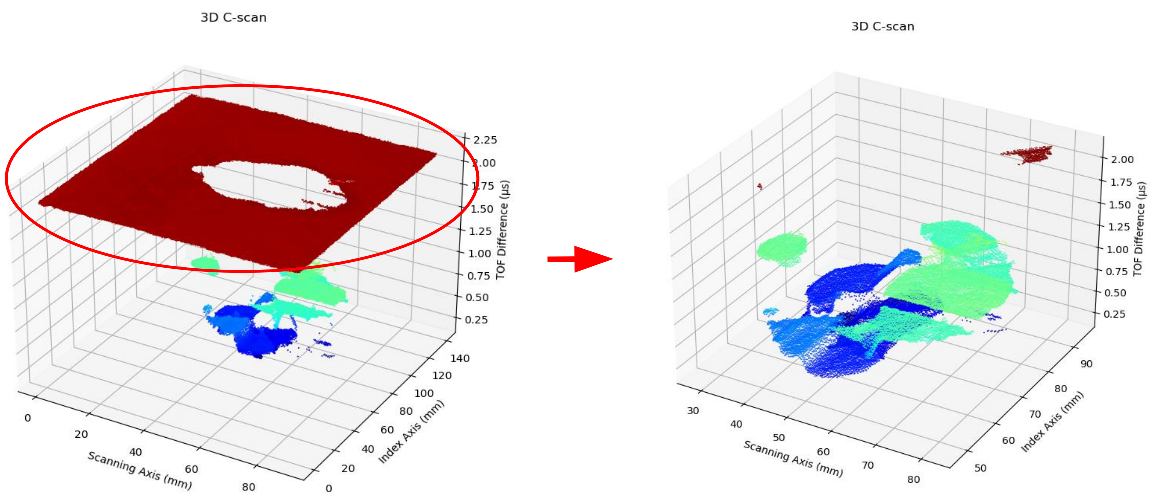


Figure 2.17 3D plot before and after excluding surface readings.

If the scan corresponds to the front inspection surface, the coordinates are reflected according to

$$Z_{front} = TOFd_{max} - Z \quad \text{Eq. 8}$$

which aligns the reconstructed delamination geometry with its physical location inside the laminate. Without this transformation, front-side measurements would appear mirrored relative to back-side measurements because high values of ΔTOF indicate damage closer to the back surface and low values of ΔTOF indicate damage closer to the top surface, but the plot's z-axis shows values from lowest to highest in the vertical direction. The filtered scan is then converted from a structured grid into an unstructured point cloud by flattening the coordinate matrices and removing all undefined values. This produces three one-dimensional coordinate arrays representing the spatial location of every retained damage point.

The centroid of the reconstructed damage cloud is subsequently calculated to provide a representative location of the damage. The x and y coordinates are approximated from the arithmetic mean of the filtered point cloud, like in the case of each individual cluster. On the other hand, the centroid's z coordinate will be calculated differently depending on the data input.

For scans reconstructed directly from raw ΔTOF data, the midplane is assigned as one-half of the laminate thickness represented by

$$\bar{z} = \frac{TODd_{max}}{2} \quad \text{Eq. 9}$$

When previously processed coordinates are supplied instead (as in the case of a hybrid C-scan), the vertical centroid is computed directly from the reconstructed point cloud, as follows:

$$\bar{z} = \frac{1}{N}\sum_{i=1}^{N} z_i \quad \text{Eq. 10}$$

where N is the number of data points belonging to a single Z array. This is because processed coordinates vary in magnitude such that their maximum value of ΔTOF is most likely not equal to the specimen's thickness like in the case of a raw dataset.

The final visualization is generated as a three-dimensional scatter plot in which each retained ultrasonic measurement is plotted according to its spatial coordinates. The ΔTOF is simultaneously mapped to the color of each point using a jet colormap, allowing the internal delamination morphology to be visualized as a continuous volumetric cloud rather than as discrete two-dimensional slices. The plot's viewing elevation and azimuth can optionally be specified by the user to facilitate interpretation from different perspectives, while default values produce an isometric representation suitable for general visualization.

An additional feature allows the processed point cloud and its associated metadata—including the reconstructed coordinates, centroid location, TOFD limits, and depth representation—to be exported in a .pk file. These processed datasets serve as standardized inputs for subsequent hybrid reconstructions, enabling multiple C-scans obtained from different inspection surfaces to be spatially aligned and combined into a unified three-dimensional damage model. Overall, this function performs three primary tasks: (1) automatic isolation of internal delamination from raw ultrasonic ΔTOF data through thresholding and cluster analysis, (2) reconstruction of the selected measurements into a three-dimensional point cloud that accurately represents the internal damage morphology, and (3) generation of standardized datasets that can be directly integrated into the hybrid reconstruction workflow described in the following section.

### 2.2.5 Hybrid 3D C-Scans – `hybrid_cscan_plots ()`

Because damage detection in pulse-echo ultrasonic testing relies on reflected signals, C-scans are inherently limited by the first major reflection encountered. Once a reflection occurs, deeper damage may remain undetected. This limitation is known as the shadowing effect. To mitigate shadowing, hybrid 3D C-scans are created by combining front- and back-surface scans, as illustrated in Figure 2.18.

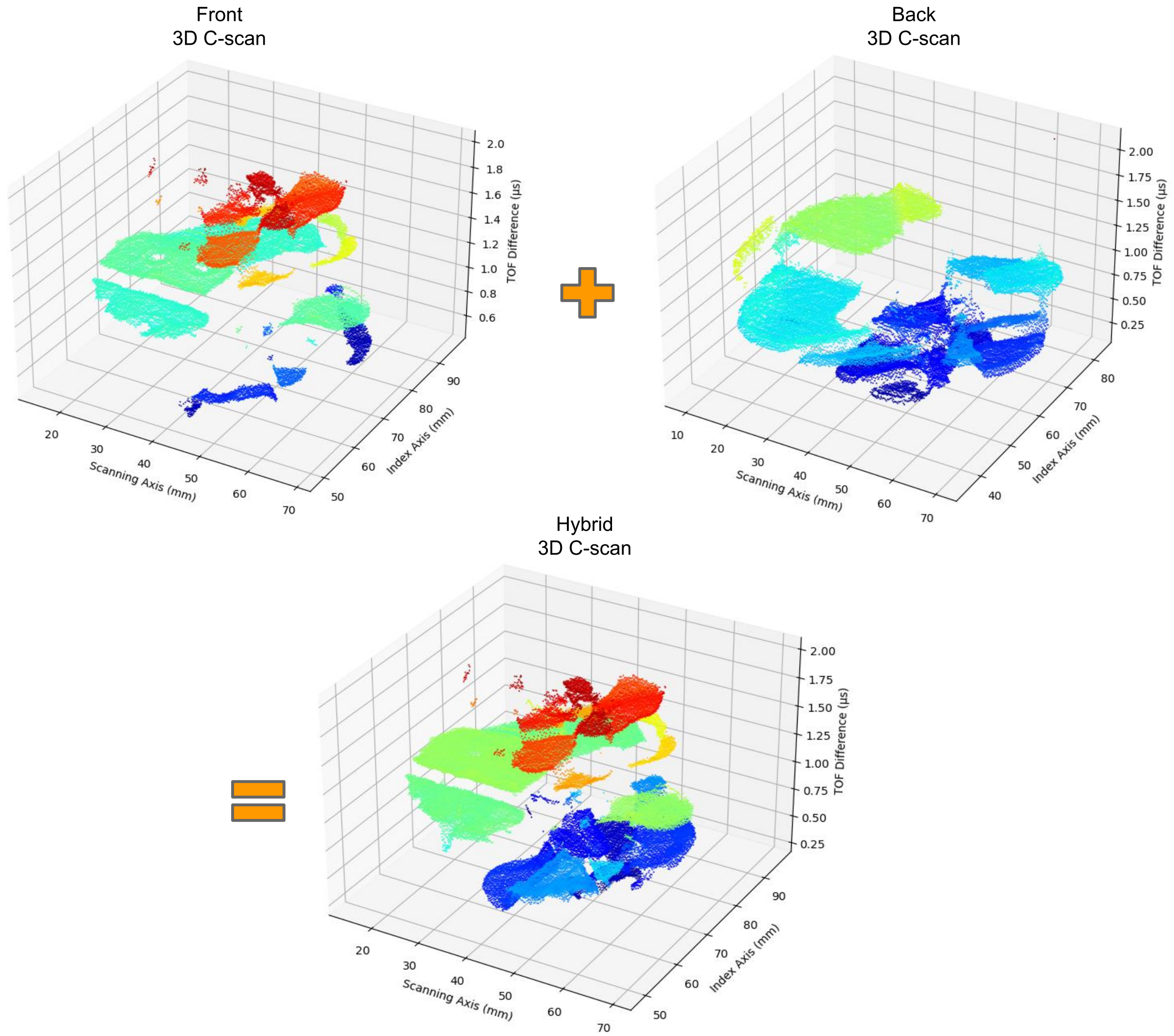


Figure 2.18 Hybrid 3D C-scan plot

The `hybrid_cscan_plots()` function was developed to combine independent front- and back-surface ultrasonic C-scans into a single three-dimensional representation of the internal delamination network. Rather than treating each scan independently, the function spatially aligns both point clouds — mapping them into a common coordinate frame — through a combination of geometric transformations and centroid-based alignment, enabling a complete reconstruction of the damage morphology across the full laminate thickness. The function generates the hybrid plots by combining the X, Y, and Z (ΔTOF or depth) coordinate data from any set of front- and back-surface C-scans, which are automatically generated and stored in .pk files by the `cscan_plots()` function, ensuring that only segmented damage features are incorporated into the reconstruction.

The first stage involves loading the processed front- and back-surface point clouds and mirror the back-side scan horizontally. This mirroring operation compensates for the reversed x-coordinates that naturally arise when opposite specimen surfaces are inspected, thereby placing both scans within a common reference frame. Once mirrored, the centroids of the two damage point clouds are compared to determine the required translational offsets in the scanning, indexing, and ΔTOF directions. These offsets are automatically computed from the centroid coordinates, enabling the back-surface scan to be translated into alignment with the front-surface scan while preserving the relative geometry of the damage features. Further details on automatic data alignment are provided in Section 2.2.5.1. This feature can be disabled by setting the variable *auto_align* to False in the function's input.

For cases in which automatic alignment alone is insufficient, optional user-defined corrections, based on visual inspection, should be applied to further refine the operation. Manual adjustment is enabled by setting *Manual_Auto* to True and assigning the desired correction values to *dx_manual*, *dy_manual*, and *dz_manual* in mm, as seen in Figure 2.19.

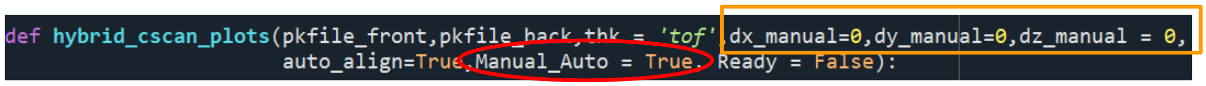


Figure 2.19 `hybrid_cscan_plots()` input variables: manual alignment.

It was observed that both the front- and back-surface scans include overlapping damage at the midplane region. These shared midplane delaminations serve as reliable alignment reference features. As shown in Figure 2.20, once complete alignment is achieved, these midplane delaminations, and any other damage features detected by both scans, should coincide at equivalent z values.

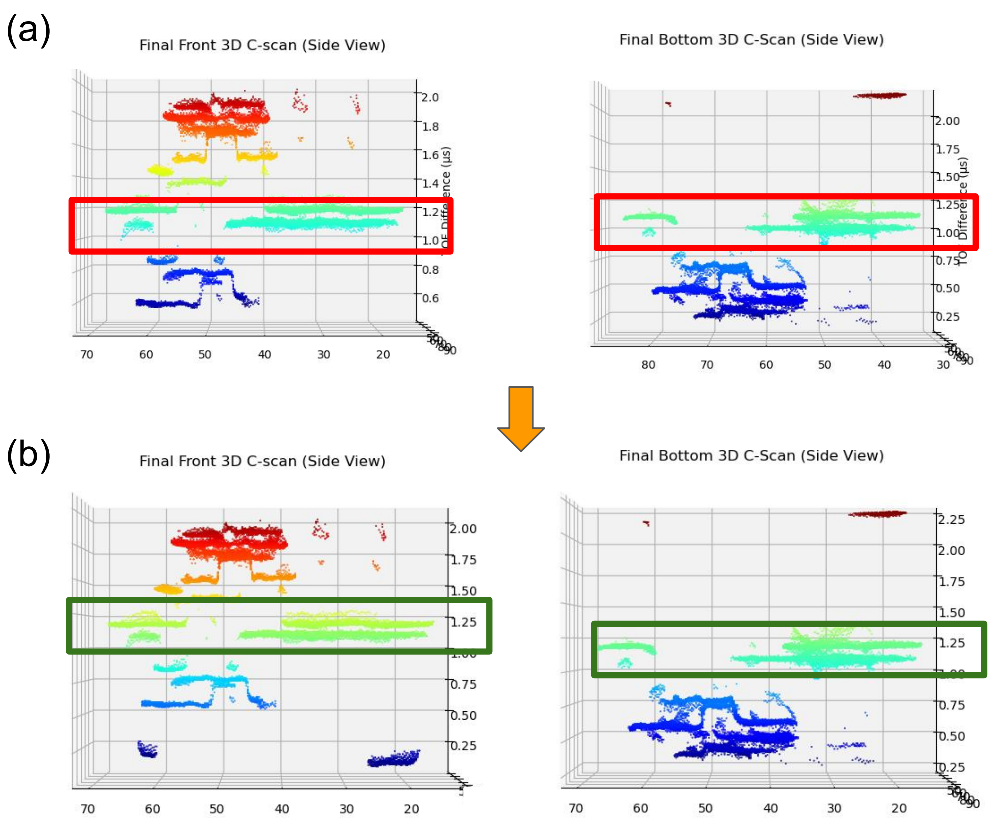


Figure 2.20. Front and Back 3D C-scans alignment: (a) midplane delaminations at different ΔTOF values, (b) midplane delaminations aligned.

In addition, both scans must be aligned in the x-y plane, which is also performed automatically. However, in cases where automatic alignment is insufficient, the user may use the damage outlines from both scans as a visual reference and translate the data until the outlines of both scans are overlapping by at least 50%. The outlines are extracted by a helper function called `compute_damage_outline()`, which first discretizes the spatial coordinates onto a uniformly spaced Cartesian grid, where each occupied grid cell is assigned a binary value of one to indicate the presence of damage and zero otherwise. A binary erosion operation is then applied to remove small, isolated discontinuities and refine the boundary of the damage region, producing a refined binary mask. Finally, a contour extraction algorithm identifies the outer boundary of the connected damage region. The `hybrid_cscan_plots()` function uses this helper function to generate the outlines of both the front- and back-surface scans and renders them in a single plot window to facilitate visual inspection, as shown in Figure 2.21.

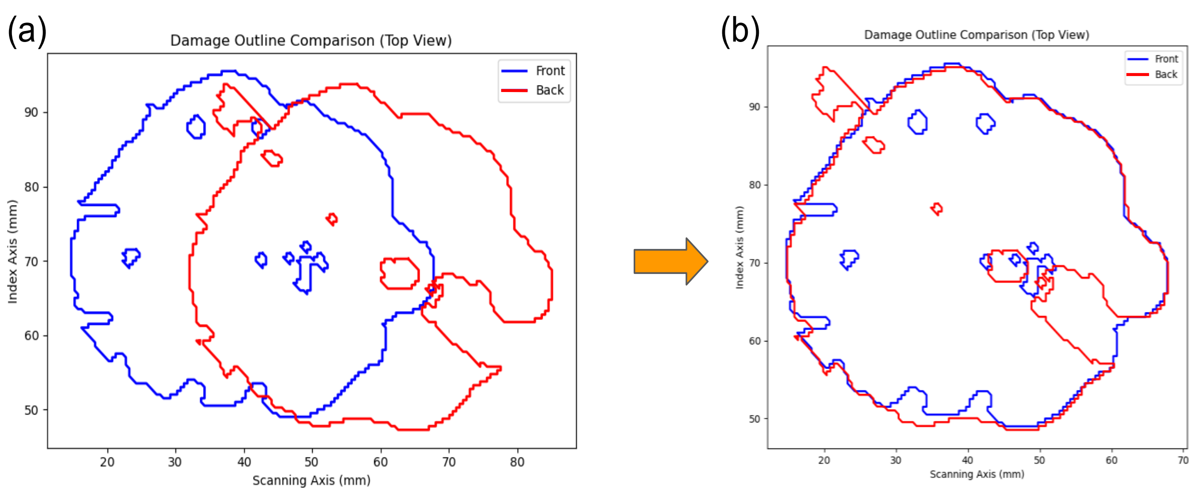


Figure 2.21 Outline alignment: (a) example of outlines without auto and manual alignment, and (b) example of outlines after final auto + manual refined alignment.

Because of the iterative nature of this process, the user can set the variable *Ready* to False, which restricts the code to plotting only the side views and damage outlines for detailed visual inspection prior to merging the data and saving the hybrid dataset. This step also reduces runtime and avoids generating unnecessary figures. Following successful alignment, the front- and back-surface point clouds are merged into a single dataset representing the complete hybrid three-dimensional damage volume. Multiple viewing orientations are saved, including isometric, top, bottom, and side perspectives (see Appendix D for examples), analogous to the visualization approach implemented in `cscan_plots()`. These complementary views facilitate interpretation of the internal delamination morphology and allow to compare the final selected damage to their two-dimensional versions. Additionally, the function exports a summary text file documenting the centroid locations, alignment translations, and processing parameters, thereby ensuring full traceability and reproducibility of the reconstruction procedure. The combined coordinates are saved in a .pk file for future processing.  In summary, this function constitutes the final stage of the three-dimensional reconstruction methodology, integrating independently acquired C-scan datasets into a unified hybrid representation of the internal damage field.

#### *2.2.5.1 Automatic Front-and-Back Plot Alignment*

It is virtually impossible—even for the same specimen—to obtain two C-scans with identical x, y, and z coordinates. Therefore, numerical permutations of the data must be performed before concatenation. That is, the data points from either specimen must be translated in all directions to ensure that the data is fully aligned prior to generating a final hybrid plot. The function `hybrid_cscan_plots ()` translates the back-scan coordinates to align with the original front scan coordinates; however, either scan could have been chosen, as no preference existed between them.

First, automatic alignment is performed in the x-y plane by comparing the corresponding centroid coordinates and using the calculated distance between them as an automatic shift in both the x and the y direction, which is then applied to the Back scan's entire X and Y data arrays, as shown in Figure 2.22.

```
# # # = = = Centroid & Midplane Alignment Section Begins = = = # # #

dx = front_centroid[0] - back_centroid[0]
dy = front_centroid[1] - back_centroid[1]
```

⋮

```
if auto_align:
    X_back_aligned = X_back_flipped + dx
    Y_back_aligned = Y_back_flipped + dy
```

Figure 2.22 Automatic x and y coordinate shift.

The front- and back-surface datasets must also be aligned in the z-direction; otherwise, the hybrid plot will contain delaminations at incorrect depths and duplicate representations of features detected by both scans. Considering the inherent variability of each scan and the difference in size between each data array, automatic z-direction alignment cannot be achieved simply by computing the distance between the scans' centroid z-coordinates and applying the resulting offset to shift the entire Z array, as is performed in the x-y plane. Unlike the x and y directions, the total through-thickness extent of each scan may vary significantly due to the data selection process.

One reason delaminations may appear at inconsistent depth values is that the scans, being performed from opposite surfaces, detect the same delaminations from opposing sides, as seen in Figure 2.23. However, it was observed that each delamination cluster exhibits a measurable thickness in the z-direction, as shown in Figure 2.24, (a), which may provide the basis for a reliable z-direction alignment strategy.

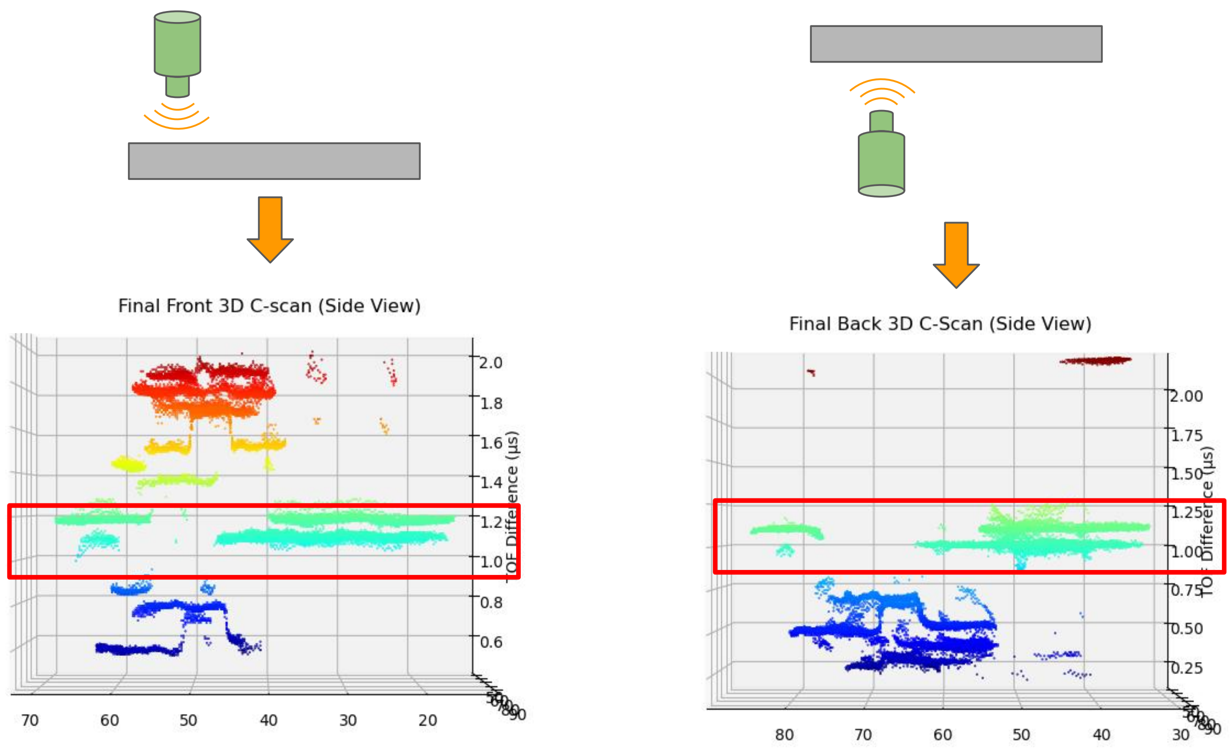


Figure 2.23 Front and Back scan orientations.

Thus, it was determined that the most effective approach to aligning the delaminations in the z-direction is to offset the data by a value corresponding to the average delamination thickness, as shown in Figure 2.24, (b). This value is not fixed or universally defined, as it varies with the material properties, impact energy, and transducer resolution. For a 25-ply, unidirectional IM7/977-3 autoclave-cured carbon fiber/epoxy composite laminate, an offset equivalent to an average delamination thickness of 0.07 µs and 0.2 mm was applied to the ΔTOF and depth three-dimensional plots, respectively.

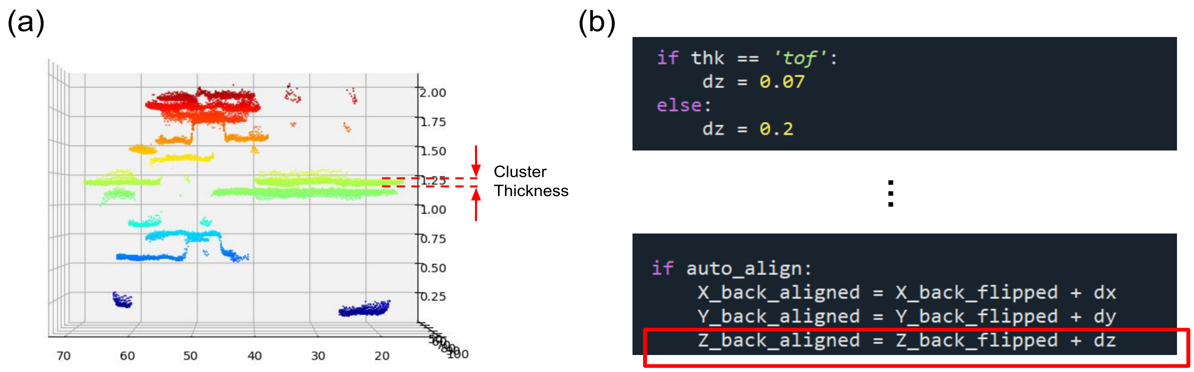


Figure 2.24 Automatic z shift: (a) visual representation of a delamination cluster thickness, and (b) automatic z-shift based on cluster thickness.

### *2.2.5.2 Damage Depth Plots*

Time-of-flight plots provide a clear visual depiction of the position of damage inside a composite. However, in order to derive the exact depth of each delamination within the composite, one can convert the time-of-flight values from the ultrasonic pulse-echo data into measurements of distance relative to the total thickness of the structure. Particularly, the wave speed through the scanned material must be known or calculated, which is then used to derive distance, as shown in Equation 1. Nevertheless, in cases where the wave speed is unknown, the values of ΔTOF can be converted into values of thickness by dividing each value of ΔTOF by the value of TOF representing the total thickness (i.e., *tofd_max*) and multiplying that by the known specimen thickness. By setting the variable *thk* equal to a real value of thickness in millimeters (mm) instead of 'tof' in `cscan_plots()`'s input, as shown in Figure 2.25, the function automatically converts the regular plots of ΔTOF into depth plots, where the z-axis has now units of mm.

```
def cscan_plots(pkfile, save_processed=True, tof1plot = 1, tofdplot = 1, dmg = 1,
                dent = 1, amp1plot = 1, amp2plot = 1, amp3plot = 1, contplot = 1,
                sect_cut = -1, cont_range = [-1.5,1.5], thk = 3.292, Front = True,
                three_d = True, Ready = True):
```

Figure 2.25 `cscan_plots()`: depth plot command.

Hybrid plots can also be generated in terms of physical depth. However, this requires that both the front- and back-surface C-scans are processed using `cscan_plots()` as depth plots, such that the data passed to `hybrid_cscan_plots()` is already expressed in millimeters. Furthermore, as in `cscan_plots()`, the variable *thk* must be set to the same thickness value used when generating each individual scan plot. Doing so produces a hybrid plot with depth measurements, as seen in Figure 2.26, that can be directly related to physical distance measurements within the composite structure under examination. It should be noted that depth values are measured from the back surface upward.

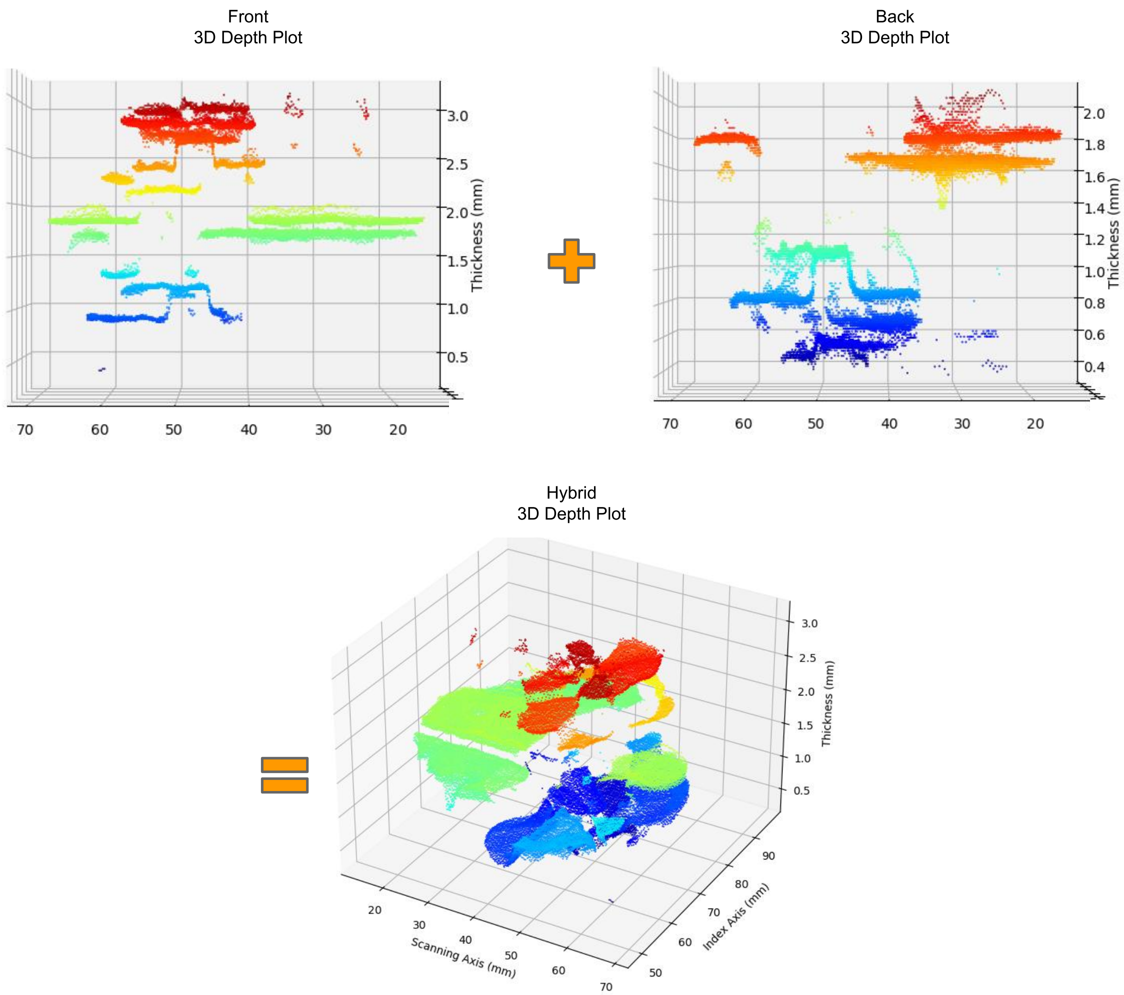


Figure 2.26 Hybrid depth plot example.

### 2.2.6 Delamination Density Maps of 3D C-Scans – `density_plots()`

One objective of this work is to improve the visualization of delamination propagation using reconstructed three-dimensional data. Upon impact, delaminations propagate and interconnect throughout the composite material via matrix cracks. Furthermore, some delaminations may overlap without being directly connected, owing to their ply-angle-driven morphology (Ellison, 2020). Together, matrix cracks and delamination overlaps form a pattern referred to hereafter as the delamination network branches (DNBs). The `density_plots()` function analyzes C-scan data to produce density maps of delaminations, shown in Figure 2.27, which are specifically designed to highlight and reveal these damage branches.

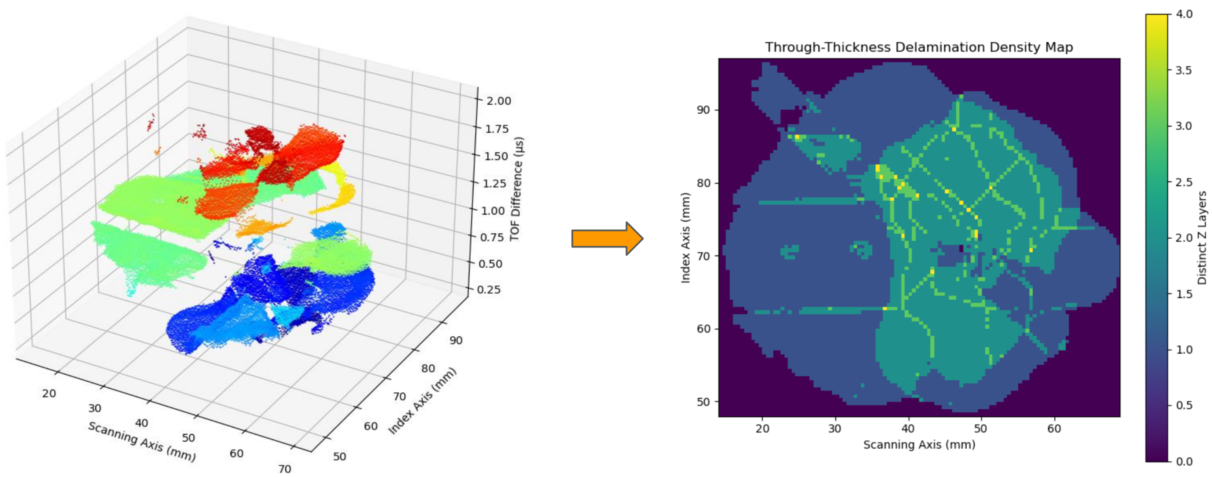


Figure 2.27 Delamination density map example.

Notably, this function can also process hybrid datasets, which contain DNBs from both the top and bottom surfaces, providing important information for the placement of injection holes, as these regions may serve as percolation pathways through which the repair resin can travel and infiltrate the damaged laminate, as illustrated in Figure 2.28.

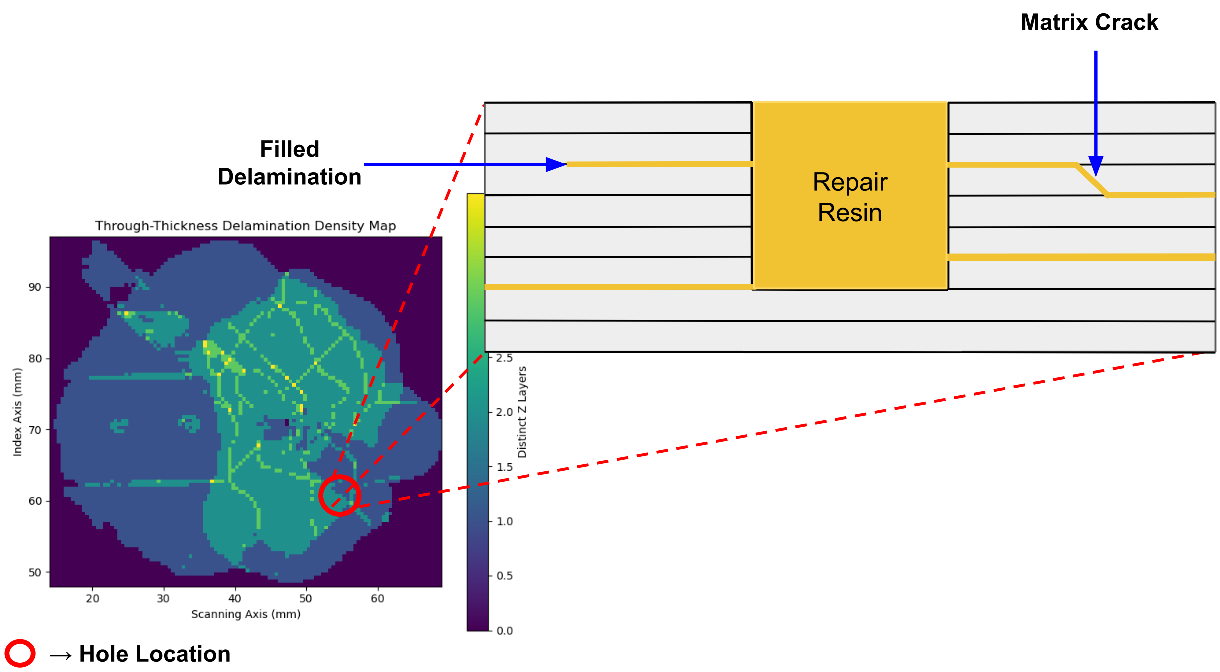


Figure 2.28 Ideal hole placement diagram.

More specifically, the `density_plots()` function can generate two-dimensional density maps from the three-dimensional ultrasonic dataset produced by either `hybrid_cscan_plot()` or `cscan_plots()`. The input data, stored as a .pk file, consist of the spatial coordinates (X, Y, Z) corresponding to the location of internal damage features within the composite laminate. The function first imports and separates the coordinate data and subsequently partitions the scanned region into a user-defined Cartesian grid. The auxiliary function `compute_delamination_grid()`, evaluates the local damage distribution within each grid cell by quantifying the number of distinct through-thickness delamination layers. The resulting damage layer count values generated in the auxiliary function are then visualized as two-dimensional color maps, where each color represents a local concentration damage layers. Additionally, `density_plots()` includes an optional coordinate transformation that translates the scanning coordinates with respect to a user-defined reference point on the structure, enabling the generation of density maps in an alternative coordinate system.

#### *2.2.6.1 Delamination Density Map* – `compute_delamination_grid()`

The `compute_delamination_grid()` function quantifies the spatial distribution of internal damage by discretizing the scanned region into a two-dimensional Cartesian grid and evaluating the through-thickness structure within each grid cell. First, the spatial domain defined by the X and Y coordinates is partitioned into uniformly spaced cells of size *grid_res*. Each data point is then assigned to its corresponding grid cell using a binning procedure based on its in-plane coordinates. The variable *grid_res* is a user-defined input, and it should vary depending on the scan's resolution as this determines how spaced-out data points are. For example, for a scan with a resolution of 0.25 mm, the grid resolution should be higher than 0.25 mm in order to capture at least one data point per grid cell. The larger the grid cells, the more data points will be assigned to each grid cell; however, larger grid cells lead to plots with lower resolution.

For each cell, the associated through-thickness coordinates, $Z_{local}$, are extracted and sorted in ascending order. The algorithm subsequently identifies distinct damage layers by examining the spacing between consecutive points along the thickness direction. Whenever the separation between two adjacent points exceeds a user-defined threshold, $z_{tol}$ , a new layer is assumed to exist. The value of $z_{tol}$ is another user-defined variable and it should be adjusted to the structure in question. In theory, the lowest value of $z_{tol}$ should be equal to one-ply thickness since that is the closest two delaminations will ever be due to the material's inherent discontinuity. The total number of layers within the cell is obtained by counting the number of such damage layers and adding one to account for the initial layer, as defined by Equation 11.

$$N_{layers} = 1 + \sum_{i=1}^{n-1} \begin{cases} 1, & if \;\; z_{i+1} - z_i > z_{tol} \\ 0, & otherwise \end{cases} \qquad \text{Eq. 11}$$

where $z_i$ and $z_{i+1}$ are consecutive sorted through-thickness coordinates, $z_{tol}$ is the threshold used to distinguish adjacent delamination interfaces, and n is the number of ultrasonic data points contained within the grid cell. This criterion enables the algorithm to identify multiple damage layers within a single grid cell while accounting for small variations in the measured data.

The resulting layer count is stored in a two-dimensional array, referred to as the layer grid, in which each element represents the number of distinct through-thickness damage layers present at a given in-plane location. The function returns both the computed grid and the corresponding grid boundaries, which can subsequently be used to generate density maps and visualize the spatial distribution of delamination throughout the laminate.

## 2.3 Experimental Setup

### 2.3.1 Tank-Less Pulse-Eco Ultrasonic Testing Setup

Traditionally, the PZT probe is submerged in a couplant-filled tank to provide optimal wave transmission. However, the C-scan setup used in this work employed an innovative tankless configuration, shown in Figure 2.29, inspired by a previous model developed by NASA Langley Research Center. This approach utilizes a compact adapter that encloses the PZT probe while maintaining effective acoustic coupling. The bottom of the adapter is a flexible membrane made of an impermeable polymer thin film (nitrile glove). Moreover, the surface of the scanned specimen must contain a layer of water to allow for the ultrasonic waves to propagate efficiently through the membrane and into the specimen without full immersion. An NDT System IAHG052 10MHz transducer is used for signal generation, a Mistras/NDT Automation 1682 control box is used for 2-degree-of-freedom translation, and the Pocket UT system is used to control motion and store the scan data.

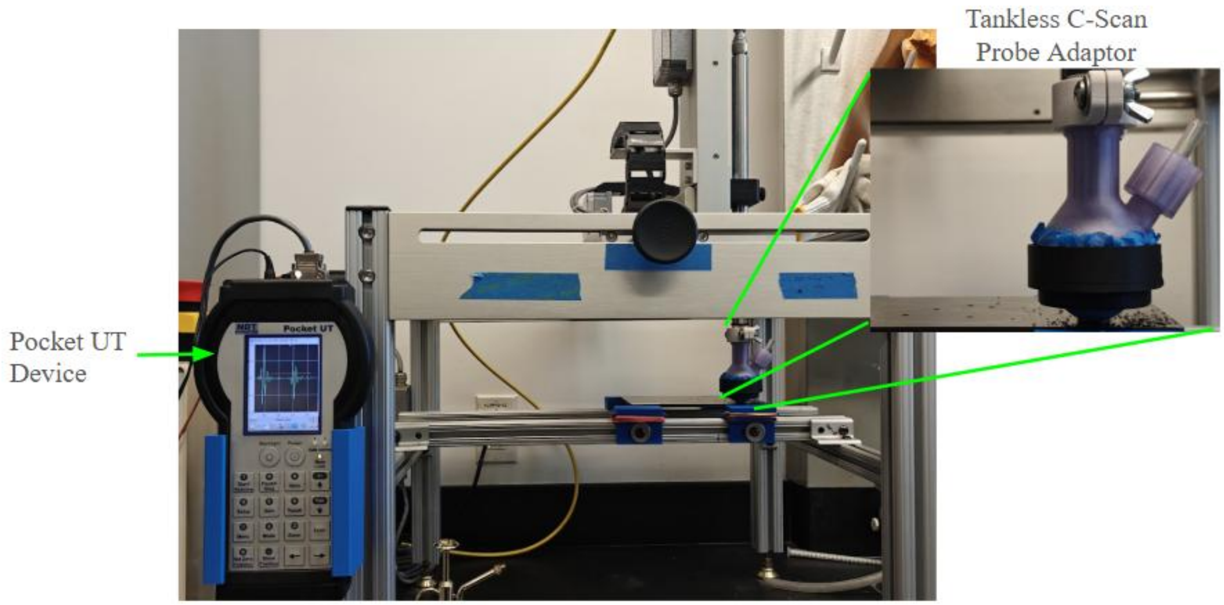


Figure 2.29 Tankless C-scan setup.

A remarkable feature of this setup is the augmented signal reflection from the back surface of the specimen. This effect is caused by the higher acoustic impedance mismatch created at the back of the specimen, which is now exposed to air—air is assumed to have a dynamic stiffness close to zero. Therefore, a greater portion of the ultrasonic wave is preserved and reflected off the back of the specimen resulting in higher amplitudes corresponding to the back surface (Delaney, 2026).

### 2.3.2 Experimental Procedure

The specimens were scanned with the longest side oriented in the x-direction and the shortest side in the y-direction of the scanner fixture. The placement of the specimen is arbitrary, provided that the correct dimensions are entered into the Pocket UT. Note that the x and y dimensions are labeled as index and scan, respectively, in the Pocket UT. A 10 MHz transducer was used, with a raster resolution of 0.25 mm, a scanning speed of 35 mm/s, and a gain of 12.2 dB.

The specimens were clamped onto the T-slotted bar frame in the desired position and the transducer was positioned at any point on the pristine surface of the specimen such that the second peak of the reflected ultrasonic wave corresponds to a TOF of 35 μs, thereby establishing a consistent standoff distance of approximately 1 inch between the transducer and the specimen surface, as seen in Figure 2.29. The width and length of each specimen were then recorded and entered in the C-scan configuration tab of the Pocket UT. The dimensions of any specimen can be determined by traversing the transducer to its farthest corner and recording the corresponding x and y coordinates — labeled as index and scan in the Pocket UT. Finally, after confirming that the resolution and scanning speed are set up correctly, the scan may be initiated.

Prior to scanning, tape markers were placed on both the front and back surfaces of the specimen, as shown in Figure 2.30. The bottom-left corner of the bottommost marker is used as the reference origin, which is essential for translating the C-scan coordinates to the physical specimen. The remaining two tape markers are used to define a known distance, which can be used to spatially calibrate the damage images. The distances and size of the markers should be adjusted such that they do not obstruct the damage region while their outlines still appear in the two-dimensional C-scan plots, as seen in Figure 2.31. All three markers are excluded from the damage network during the three-dimensional reconstruction.

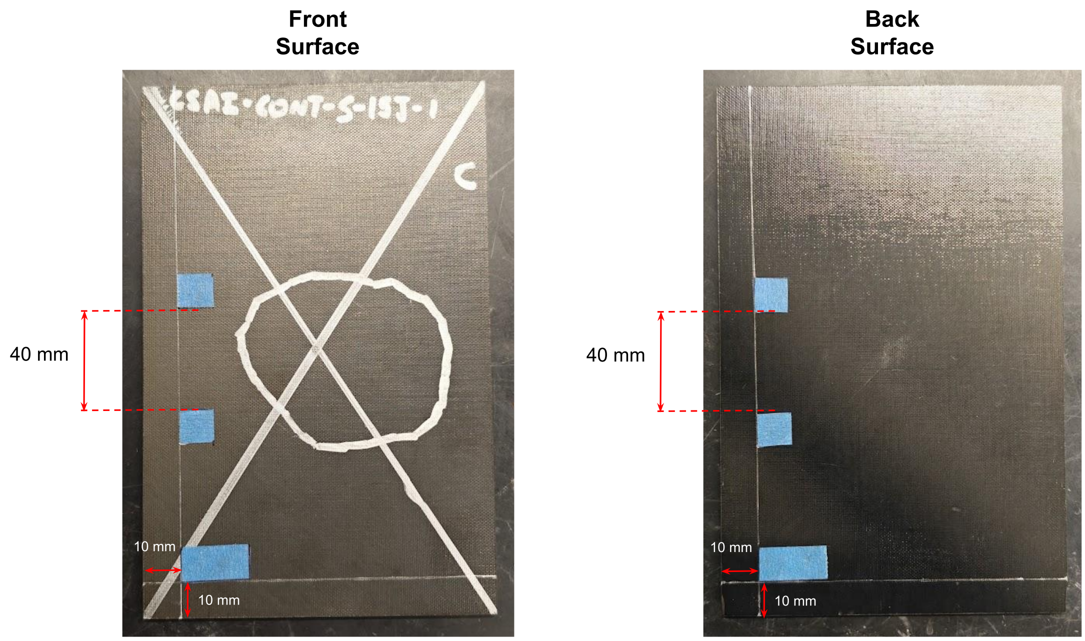


Figure 2.30 Marker placement diagram.

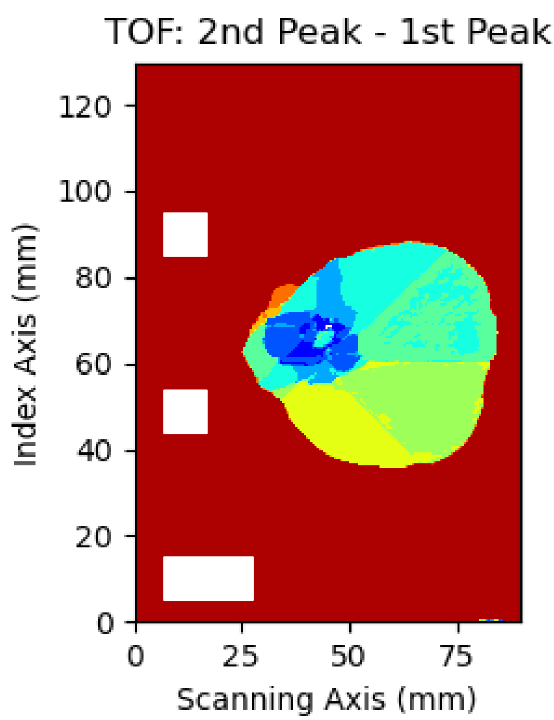


Figure 2.31 Marker outlines present on ΔTOF C-scan.

#### 2.3.3 Specimen Information

The Python code is material-independent, as it processes all C-scan data uniformly. However, for the specimens analyzed in this thesis, the results correspond to 25-ply IM7/977-3 autoclave-cured carbon fiber/epoxy composite laminates. Each specimen is nominally 102 mm wide and 152 mm long, with the 0° ply oriented parallel to the longest side. The specimens were fabricated with three layup configurations of varying effective modulus, as shown in Table 2.1, and were impacted at three energy levels: 10 J, 15 J, and 20 J. Additionally, three post-scan fabrication conditions were applied to each specimen upon completion of the C-scans, as indicated by the specimen designation in Table 2.2. These labels define the specimen naming convention. Therefore, the naming convention for all specimens was determined in accordance with the following convention (Romasko, 2022).

CSAI-**A-B-C-D**, where

**A**: BL, RPR, or CONT condition

**B**: H, M, or S panel type

**C**: Impact Energy Level (in Joules)

**D**: Specimen number (1-3)

Example: CSAI-**BL-H-10J-1**

Table 2.1 Ply layups and stiffness of samples.

| **Layup Type** | **Ply Layup** | **Effective Modulus (GPa)** |
|---|---|---|
| H (hard) | [45/-45/0/0/45/-45/0/0/45/-45/0/0/90]s | 114.0 |
| M (medium) | [45/-45/0/0/45/-45/0/45/-45/0/45/-45/90]s | 79.2 |
| S (soft) | [45-/45/0/45/-45/90/45/-45/0/45/-45/90/90]s | 58.6 |

Table 2.2 Fabrication conditions and abbreviations.

| **Fabrication Condition** | **Abbreviation** |
|---|---|
| Baseline Unrepaired | BL |
| Surface prepped and repaired | RPR |
| Contaminated, surface prepped, and repaired | CONT |

## 2.4 Results

The Python code developed in this thesis generates two-dimensional and three-dimensional C-scan plots, depth plots, hybrid three-dimensional plots, and delamination density maps. This section presents the processed three-dimensional ΔTOF C-scans and delamination density maps for specimens injected as part of the injection repair development process. Additionally, a correlation study is presented in which the branches identified in the delamination density maps were verified to correspond to matrix cracks within an impacted specimen.

### 2.4.1 3D C-Scans

A total of five CFRP composite specimens were scanned before and after injection repair to document evidence of damage restoration using nondestructive evaluation. Figures 2.32 to 2.36 present the pre- and post-injection C-scan results for each specimen and demonstrate the robustness of the Python code, which yielded consistent and reliable results across specimens with varying laminate layup configurations, impact energies, and damage sizes.

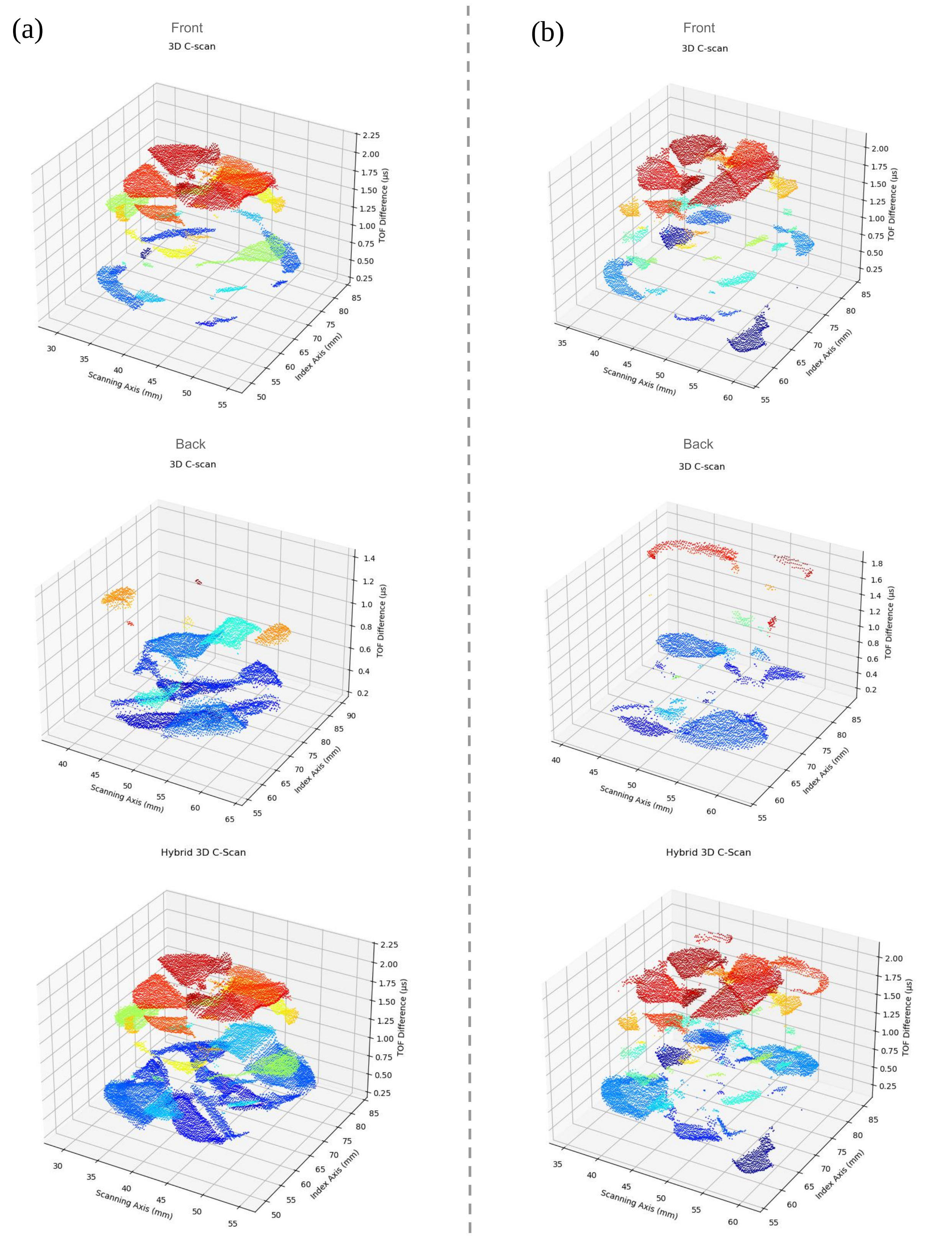


Figure 2.32 Specimen CSAI-RPR-HARD-10J-1: Front, Back, and Hybrid 3D C-scans (a) **before** and (b) **after** injection repair.

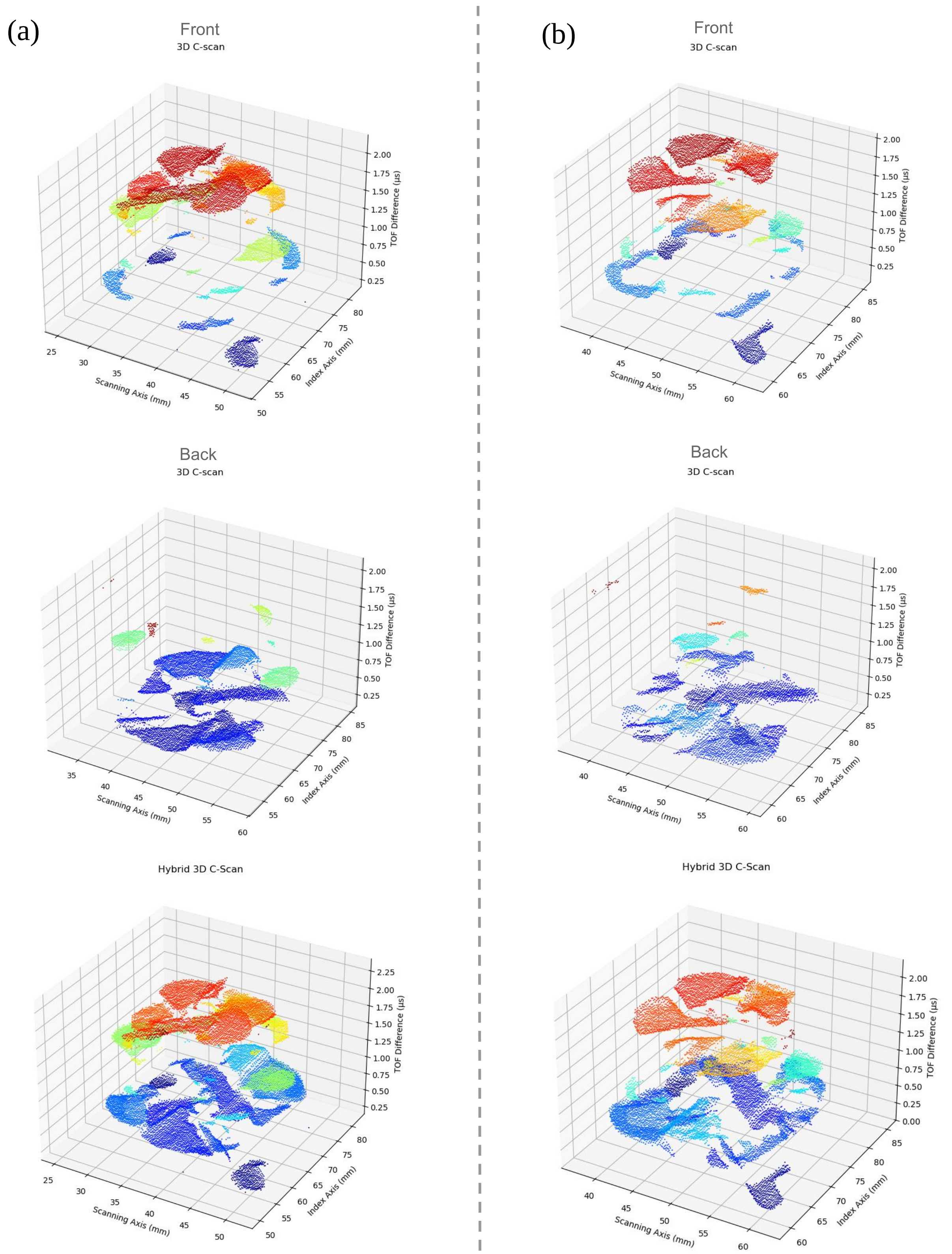


Figure 2.33 Specimen CSAI-CONT-HARD-10J-1: Front, Back, and Hybrid 3D C-scans (a) **before** and (b) **after** injection repair.

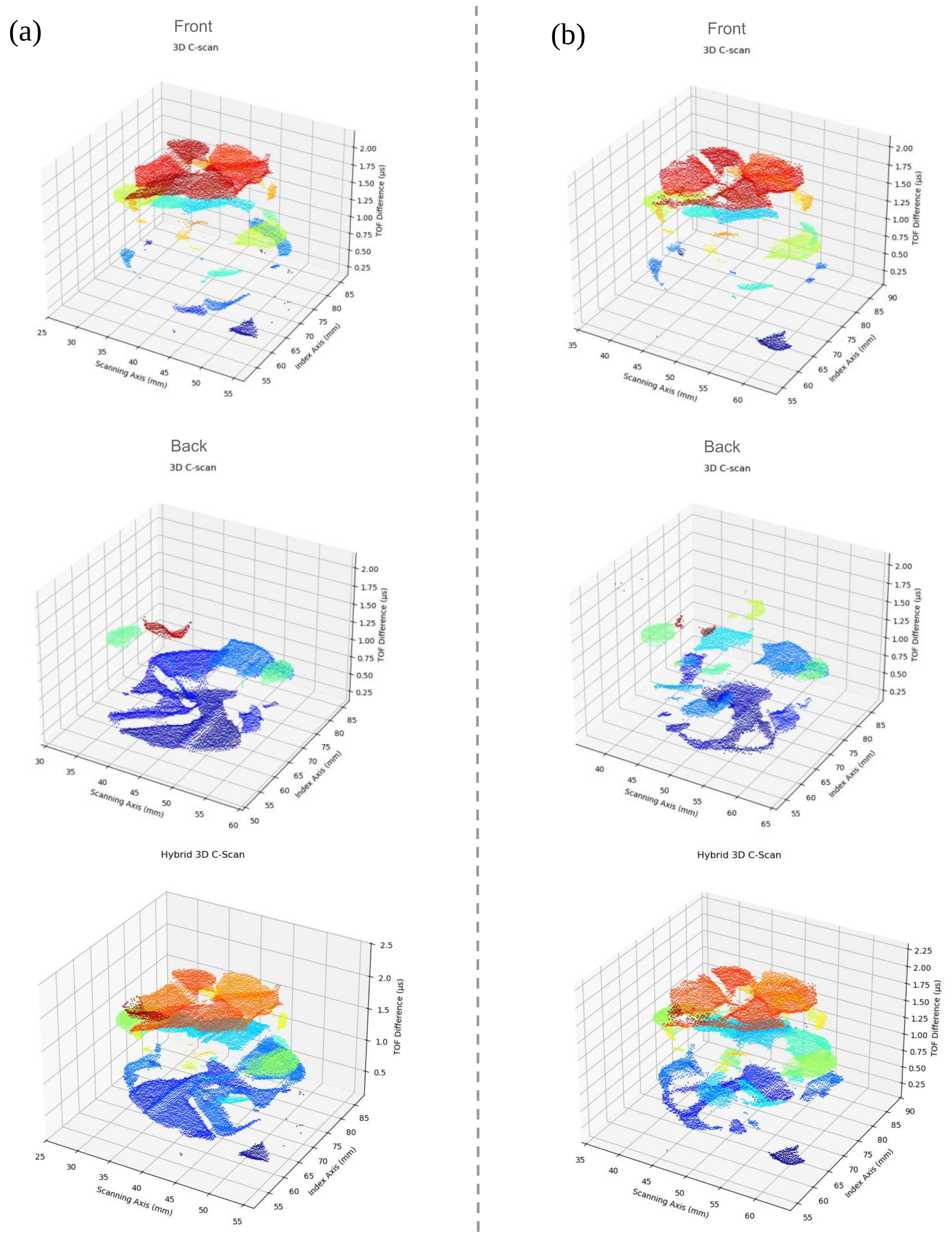


Figure 2.34 Specimen CSAI-RPR-HARD-10J-3: Front, Back, and Hybrid 3D C-scans (a) **before** and (b) **after** injection repair.

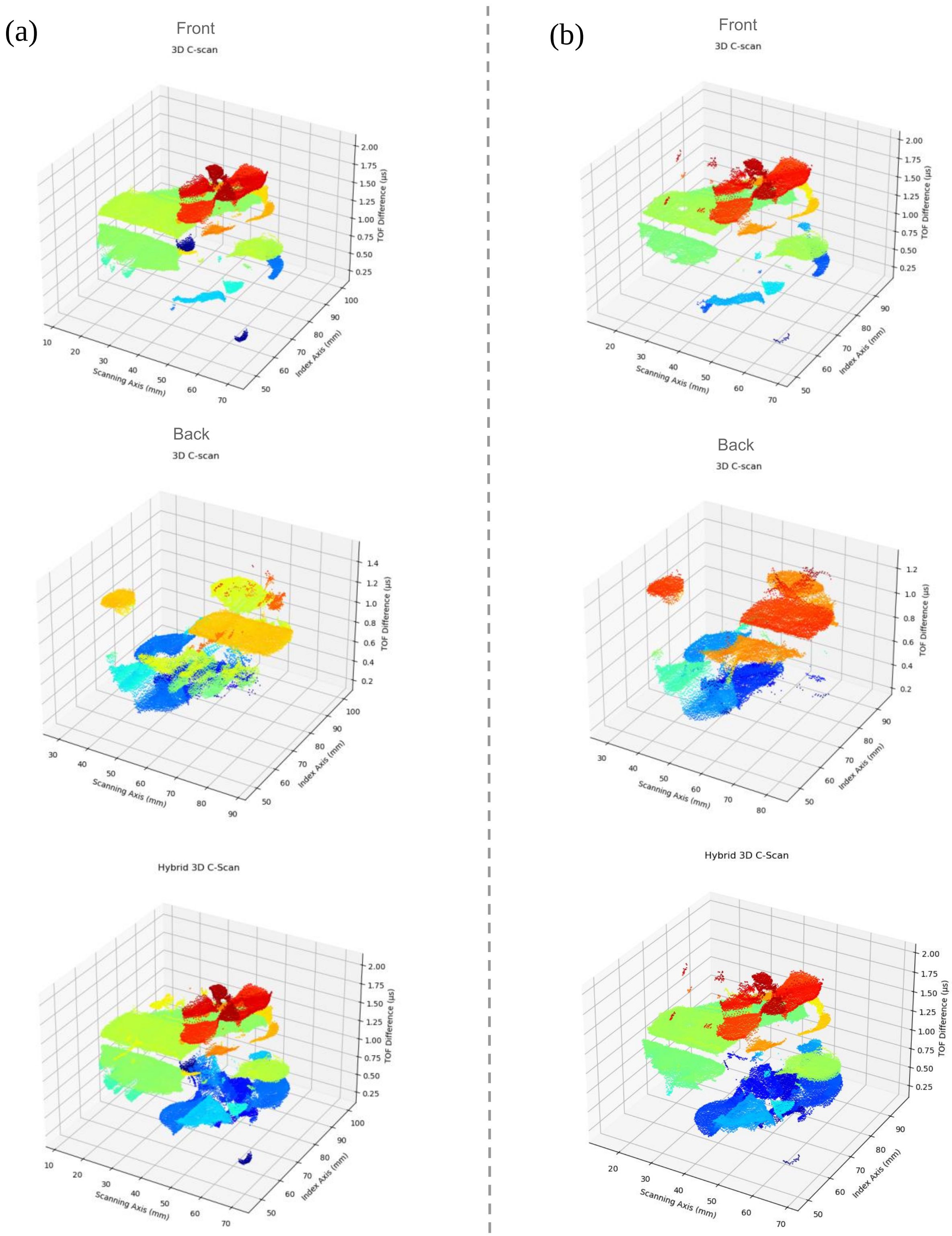


Figure 2.35 Specimen CSAI-RPR-HARD-20J-1: Front, Back, and Hybrid 3D C-scans (a) **before** and (b) **after** injection repair.

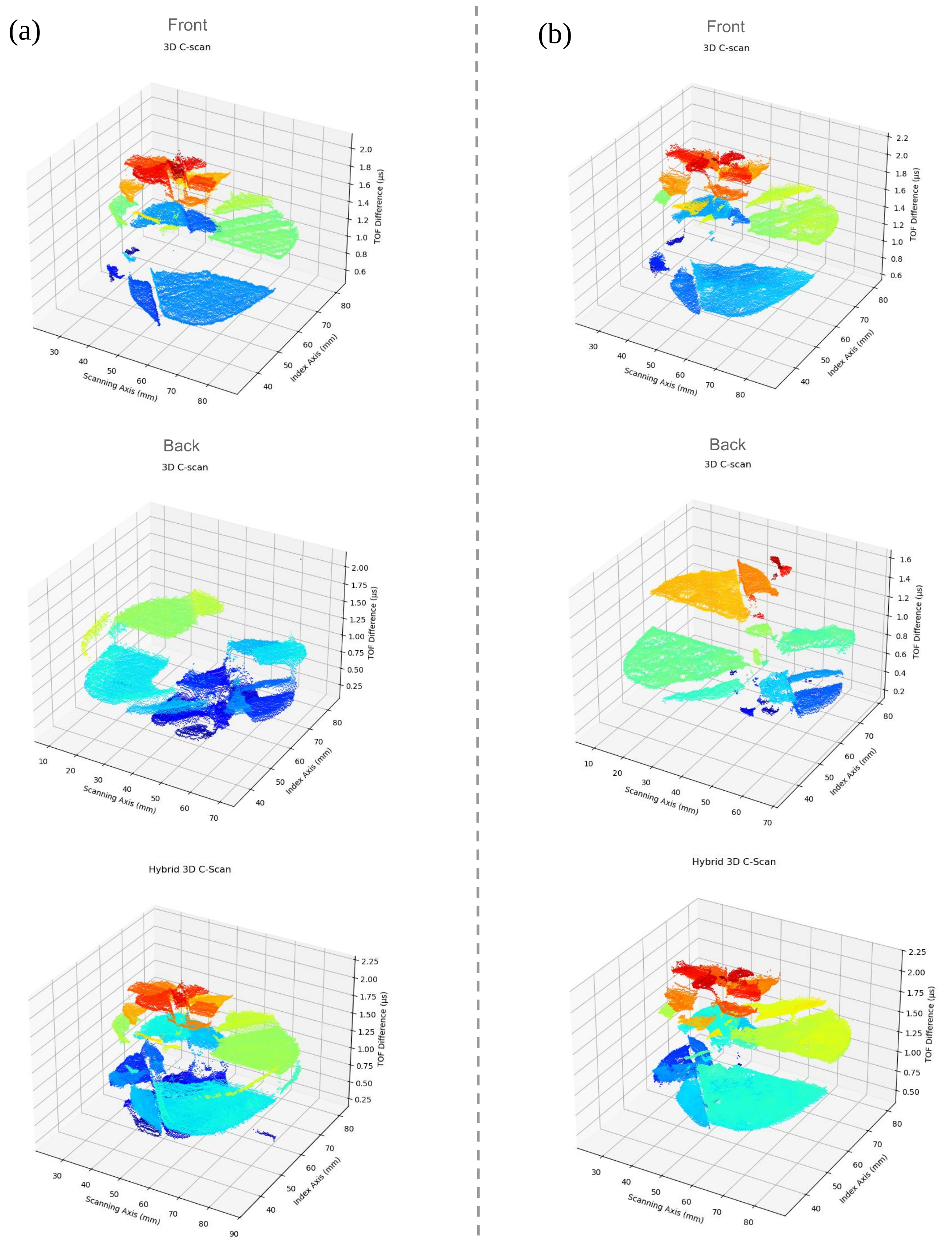


Figure 2.36 Specimen CSAI-RPR-SOFT-15J-1: Front, Back, and Hybrid 3D C-scans (a) **before** and (b) **after** injection repair.

Combining the datasets from the front- and back-surface scans into a hybrid plot captures the damage network more completely than either individual scan alone. Upon reconstruction, the lowermost delaminations are revealed, thereby mitigating the shadowing effect (although not entirely). Furthermore, successful alignment in all directions is confirmed by the absence of duplicate delaminations.

As seen more clearly in Figure 2.32 to 2.34, following injection, some of the deeper delaminations exhibit a reduction in size and a change in outline. This is attributed to the repair resin having infiltrated portions of the delamination void, enabling the ultrasonic wave to propagate through the previously voided region and therefore registering as an absence of damage in the post-injection scan.

### 2.4.2 Density Maps

Similarly, each of the five CFRP specimens has a corresponding delamination density map acquired before and after injection repair. In all cases, the plots highlight the delamination network branches, which manifest as regions of elevated delamination count. In practice, what the code effectively detects are layers of data points that fall within a defined proximity threshold ($z_{tol}$). It is worth noting that the density maps exhibit anomalously elevated damage layer counts, which in theory should not exceed two for any given hybrid plot. Counts above this threshold arise for two reasons: first, more than one scanning coordinate may be captured within a single grid cell depending on the spatial resolution of the scan; and second, some of the detected damage layers represent matrix cracks, given that delaminations do not propagate within the fibers themselves, but matrix cracks do.

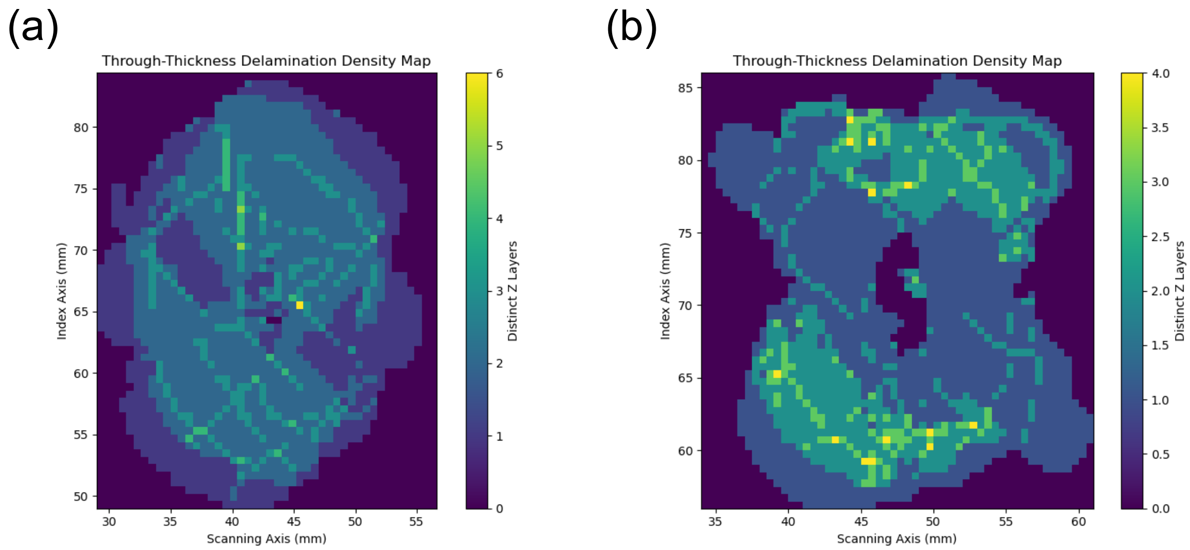


Figure 2.37 Specimen CSAI-RPR-HARD-10J-1: Delamination density map (a) **before** injection, and (b) **after** injection.

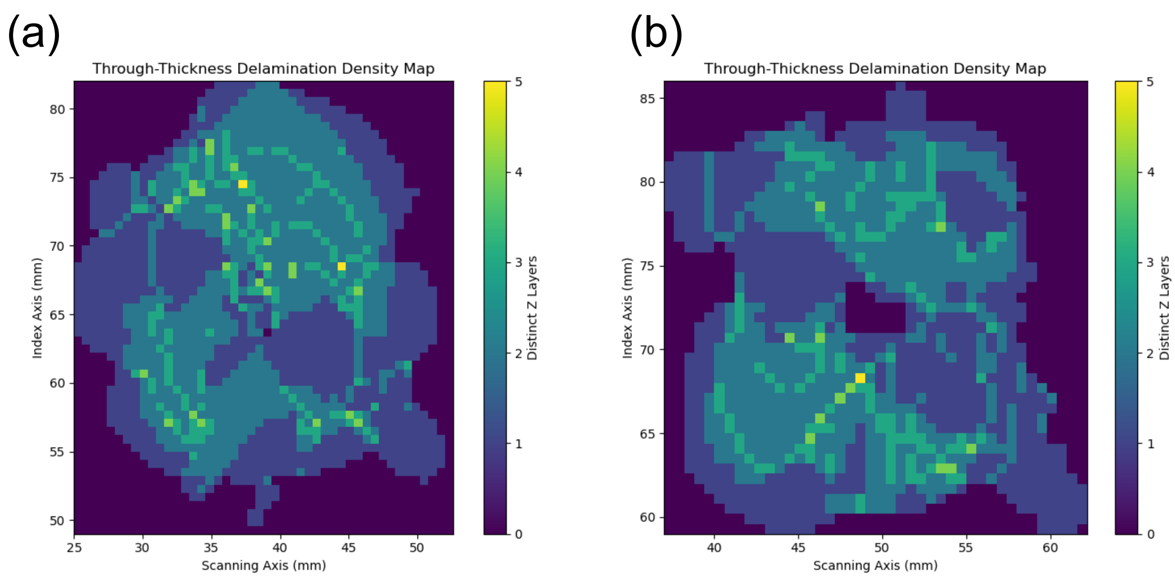


Figure 2.38 Specimen CSAI-RPR-HARD-10J-1: Delamination density map (a) **before** injection, and (b) **after** injection.

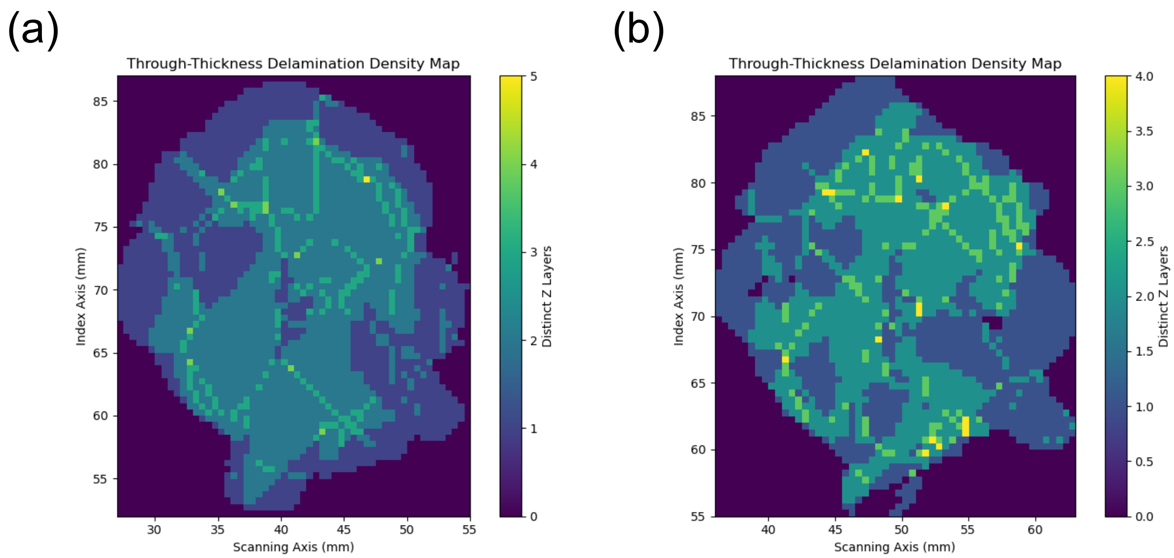


Figure 2.39 Specimen CSAI-RPR-HARD-10J-3: Delamination density map (a) **before** injection, and (b) **after** injection.

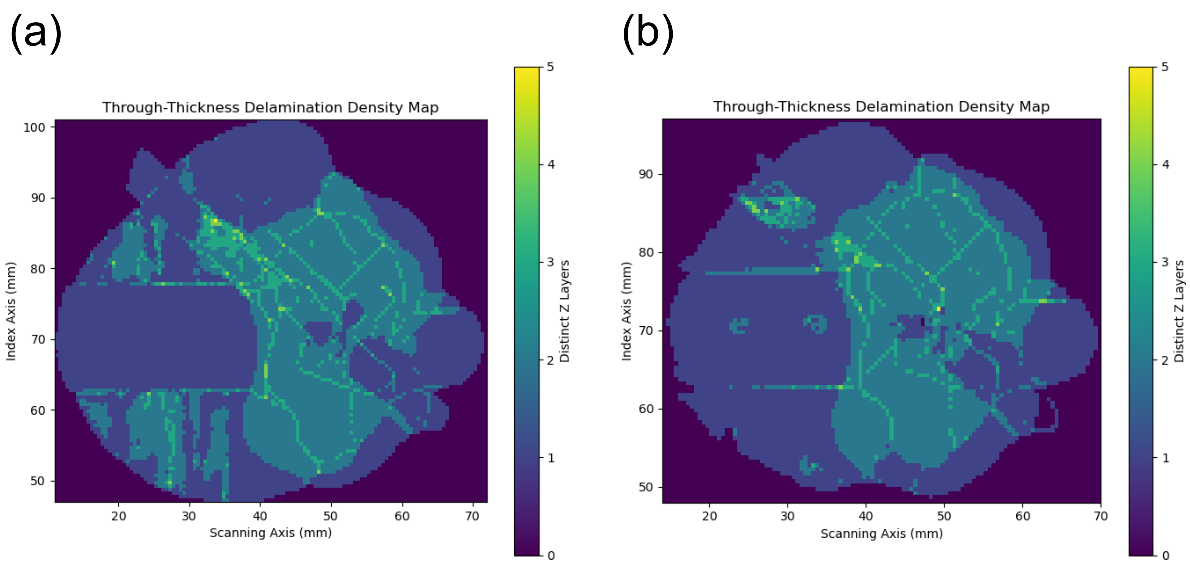


Figure 2.40 Specimen CSAI-RPR-HARD-20J-1: Delamination density map (a) **before** injection, and (b) **after** injection.

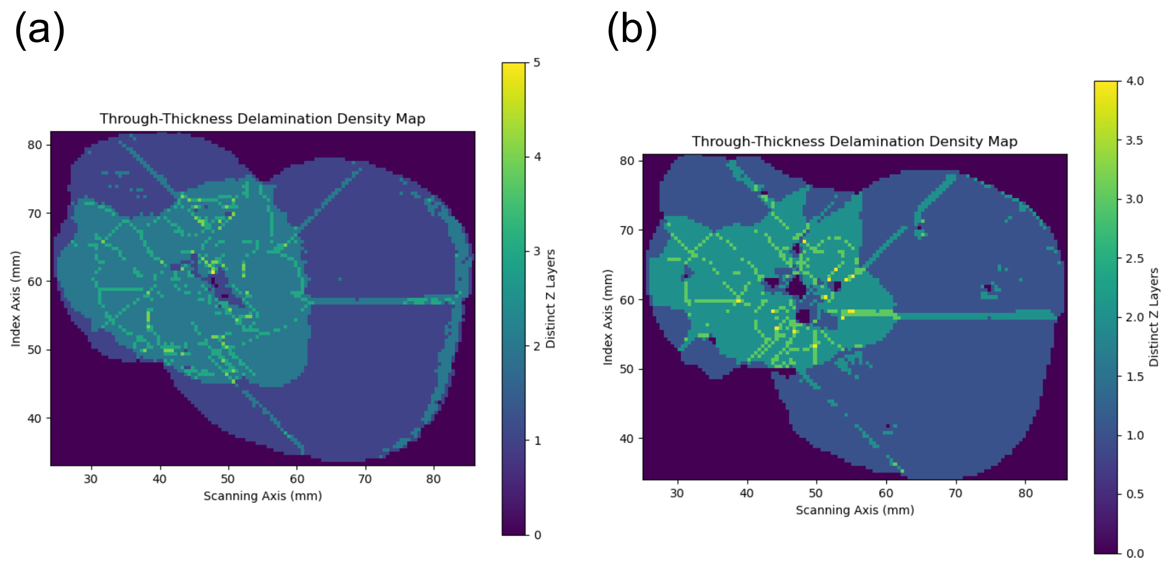


Figure 2.41 Specimen CSAI-RPR-SOFT-15J-1: Delamination density map (a) **before** injection, and (b) **after** injection.

Figures 2.37 to 2.39 show significantly different damage outlines and network branches after injection, attributed to the repair resin infiltrating the delaminations and matrix cracks, resulting in fewer branches being detected. Nevertheless, specimen CSAI-RPR-HARD-10J-1 shows an increase in overall damage area, which contradicts the expected reduction in detected damage associated with resin infiltration. This is primarily attributed to inconsistencies in the C-scan acquisition settings and post-processing parameters. As shown in Figure 2.37 (a), some delaminations may have been excluded from the damage selection process performed during three-dimensional plot generation by `cscan_plots()`, which operates independently of the density plotting function, as the latter uses already-processed three-dimensional C-scan data.

In Figures 2.40 to 2.41, where the damage networks are considerably larger, a significant proportion of the network branches are preserved after injection, indicating poor resin infiltration. Conversely, some regions exhibit lower delamination counts following injection, indicative of successful resin infiltration.

### *2.4.2.1 Density Plot vs. Microscopy Correlation*

The detection of matrix cracks and delamination overlaps emerged as a byproduct of developing the delamination density plots. In theory, due to the shadowing effect, a hybrid C-scan can detect a maximum of two delaminations per grid cell — the first reflection from each of the front- and back-surface scans. However, the delamination density maps reveal anomalously elevated delamination counts in localized regions of the damage zone. These regions could correspond to where an upper delamination terminates and connects to an adjacent lower delamination through a matrix crack. To verify that the delamination network branches identified in the density maps correspond to matrix cracks and delamination overlaps, one of the impacted specimens was sectioned and analyzed at a region where, based on the delamination density map, there should be a matrix crack, as seen in Figure 2.42. The cut was done at approximately 43.5 mm in the y (index) direction.

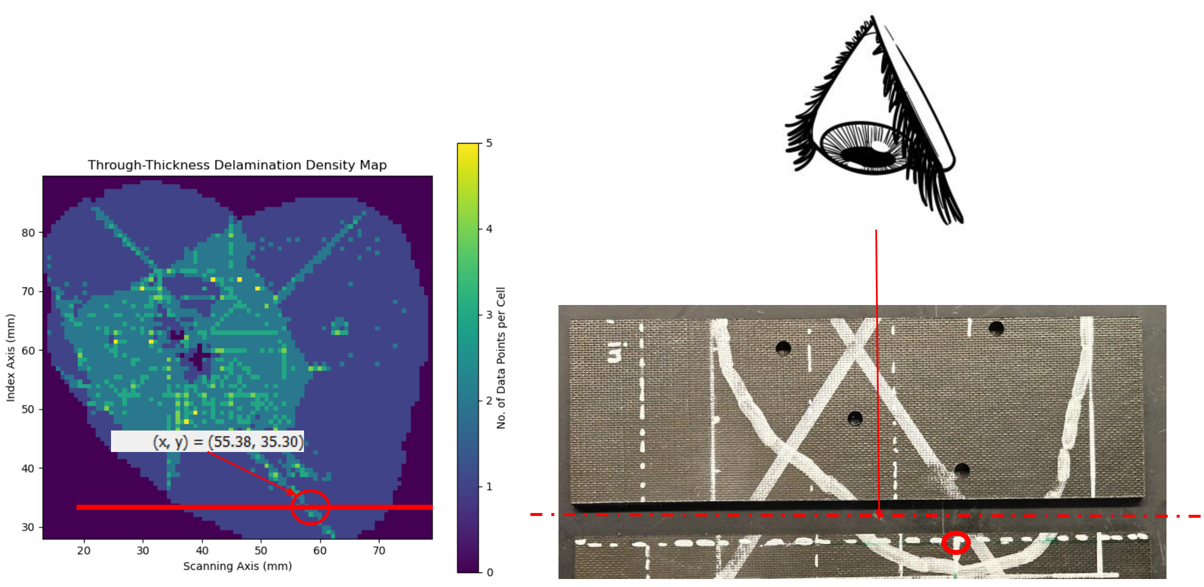


Figure 2.42 Specimen CSAI - RPR - S - 20J – 1: Section cut at y ~ 43.5 from reference origin.

To better visualize the damage within the region of interest, a B-scan was extracted from the hybrid dataset over the range 44 mm ≤ y ≤ 46 mm, as shown in Figure 2.43 (top right), which more clearly reveals the delamination branch under analysis.

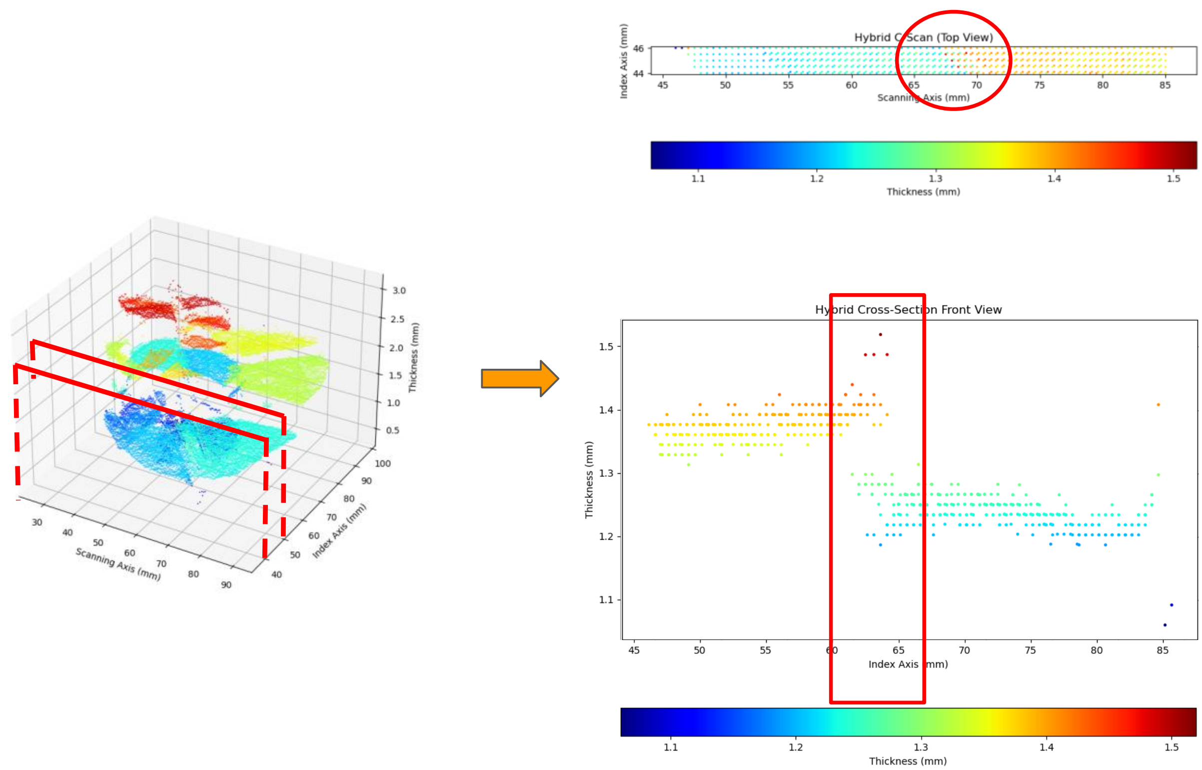


Figure 2.43 2-mm-wide B-scan of Specimen CSAI - RPR - S - 20J – 1: Top (top right) and front (bottom right) views at y ~ 43.5 mm from reference origin.

Figure 2.44 shows a micrograph of the composite specimen at the region of interest, revealing a pair of delaminations connected by a matrix crack, consistent with the delamination network branches identified in the density map. Furthermore, the delamination depths from the micrograph correspond to the depth readings obtained from the hybrid C-scan, with the uppermost delamination located approximately 1.32 mm and the lowermost approximately 1.20 mm from the back surface of the specimen. Ultimately, these results prove that the DNBs from the delamination density maps successfully highlight matrix cracks within the impacted composite, and that the readings of damage depth from the three-dimensional C-scans match the true spatial position of BVID in composites.

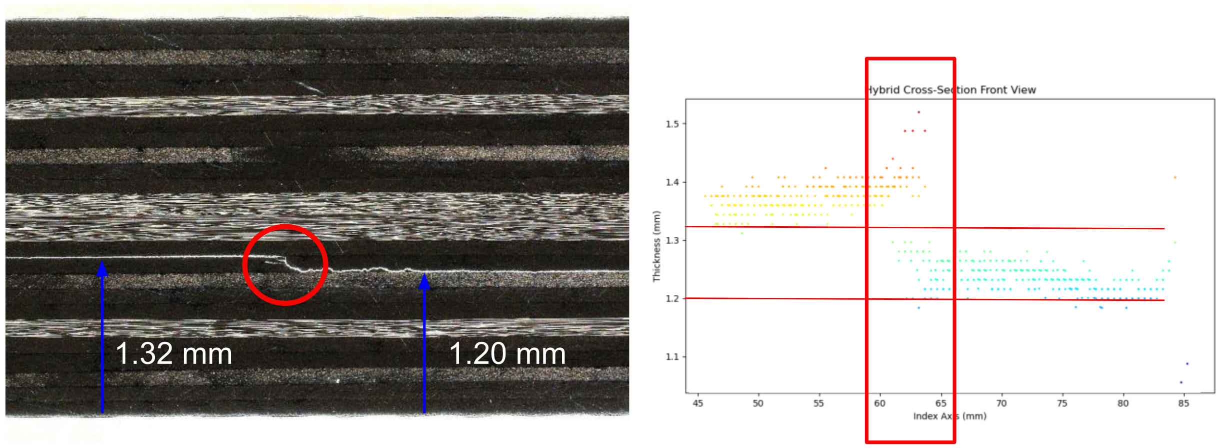


Figure 2.44 Matrix Crack in Specimen CSAI - RPR - S -10J -1: (a) B-scan at y ~ 33.5 mm, and (b) cross-section micrograph of composite at x~ 55.4 mm, y ~ 33.5mmx.

# CHAPTER 3: DRILLING OF IMPACT-DAMAGED LAMINATED COMPOSITES

In relation to injection repair, the results of Chapter 2 guide the decision on where to place holes relative to internal damage, as determined by the ultrasonic C-scan data visualization. This chapter is focused on achieving high-quality holes while removing debris during the drilling operation. The shape, depth, and quality of the drilled holes are crucial in the injection repair process. If the hole is too shallow, the deepest delaminations are not reached; if the hole is too deep, the repair resin may leak through the back surface of the part. Furthermore, if the drill bit is dull or abrasive, it may cause surface fraying and chipping, creating surface irregularities that impede resin penetration. Critically, improper drilling technique can introduce additional delaminations to the composite. An additional concern is debris contamination, which can clog the resin flow pathway from the drilled hole into the pre-existing delaminations and accumulate at the base of the hole. Tool geometry is equally important, as the goal is for the hole geometry to maximize contact with the delamination network. In summary, holes drilled for injection repair should exhibit a rectangular geometry to allow complete surface coverage, should not induce further damage to the composite, should terminate approximately two plies from the back surface to contain the repair resin, and should be free of accumulated composite particles or debris upon completion of machining, as illustrated in Figure 3.1. The work presented in this thesis provides novel contributions to the drilling process that successfully address the aforementioned concerns.

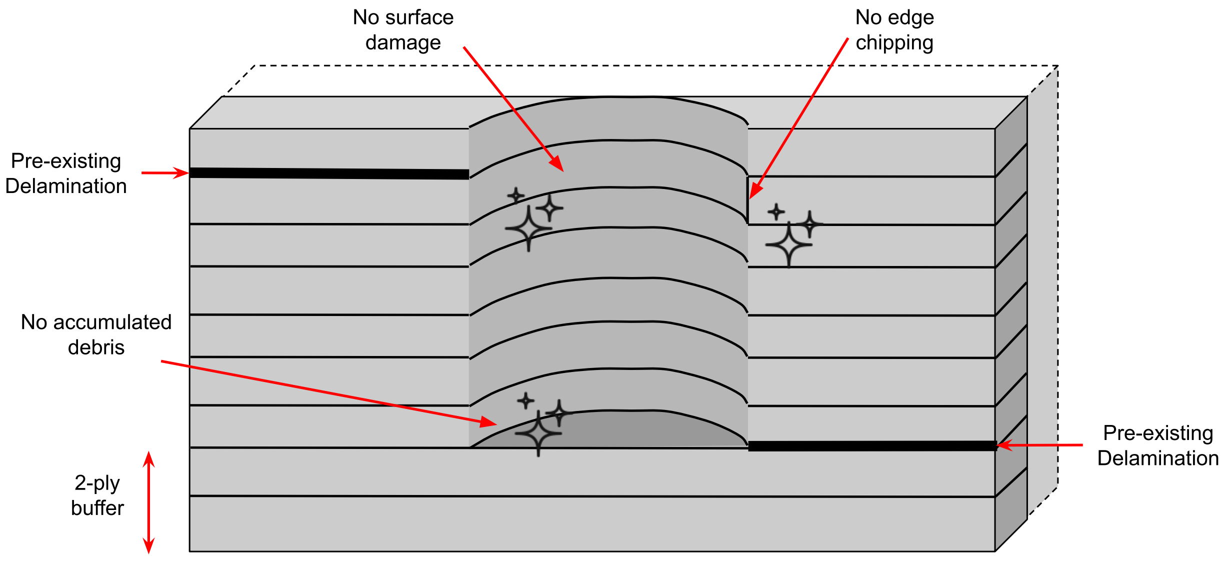


Figure 3.1 Cross-section diagram of an ideal drilled hole for delamination injection repair.

## 3.1 Drilling Physics

### 3.1.1 Drilling Mechanics

Understanding the mechanics behind drilling is paramount for its quality improvement and optimization. In composites specifically, knowledge of the governing mechanics and the parameters that influence them is critical to account for drilling-induced damage modes that are unique to these materials. In industrial practice, the twist drill remains one of the most widely used drill bit types, particularly in the United States. Consequently, many of the analytical models in the literature are derived from this geometry, from which analogous models for alternative drill bit types can be extended. Figure 3.2 illustrates the geometry of a typical twist drill, which serves as the geometric basis for most other drill bit designs (Ismail & Dhakal, 2018).

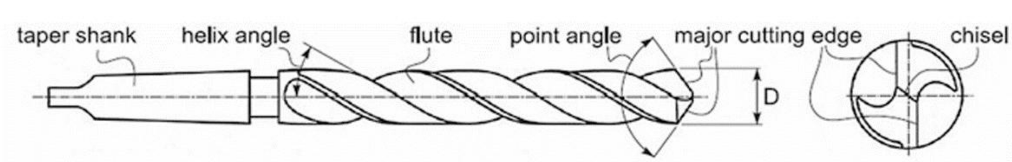


Figure 3.2 Standard geometry of a twist drill (Ismail & Dhakal, 2018).

Drilling is a material removal process in which a rotating cutting tool — the drill bit — is advanced into a workpiece under an applied axial thrust force. The cutting action is driven by the helical flutes and sharp cutting edges of the bit, which shear chips away from the workpiece material as the tool rotates and advances (Ismail & Dhakal, 2018).

The primary governing parameters of drilling mechanics are cutting speed, feed rate, and thrust force. Cutting speed refers to the velocity at which the outer periphery of the tool moves relative to the workpiece surface due to the tool's rotation, typically expressed in mm/s. The relationship between peripheral velocity and rotational spindle speed is given by Equation 12:

$$V = \frac{\pi D S}{1000} \qquad \text{Eq. 12}$$

where V is the peripheral velocity in mm/s, D is the drill bit diameter in meters, and S is the spindle speed in revolutions per minute (rpm). The spindle speed is usually the parameter controlled by the machinist, and for a target peripheral velocity, is therefore defined by Equation 13:

$$S = \frac{1000V}{\pi D} \qquad \text{Eq. 13}$$

Feed rate — arguably the most critical parameter in composite drilling — describes the axial rate at which the drill bit advances into the workpiece, typically expressed in mm/min. It represents the rate of material engagement without causing tool jamming, and is given by:

$$R = S\ x\ f\ x\ N \qquad \text{Eq. 14}$$

where S is the spindle speed, f is the feed per tooth in mm/tooth, and N is the number of flutes on the cutting tool (Ismail & Dhakal, 2018). Note that feed per tooth is a term commonly used in milling, referring to the axial distance the tool advances per cutting tooth per revolution. In the context of drilling, the cutting tooth is known as a flute, and feed per tooth therefore denotes the axial advance of the drill per flute per revolution, expressed in mm/rev/flute — equivalently expressed as the feed per revolution in mm/rev.

Ultimately, thrust force is the primary mechanical driver of delamination in laminated composites, acting by either pushing out or pulling up individual plies during drilling. As the drill bit nears the exit plane of the laminate, the remaining uncut thickness decreases progressively, reducing the material's resistance to the applied load. Once the drilling force exceeds the interlaminar bond strength of the remaining plies, delamination initiates in a Mode I fracture mechanism, as shown in Figure 3.3 (Hocheng & Tsao, 2005). An analogous but reversed mechanism governs peel-up delamination at the drill entry, where the upward component of thrust force lifts and separates the outer plies as the bit engages the material.

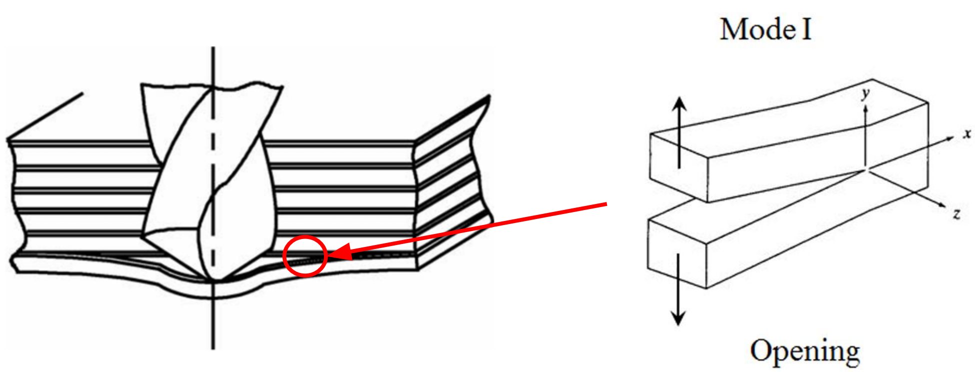


Figure 3.3 Fracture mechanism of a composite delamination (Hocheng and Tsao, 2005).

In its simplest form, thrust force is the normal force applied by the cutting tool on the workpiece and it can be estimated by the following equation:

$$F = \frac{k' \times kc \times f \times D}{2} \quad \text{Eq. 15}$$

where kc is the specific cutting force in N/mm$^2$ which depends on the material being drilled, $f$ is the feed per revolution in mm/rev, D is the tool diameter in mm, and k' is the drilling coefficient which is dependent on the tool tip geometry (Ismail & Dhakal, 2018).

Alternatively, by modeling the thrust force as a concentrated load applied at the chisel edge and assuming isotropic behavior under pure bending, the critical thrust force at the onset of delamination crack propagation can be expressed as:

$$F_A = \pi\sqrt{32G_{IC}M} = \pi\left[\frac{8G_{IC}Eh^3}{3(1-v^2)}\right]^{1/2} \quad \text{Eq. 16}$$

where $F_A$ is the thrust force, h is the uncut depth under the tool, $M = \frac{Eh^3}{12(1-v^2)}$ is the stiffness per unit width of the fiber reinforced material, E is Young's Modulus, v is the Poisson's ratio for the material, and $G_{IC}$ is the mode I interlaminar fracture toughness of the material (Hocheng, 2012). To avoid drilling-induced delamination, the applied thrust force must remain below this critical value, which is governed entirely by the material properties and the remaining uncut thickness at any given point during drilling.

However, composite materials are anisotropic and heterogeneous, and therefore require more complex analytical models to characterize drilling behavior than the isotropic formulations proposed by Hocheng (2012). Specifically, while the isotropic models assume a circular delamination morphology, an anisotropic model was developed by Jain and Yang (1993), which accounts for the three-dimensional material properties of the composite and assumes an elliptical delamination geometry — a morphology that has been experimentally observed in prior studies. The thrust force expression for the anisotropic case is given by:

$$F_A^* = \frac{3\pi}{k}\sqrt{2G_{IC}D^*} \quad \text{Eq. 17}$$

where k = a/b is the ellipticity ratio, a is the half-length of the major axis of the elliptical delamination, b is the half-length of the minor axis, and $D^* = D_{11} + \frac{2}{3}(D_{12} + 2D_{66})k^2 + D_{22}k^4$ with k being the ellipticity ratio. Similarly, all other drilling parameters can be derived considering the anisotropic nature of composites. However, these derivations are outside the scope of this work.

### 3.1.2 Drilling Thermodynamics

The cutting mechanics and progressive tool engagement during drilling produce a characteristic evolution in both thrust force and temperature throughout the operation, as shown by Liu and Huang (2024) in Figure 3.4. As the tool tip initially contacts and penetrates the laminate surface, the contact area between the tool face and the workpiece grows, causing both thrust force and temperature to rise simultaneously. Once the tool tip is fully embedded and the main cutting edge becomes the primary material-removing element, the effective stiffness of the engaged material begins to decrease, reducing the rate of thrust force increase. Despite this, both quantities continue to climb gradually until reaching their respective peak values. This intermediate stage — full tip engagement with no exit breakthrough — corresponds to the drilling scenario for injection repair, where through-penetration is deliberately avoided in order to retain the repair resin. Had drilling been continued to full exit, the stiffness of the remaining material would drop sharply, producing a rapid decline in thrust force and a more gradual reduction in temperature (Liu & Huang, 2024).

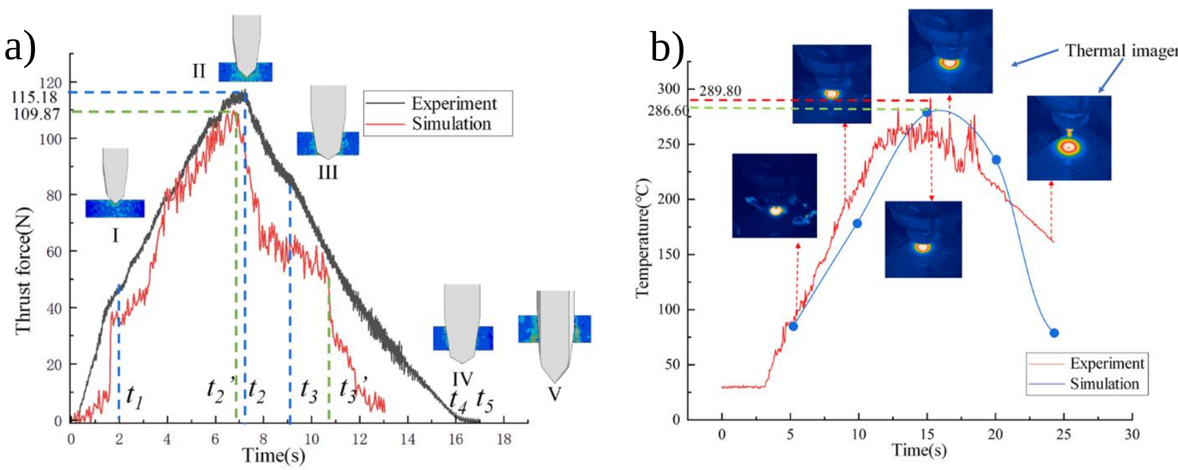


Figure 3.4 Time evolution as drill tool traverses the workpiece of a) thrust force, and b) temperature (Liu & Huang, 2024).

The rise in workpiece and tool temperature throughout the drilling process is primarily driven by the frictional forces between the cutting tool and the composite material, increased by tool wear where present. Temperature reduction begins as the tool exits the workpiece, at which point heat conduction from the hot drilling zone to the surrounding cooler material becomes the dominant thermal mechanism. As drilling advances and the tool penetrates deeper, the diminishing material stiffness reduces frictional heat generation, causing the rate of heat production to fall below the rate at which heat is conducted away — resulting in a net decrease in temperature at the drilling site, as shown in Figure 3.4, b). Once the tool is fully withdrawn, thermal convection between the workpiece surface and the surrounding air provides an additional cooling mechanism that further reduces the residual temperature at the drilled location (Liu & Huang, 2024).

Similarly, temperature during drilling is highly dependent on process parameters — spindle speed, feed rate, and drill bit geometry — which play an important role in minimizing thermal build-up while simultaneously reducing thrust force. With respect to temperature specifically, low feed rates and low spindle speeds have been shown to produce the lowest temperature rise during drilling (Liu & Huang, 2024).

## 3.2 Drilling Optimization

### 3.2.1 Parameter Optimization

Key concerns when drilling composites include drilling-induced delamination, debris generation leading to additional contamination, and depth control. Drilling parameters — such as bit diameter, spindle speed, helix angle, and feed rate — have been extensively studied to understand their effects on hole quality in anisotropic composite materials. As demonstrated in Section 3.1.1, some of these parameters are interdependent, and some are proportional to one another, such as feed rate and spindle speed. Moreover, as shown in Section 3.1.2, thrust force —

which is directly related to the magnitude of drilling-induced damage — evolves throughout the drilling operation owing to the drilling tool having different cutting mechanisms as it traverses the workpiece. Together, these concepts inform the selection of optimal drilling parameters to minimize drilling-induced damage in composite materials.

Thrust force is the driving factor in drilling-induced composite delamination both at entry and exit. Therefore, the most effective way to mitigate such failure mechanism is to meticulously select drilling parameter values that lead to the minimization of thrust force. As captured in Equation 15, thrust force is directly proportional to drill bit diameter and feed per revolution. And, because feed rate is directly proportional to feed per revolution, as seen in Equation 14, but inversely proportional to spindle speed, as shown in Equation 3, thrust force is also inversely proportional to spindle speed. Based on these mathematical relationships, it can be concluded that minimizing the drill bit diameter and feed per revolution, while maximizing spindle speed will lead to the lowest thrust force and, therefore, to the lowest drilling-induced delaminations.

Latha et al. (2011) analyzed the influence of drill geometry on the drilling of glass fiber reinforced polymer (GFRP) composites by comparing thrust forces produced by different drill bit geometries using experimental data. Figure 3.5 shows the values of thrust force versus various drilling parameters using a brad point drill — a geometry commonly used in machining of composites, illustrating how spindle speed, feed rate, and drill diameter simultaneously affect thrust force intensity. As seen in the plots, feed rate is the most influential parameter on thrust force, followed by drill diameter, while spindle speed shows a weak relationship to producing thrust force. Thus, in most cases, for a selected drill diameter, one should use the lowest feed rate possible to reduce thrust force.

Srinivasan et al. (2017) conducted a similar study on glass fiber reinforced polypropylene (GFR-PP) composites where they examined the effects of drilling parameters on delamination using the Box-Behnken design — an experimental response surface methodology used to optimize the delamination factor across multiple process variables known to influence drilling-induced delamination, namely drill diameter, feed rate, and spindle speed. As shown in Figure 3.6, and in agreement with the results of Latha et al. (2011), the analysis confirms that feed rate is the most influential parameter on the delamination factor, and drill diameter. Spindle speed shows a non-monotonic relationship to the delamination factor as shown in Figures 3.6, (b) and 3.6, (c).

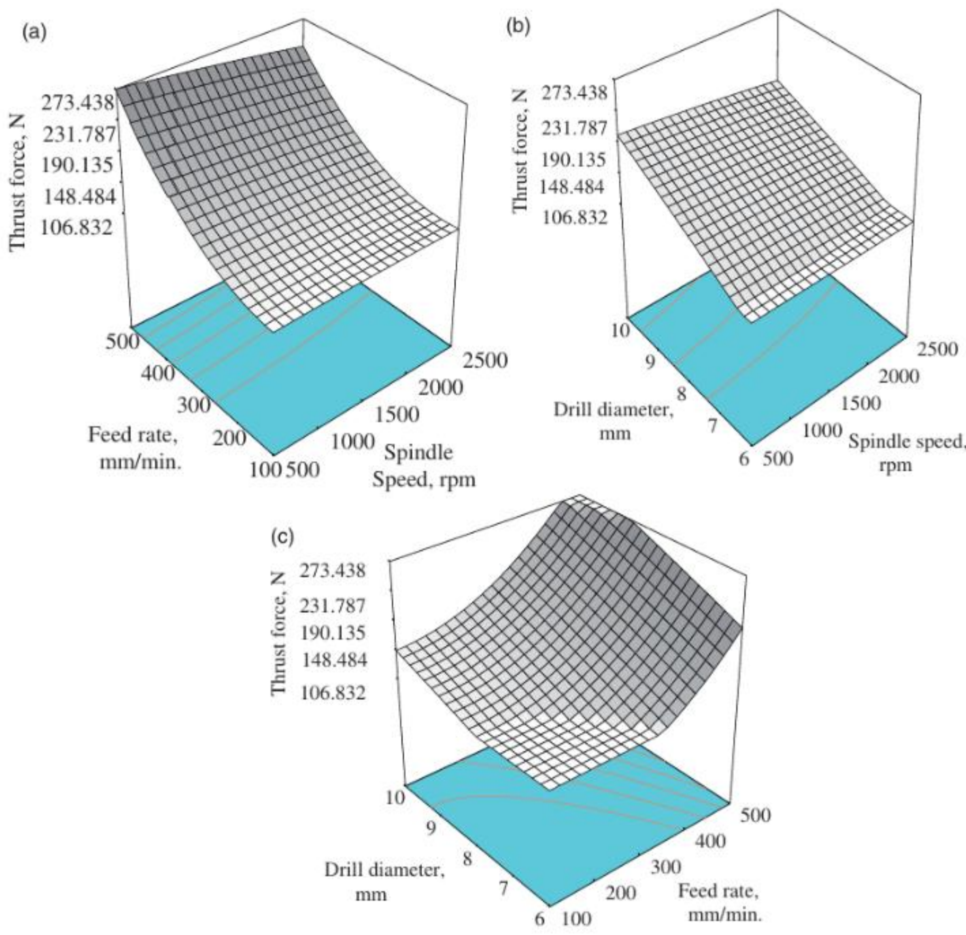


Figure 3.5 3D response graph for thrust force in drilling by Brad dill: a) spindle speed x feed rate; b) spindle speed x drill diameter; c) feed rate x drill diameter (Latha et al., 2011).

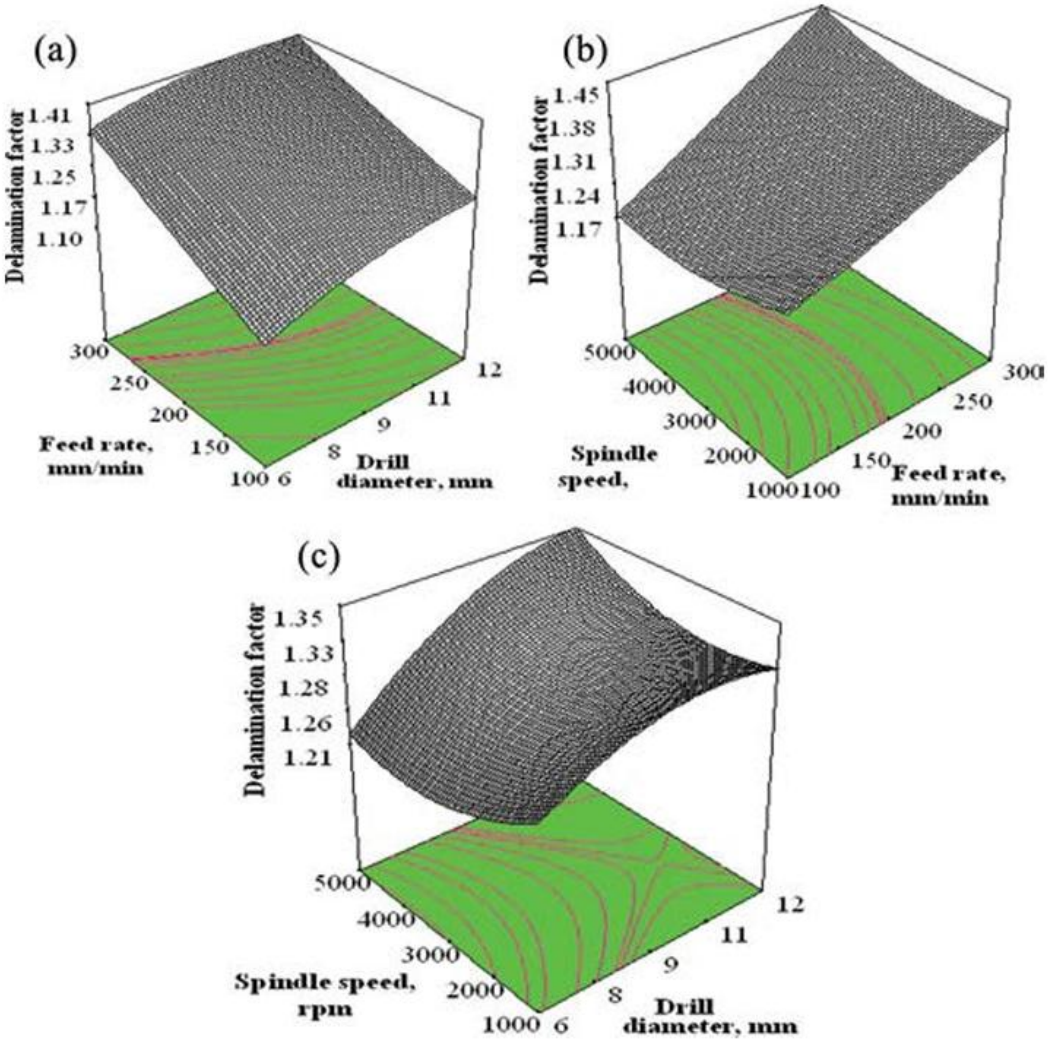


Figure 3.6 3D response graph for delamination factor in drilling by Brad dill: a) drill diameter x feed rate; b) feed rate x spindle speed; c) feed rate x spindle speed (Srinivasan et al., 2017).

It is worth mentioning that, although high spindle speeds are recommended to reduce drilling-induced defects, this trend does not hold at extreme spindle speeds — beyond the conventionally used range of 2,000–5,000 rpm — where thrust force and torque instead increase significantly. This occurs because the dominant material removal mechanism shifts from cutting to ploughing and abrasion as cutting speed increases, driven by the accelerated development of tool wear (Lin & Chen, 1996).

In summary, small drill bit diameters (< 0.118 in.), high spindle speeds (> 2,000 rpm), low helix angles (< 30°), and low feed rates (< 0.02 in./peck) have been shown to reduce the maximum thrust force during the drilling of composites. For the experiments conducted in this work, a spindle speed of 2,500 rpm was selected, as it represents the maximum achievable speed of the equipment used but it also happens to be a sweet spot in the spindle speed range. Moreover, a feed rate of 0.01 in./peck was chosen, falling below the lower bound reported in the literature, given that feed rate has been identified as the most influential parameter governing thrust force. In contrast, low spindle speeds are recommended to reduce thermal build-up during drilling; however, the speeds used in this work are not sufficient to produce significant temperature rises (Liu & Huang, 2024).

### 3.2.2 Setup Optimization - Vacuum Jig for Debris Mitigation

In addition to optimizing drilling tools and parameters to minimize drilling-induced damage, mitigating dust accumulation during drilling is critical. Microscopic composite particles generated during machining can the clog hole-to-delamination regions or adhere to the interior surface of the drilled hole, as shown in Figure 3.7. Minimizing dust contamination into the delaminations is therefore essential for injection repair, as clean pathways are required to ensure complete and effective resin infiltration.

To reduce dust accumulation during drilling, a custom 3D-printed vacuum jig was fabricated. The design was guided by Bernoulli’s equation, which states that for an incompressible fluid flowing along a streamline, fluid velocity is inversely proportional to pressure and, by continuity, to cross-sectional flow area (Hall, 2021). For a system in which height changes are negligible, Bernoulli’s equation simplifies to:

$$P + \frac{\rho v^2}{2} = constant \quad \text{Eq. 18}$$

where P is the absolute pressure, $\rho$ is the fluid density, and v is the velocity of the fluid.

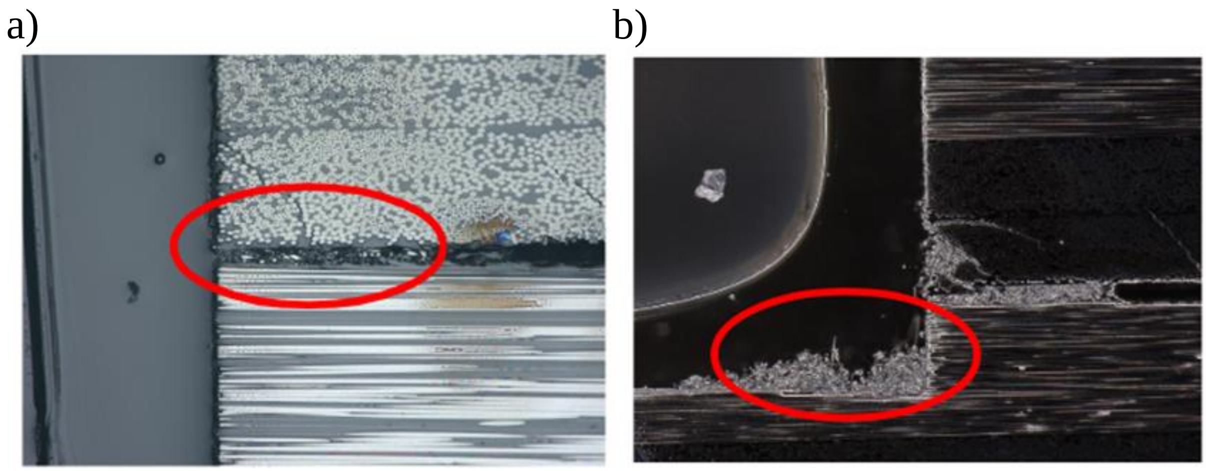


Figure 3.7 Debris contamination after drilling: a) Delamination blockage, b) debris buildup at bottom of the hole.

The vacuum jig, shown in Figure 3.8, forms a complete seal with the specimen during drilling, thereby creating a closed airflow channel. This configuration promotes higher airflow velocity at the drilling interface and lower velocity near the dry vacuum outlet, generating a pressure differential that pulls debris out of the hole while it directs debris into the vacuum hose.

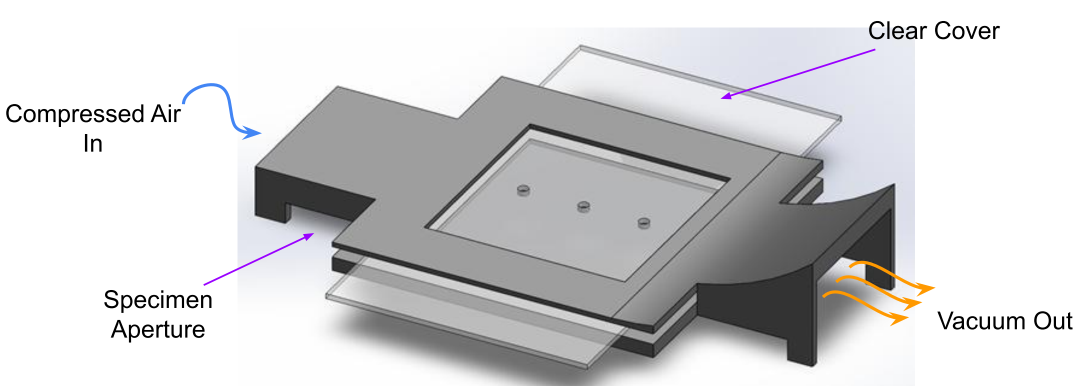


Figure 3.8 CAD model of dust-extraction vacuum jig.

More specifically, debris extraction is achieved by a suction mechanism that is created from the change in pressure and velocities as the airflow from the compressed air gun sweeps across the surface of the composite during drilling and enters the dry vacuum on the other end, as seen in Figure 3.9 and Figure 3.10.


Figure 3.9 Vacuum jig setup.

This mechanism is crucial during drilling because it prevents debris from clogging pre-existing delaminations by maintaining continuous extraction throughout the drilling process — an effect that is otherwise difficult to achieve by holding a vacuum nozzle tangent to the hole opening. As shown in Figure 3.10, the airflow travels from one end of the workpiece to the other, undergoing a significant velocity change upon passing over and entering the drilled hole. As the airflow approaches the hole inlet, it transitions from laminar to turbulent, producing a sharp increase in airflow velocity that enhances the shear forces acting on debris particles adhered to the hole surface (MacManus & Eaton, 1996). Two complementary mechanisms then drive the expulsion of loosened debris from the hole. First, consistent with Bernoulli's principle, the reduction in cross-sectional area inside the hole produces a local low-pressure zone at the inlet, which draws air and detached particles outward and through the hole. Second, the vacuum system maintains a lower pressure at the outlet ($P_{outer}$) relative to the interior ($P_{inner}$), sustaining a net pressure gradient that continuously drives airflow — and entrained debris — toward the exit of the enclosed system (Shahzad et al., 2022).

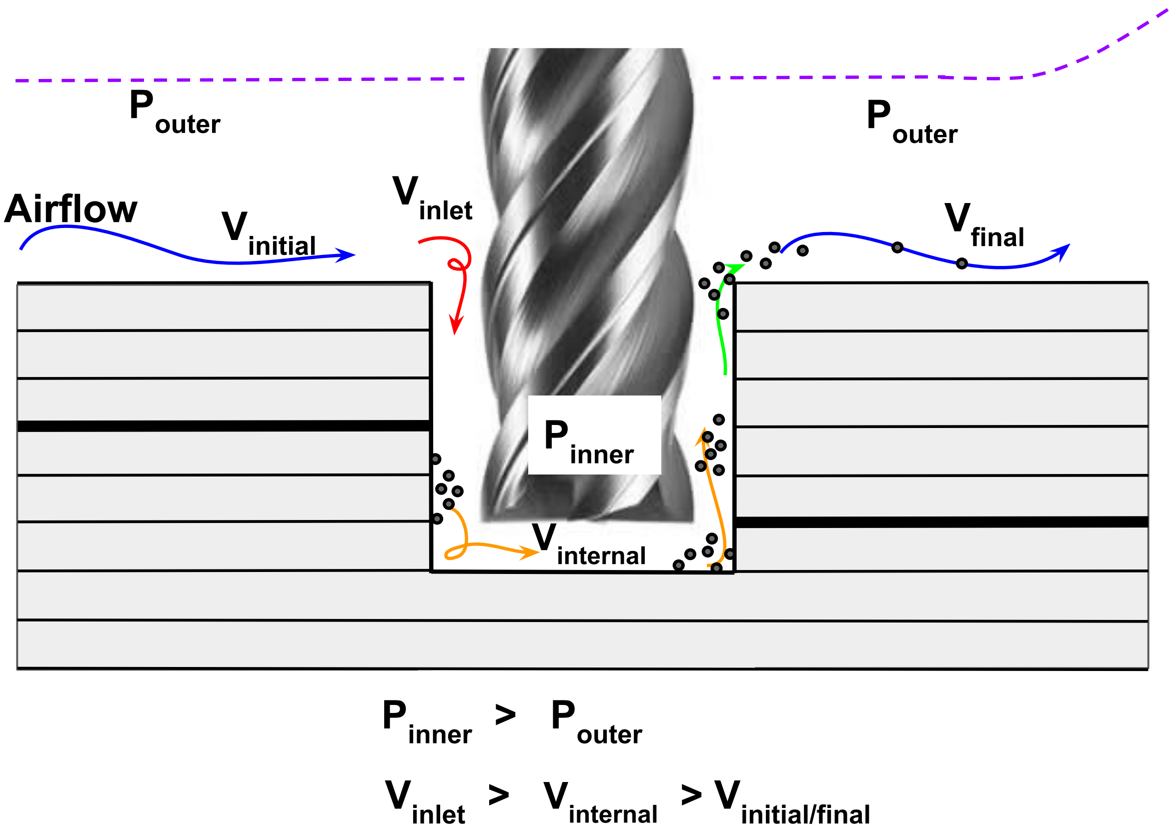


Figure 3.10 Debris suction mechanism diagram.

## 3.3 Experimental Setup

### 3.3.1 Drilling Experiments Setup

The drilling experiments conducted for this study were performed on a HiTorque 3990 Mini Mill, which features a maximum spindle speed of 2500 rpm and is equipped with a DRO Pro 3M three-axis digital readout. The digital readout provides precise readings of the movement of the mill's table and head locations. To manage debris, a 6-gallon dry vacuum with a composite filter was used during drilling which was attached to the vacuum jig, as seen in Figure 3.9.

Moreover, compressed air is constantly being blown from the left side of the jig to further increase flow speed and drive composite debris out of the drilled holes.

### 3.3.2 Experimental Procedure

The experiments conducted in this research required the use of tailored and optimized drilling tools and parameters to produce drilled holes that 1) reach as many delaminations as possible, and 2) mitigate drilling-induced damage (i.e., does not create additional delamination). To select the drilling tools that produce the desired hole geometry and surface finish, a series of experiments was conducted using four off-the-shelf drill bits, as shown in Table 3.1. The tests involved drilling artificially delaminated CFRP composite coupons using various tool combinations under selectively defined drilling parameters that minimize drilling-induced delamination and obtain the desired hole morphology. Key factors influencing drilling performance include drill bit diameter, helix angle, pecking rate, and spindle speed. Specifically, small drill bit diameters (< 0.118 in), high spindle speeds (> 2,000 rpm), low helix angles (< 30°), and low pecking rates (< 0.02 in/peck) have been shown to reduce drilling-induced damage in CFRP composites as covered in Section 3.2.1. Table 3.2 summarizes the tool combinations, machining settings, and experimental setup conditions.

Table 3.1 Drilling tools part numbers and dimensions.

| Tool | Diameter [in] | Length [in] | Helix Angle | Image |
|---|---|---|---|---|
| Short-Taper Drill Reamer<br>Mfr: Amamco Tool<br>Part #: B101-10943 | 0.0980 | 3 | 10° |  |
| Brad Point Drill Bit<br>Vendor: McMaster-Carr<br>Part #: 61264RT | 0.0979 | 2 | Unknown (<40°) |  |
| End Mill<br>Mfr: SGS<br>Part #: 30113 | 0.1094 | 1.5 | 30° |  |
| Twist Drill<br>Vendor: McMaster-Carr<br>Part #: 2956A13 | 0.0938 | 2 | 30° |  |

Table 3.2 Composite coupon drilling test matrix.

| Drilling Tool Combinations | Number of samples | Drill/Ream speeds | Pecking rate | Vacuum Parameters | Drilling Execution |
|---|---|---|---|---|---|
| Amamco short taper helical + end mill | 3 | Drill: 2500 RPM, Ream: 250 RPM | 0.01 in/peck | During drilling operation (using 3-D printed jig) | HiTorque 3990 Mini Mill<br><br>Drilling tool mounted on a Jacob's Chuck |
| Amamco short taper helical + brad point | 3 | | | | |
| Brad point | 3 | | | | |
| Twist drill | 3 | | | | |
| Twist drill + 2.5 mm brad point | 3 | | | | |
| Twist drill + end mill | 3 | | | | |

Additionally, because injection repairs are typically performed from the outer surface of an aircraft without interior access, all holes were required to maintain a buffer of two plies with a +1/-0 ply tolerance to account for human error. For example, for a composite with a nominal ply thickness of 0.005 in, this is equivalent to a maximum distance of 0.015 inches from the back surface. Figure 3.11 shows an example of a hole that barely meets the tolerance criteria. Although still acceptable, in this case, any delaminations in the last 2 plies will, most likely, not be reached by the repair resin.

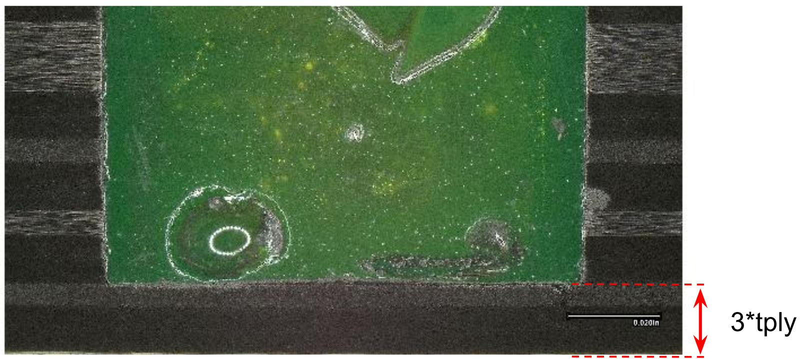


Figure 3.11 Example of 3-ply distance from bottom of laminate.

The drilling procedure begins with cleaning and wiping down the repair area to ensure the surface is free of contaminants prior to hole location layout. Injection hole locations are then marked directly on the composite surface using a permanent fine-tip marker. The placement of the holes must be determined prior to drilling, which can be completely arbitrary (e.g., often a grid pattern is used) or based on the results from the ultrasonic testing. Once the layout is complete, the number of holes and the total internal damage area (previously mapped by NDI) are recorded prior to drilling.

The mini mill is then prepared for drilling. The Amamco TDR is installed, and the hole depth is set to the total laminate thickness minus two ply thicknesses plus an additional tolerance, as follows:

$$Depth \; = \; Total\; laminate\; thickness \; - \left( \, 2 * \; t_{ply} \; + 0.5 * t_{ply} / {-0} \right) \qquad \text{Eq. 19}$$

In general, the bottom buffer can be estimated as total remaining thickness of 0.010 inches. This is achieved by driving the drill tip down to just contact a reference aluminum shim-stock sheet of 0.10-in nominal thickness, after which the Z-axis digital readout is zeroed to establish the final depth as seen in Figure 3.12. It is important to note that the depth setting must be repeated each time the drill bit is changed, as the geometry varies between tools. Spindle speed is set to a minimum of 2,500 rpm with a pecking rate of 0.01 in./peck controlled by hand-turning the fine-depth z-axis knob on this particular mini mill system. A steady drilling motion is critical throughout the process to prevent excessive vibration.

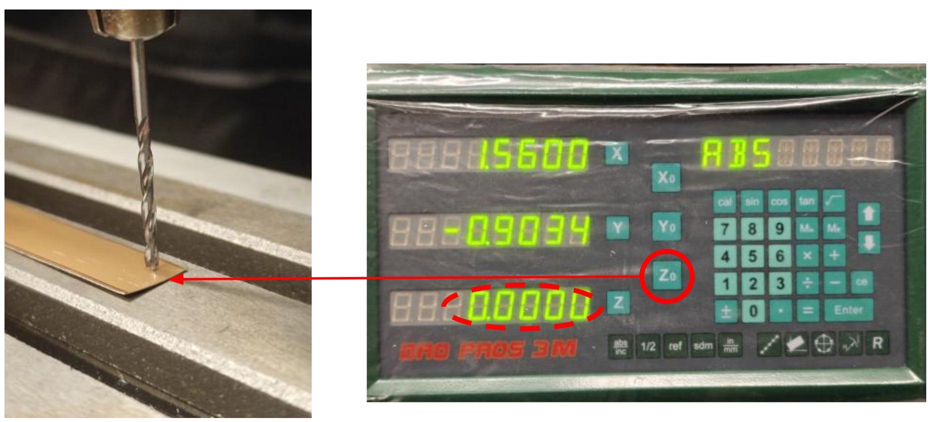


Figure 3.12 Zeroing of the z-axis after adjusting height following touching down on shim-stock.

Prior to drilling all remaining holes, a single pilot hole is drilled in the delaminated area and inspected to verify that it did not penetrate the far side of the laminate. Once confirmed, all remaining holes are drilled following the traced layout in two stages: first, all holes are drilled using the TDR; then, each hole is chased with the end mill to refine the hole geometry. The vacuum fixture and airflow defined in Section 3.2.2 are applied during all drilling operations. Following drilling and vacuum fixture removal, the repair area and its surroundings are vacuumed to remove loose debris. Finally, the number of drill bit uses is recorded with one hole counting as one use, and each bit is discarded after 30 uses to prevent performance degradation from heat build-up and surface abrasion caused by tool wear.

### 3.3.3 Specimen Information

This study involved drilling holes in 24-ply, end-notched flexure composite specimens made of unidirectional IM7/977-3 carbon/epoxy composite tape. The layup schedule for these specimens consists of only 0° plies parallel to the longest side of the specimen. Each specimen contains a lab-controlled delamination through the midplane, crated by a 0.076 mm-thick polytetrafluoroethylene (PTFE) release film insert, as illustrated in Figure 3.13.

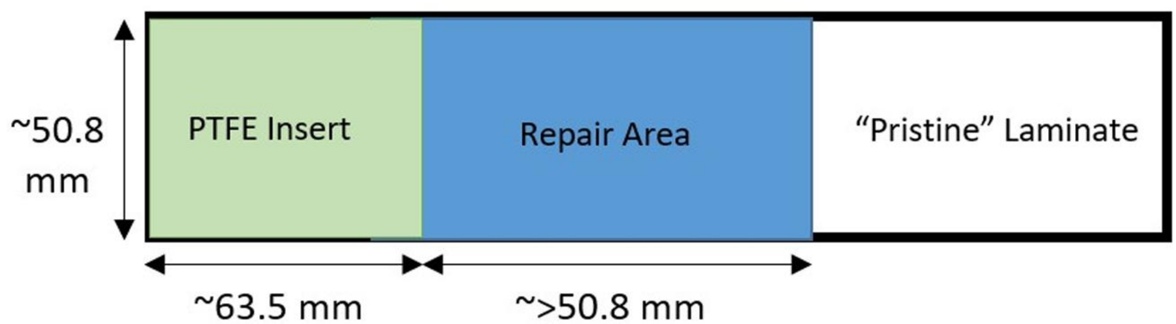


Figure 3.13 End-Notched, flexure-fractured CFRP composite with lab-controlled delamination at midplane (Hiruni, 2025).

In an effort to understand the drilling response of composites with different layup configurations besides all-unidirectional, 25-ply IM7/977-3 autoclave-cured carbon fiber/epoxy composite laminates were also drilled following the same drilling parameters and procedures. Further details on the ply layup schedules and naming conventions of these specimens are provided in Chapter 2, Section 2.3.3.

## 3.4 Results

A total of six drill bit combinations were investigated, with three specimens tested for each combination. The primary objective of this study was to identify the drill bit combination that produces the most favorable hole geometry for injection repair. Additionally, this work aimed to assess whether the drilling tools introduced any drilling-induced defects in the CFRP composites. It should be noted that the spindle speed used in this study is lower than values typically recommended in the literature, due to the drilling machine's maximum spindle speed of 2,500 rpm, as explained in Section 2.2.1. Testing of the six drill bit combinations on all-unidirectional laminates produced six distinct surface hole profiles, whose cross-sectional profiles are presented in Table 3.3.

Table 3.3 Hole cross-section views.

| Drilling Tool Combination | Hole # | Distance from Bottom [in] | Image |
|---|---|---|---|
| Amamco short taper helical + end mill | 3 | 0.0322 | 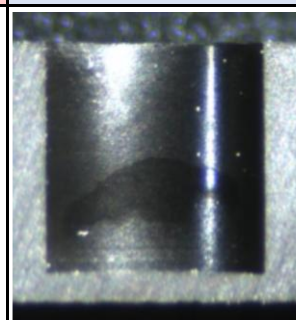 |
| Amamco short taper helical + brad point | 3 | 0.0256 |  |

Table 3.3 Hole cross-section views, Continued.

| Drilling Tool Combination | Hole # | Distance from Bottom [in] | Image |
|---|---|---|---|
| Brad point only | 3 | 0.0158 |  |
| Twist drill only | 3 | 0.0197 |  |
| Twist drill + 2.5 mm brad point | 3 | 0.0166 | 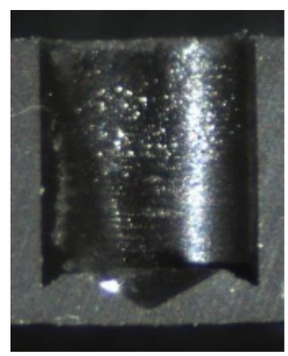 |
| Twist drill + end mill | 3 | 0.0182 | 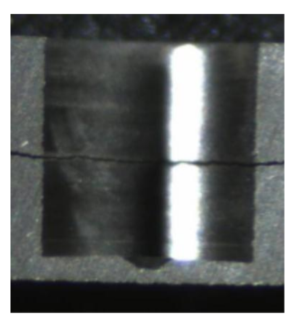 |

The micrographs obtained from the experiments show that the Amamco TDR and the end mill produced the least fraying on the hole wall and the fewest jagged edges. In contrast, the micrographs reveal that the brad point drill caused observable drilling-induced damage, including fraying, scratches, and chipping. Figure 3.14 shows that all three specimens drilled with the brad point tool produced holes with rough surfaces and chipped edges, making them non-ideal for injection repair for two reasons: first, coarse surfaces may contain micro-scale surface irregularities that impede resin penetration, leading to high stress concentrations under loading because of material discontinuity; and second, chipping produces large debris that can be hard to remove during drilling and can lead to cloggage of hole-to-delamination regions.

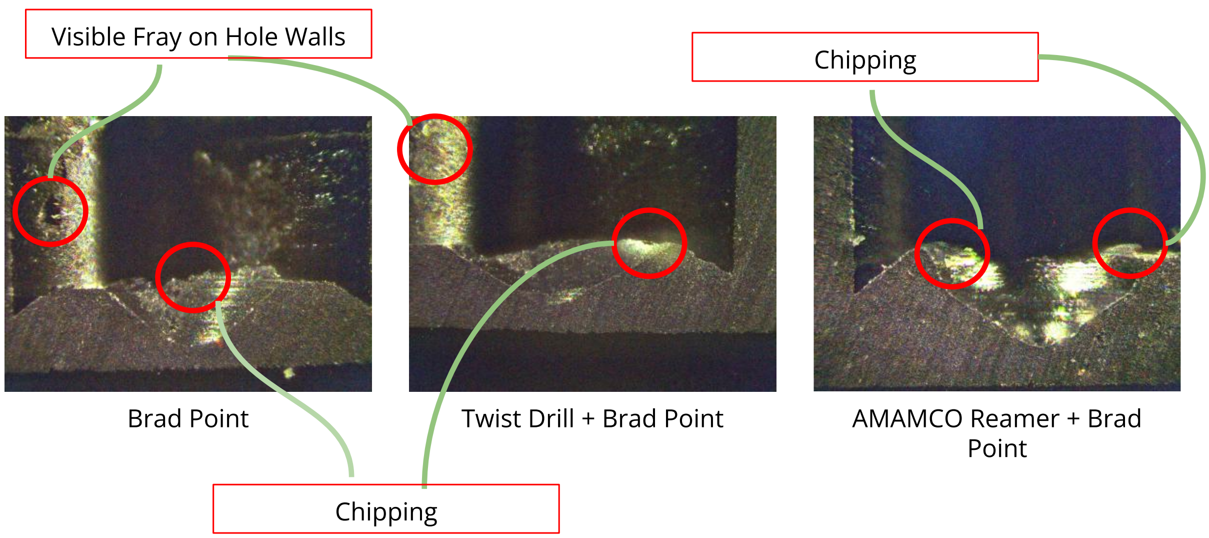


Figure 3.14 Brad point: Holes detail views.

Additionally, the micrographs indicated that the coupons drilled with the twist drill experienced complete fracture, as shown in Figure 3.15. Although this is a pre-existing, lab-controlled delamination, the twist drill was the only cutting tool that led to the complete rupture of the drilled specimen during drilling operation, suggesting that this tool type generated the highest thrust forces, which is consistent with findings reported in the literature. The twist drill exhibited similar results to those observed in the holes produced by the brad point tool, which ultimately ruled both tools out as suitable options.

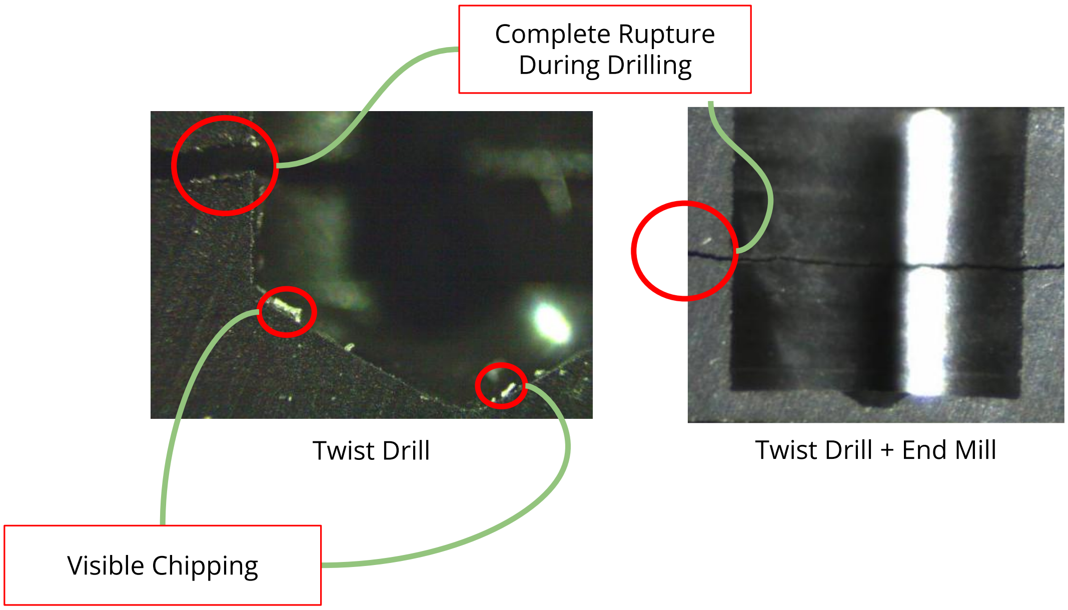


Figure 3.15 Twist drill: hole detail view.

### 3.4.1 Hole Geometry

Regarding hole geometry, the objective was to create a hole that intersected as many delaminations as possible, enabling the injected resin to infiltrate the most delaminations and fully fill the repair volume. Holes exhibiting numerous sharp corners, such as those produced by the twist drill and brad point drill shown in Figure 3.16, are not ideal because some delaminations may become inaccessible as the hole geometry tapers toward the tip.

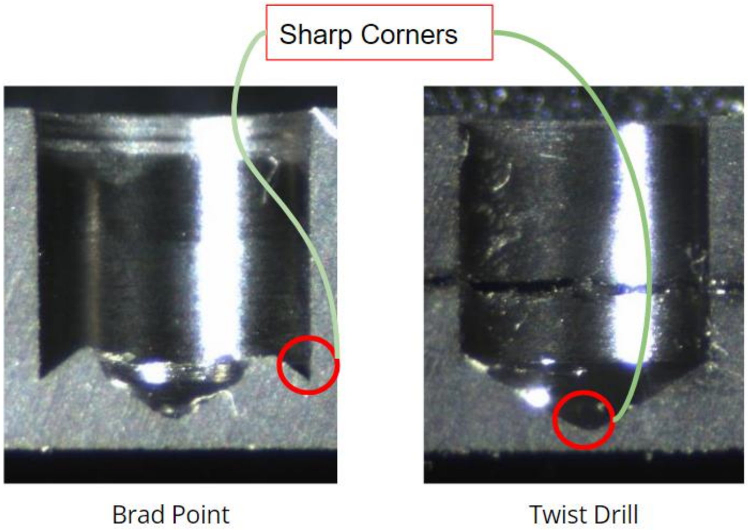


Figure 3.16 Brad point and twist drill: Hole detail views.

In contrast, the end mill produced holes with the least fraying on the hole wall and the fewest jagged edges of all the drilling tools evaluated. Additionally, as seen in Figure 3.18, tool combinations incorporating the end mill produced the flattest bottom surface, making this geometry ideal for accessing the deepest delaminated plies. It should be noted that the cross-sectional profile of the twist drill and end mill combination shows a large delamination at the midplane, which corresponds to the pre-existing, lab-induced delamination present in all ENF coupons.

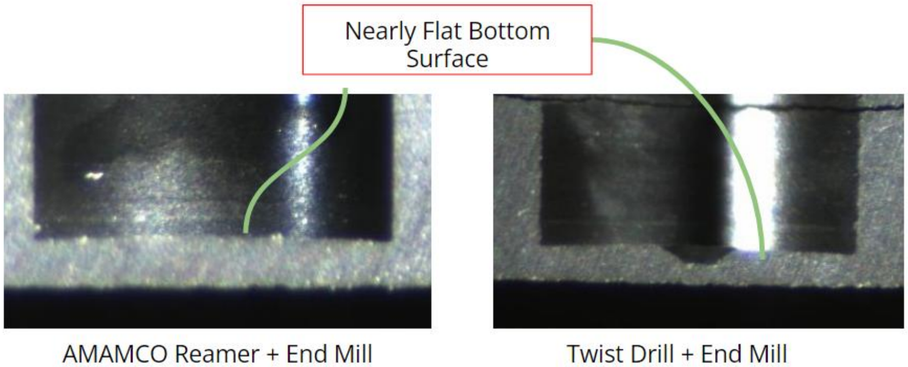


Figure 3.17 End mill: hole detail views.

### 3.4.2 Drilling-Induced Damage Mitigation

Additional experiments were conducted to further refine the drilling parameters for optimal hole surface finish. Through these experiments, it was found that reducing the cutting speed to excessively low values can damage the hole surface, attributed to elevated heat generation and excessive tool vibration. For instance, Figure 3.18 shows signs of tool chatter in the form of diagonal marks on the surface of the holes, which is a direct consequence of the self-excited vibration between the drill bit and the workpiece caused by the slow cutting speed.

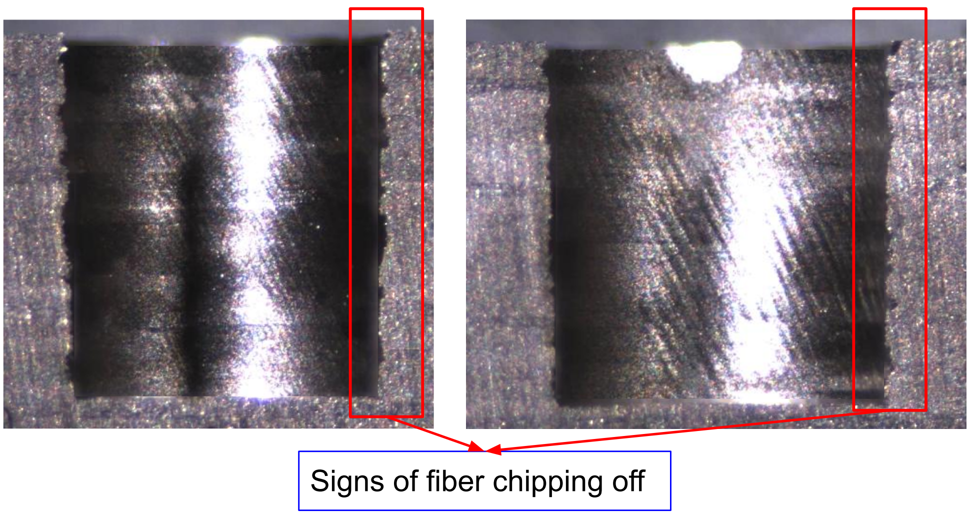


Figure 3.18 Example of fiber chipping on a drilled hole.

A notable difference in surface finish was also observed between specimens with different layup schedules. The IM7/977-3 laminates with a mix of 0, +/-45, and 90 degree plies exhibited greater surface chipping, whereas end-notched flexure specimens, which only had 0-degree plies, laminates displayed less chipping but more pronounced ply collapse at the hole surface, as shown in Figure 3.19. This difference in machinability is likely attributable to the distinct fiber-matrix interaction characteristics of each material system, suggesting that drilling parameters optimized for one material system may not be directly transferable to another.

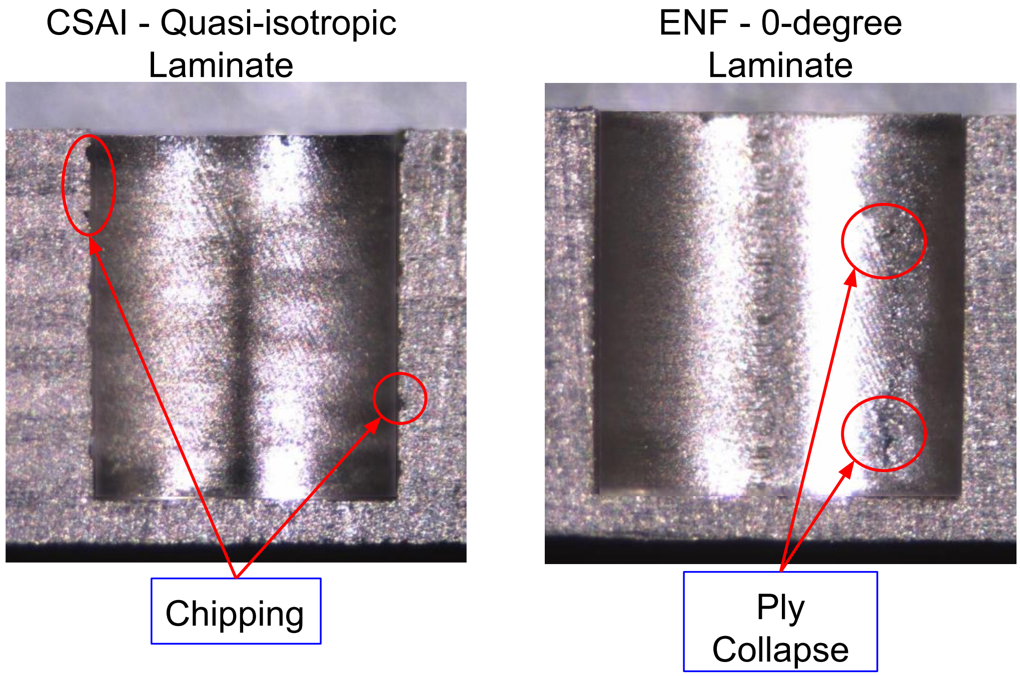


Figure 3.19 Laminate comparison: Hole finish observations.

Moreover, reducing the feed rate when cutting the samples for microscopy with a precision saw was found to mitigate edge chipping at the hole boundary. Therefore, by applying the optimized parameters from Section 3.2.1, specifying a cutting speed of at least 0.33 peck/s, depending on feed rate, and reducing the feed rate on the precision saw, the optimal hole geometry and surface finish were observed, where a rectangular geometry, a 2 to 3 ply buffer, and no signs of surface abrasion, fiber chipping, delamination, or any other type of drilling-induced damage. Figures 3.20 to 3.23 show four distinct cross-section micrographs of well-made holes, which were machined using the same tools and drilling parameters. These micrographs help demonstrate the effectiveness of the drilling methods developed in this work, proving that it is possible to prevent drilling-induced damage in a repeated and reliable manner.

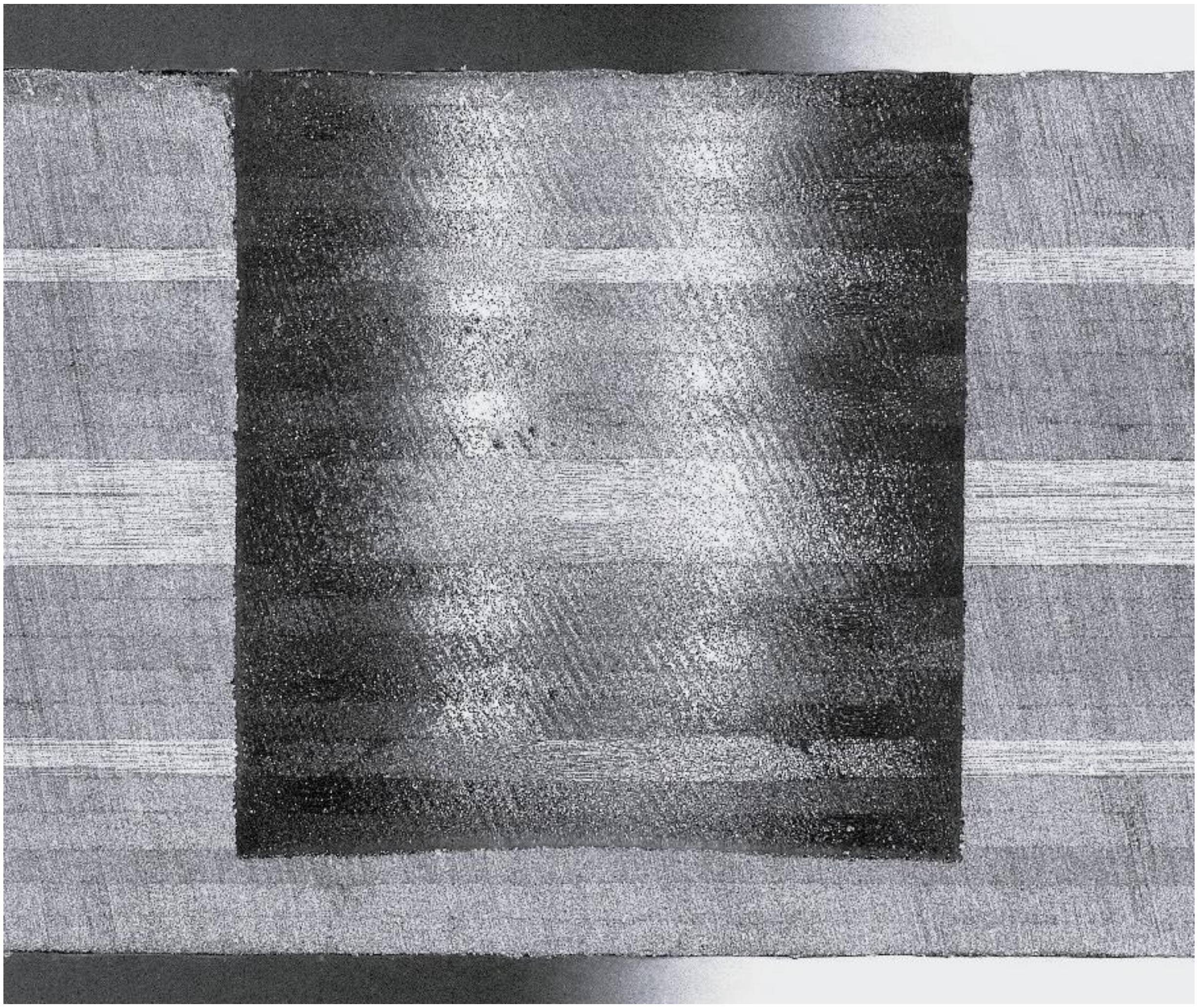

Figure 3.20 Drilled hole #1 on specimen CSAI - RPR - S - 20J – 1. Drilling parameters: Pecking rate: 0.01 in/peck, spindle speed: 2500 rpm, cutting speed: 0.33 peck/s. Tools used: Amamco TDR chased by an End Mill.

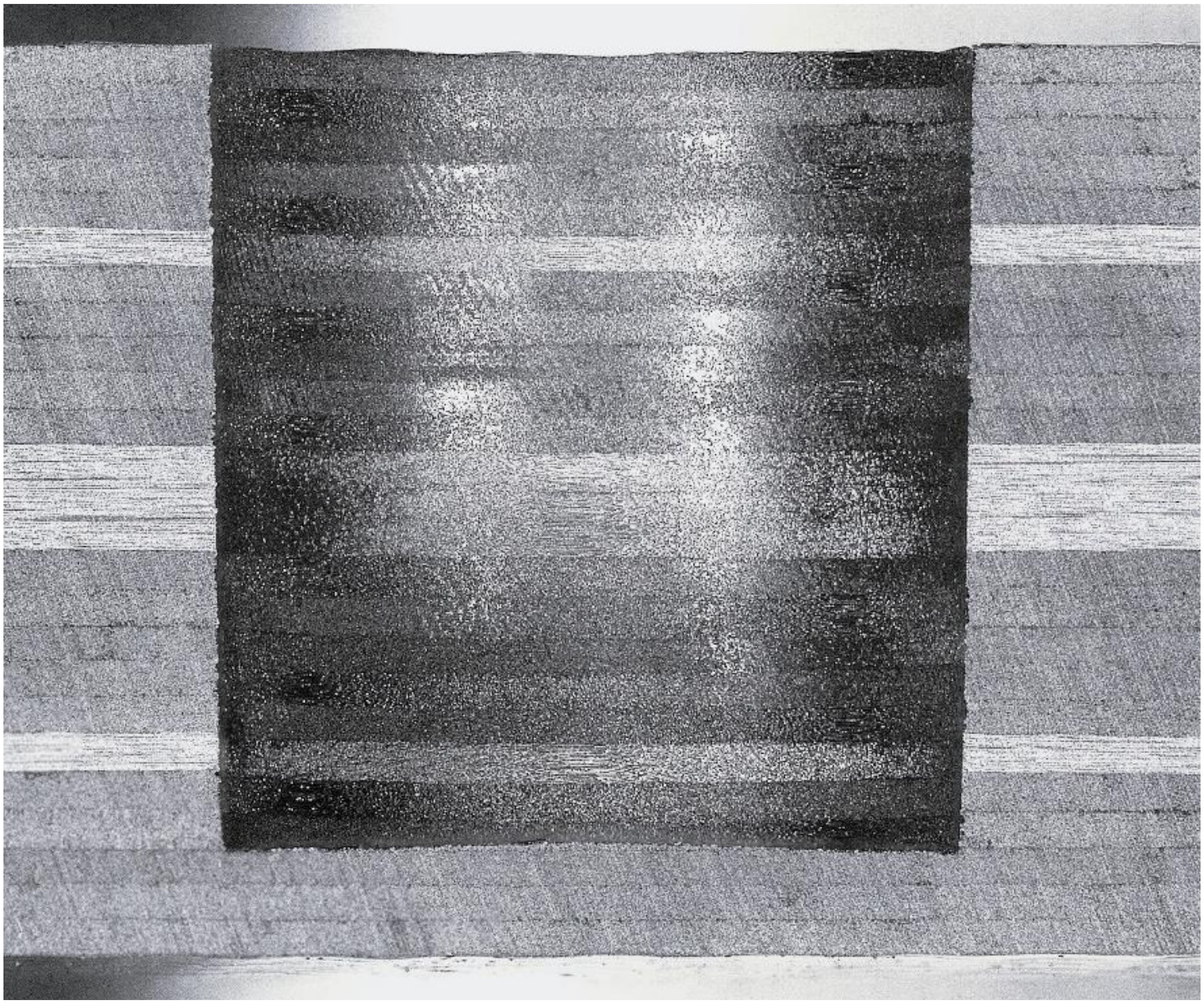

Figure 3.21 Drilled hole #2 on specimen CSAI - RPR - S - 20J – 1. Drilling parameters: Pecking rate: 0.01 in/peck, spindle speed: 2500 rpm, cutting speed: 0.33 peck/s. Tools used: Amamco TDR chased by an End Mill.

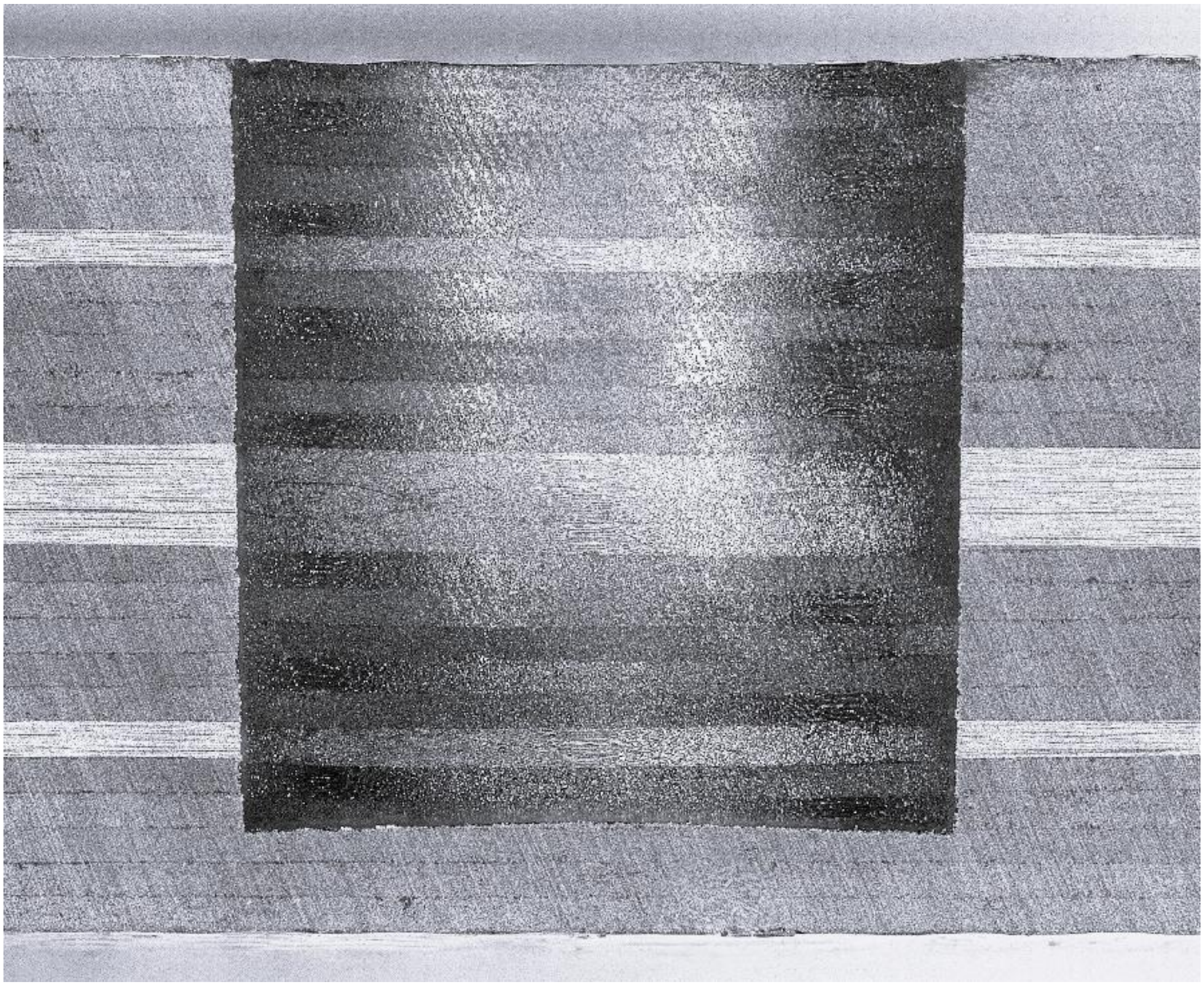

Figure 3.22 Drilled hole #3 on specimen CSAI - RPR - S - 20J – 1. Drilling parameters: Pecking rate: 0.01 in/peck, spindle speed: 2500 rpm, cutting speed: 0.33 peck/s. Tools used: Amamco TDR chased by an End Mill.

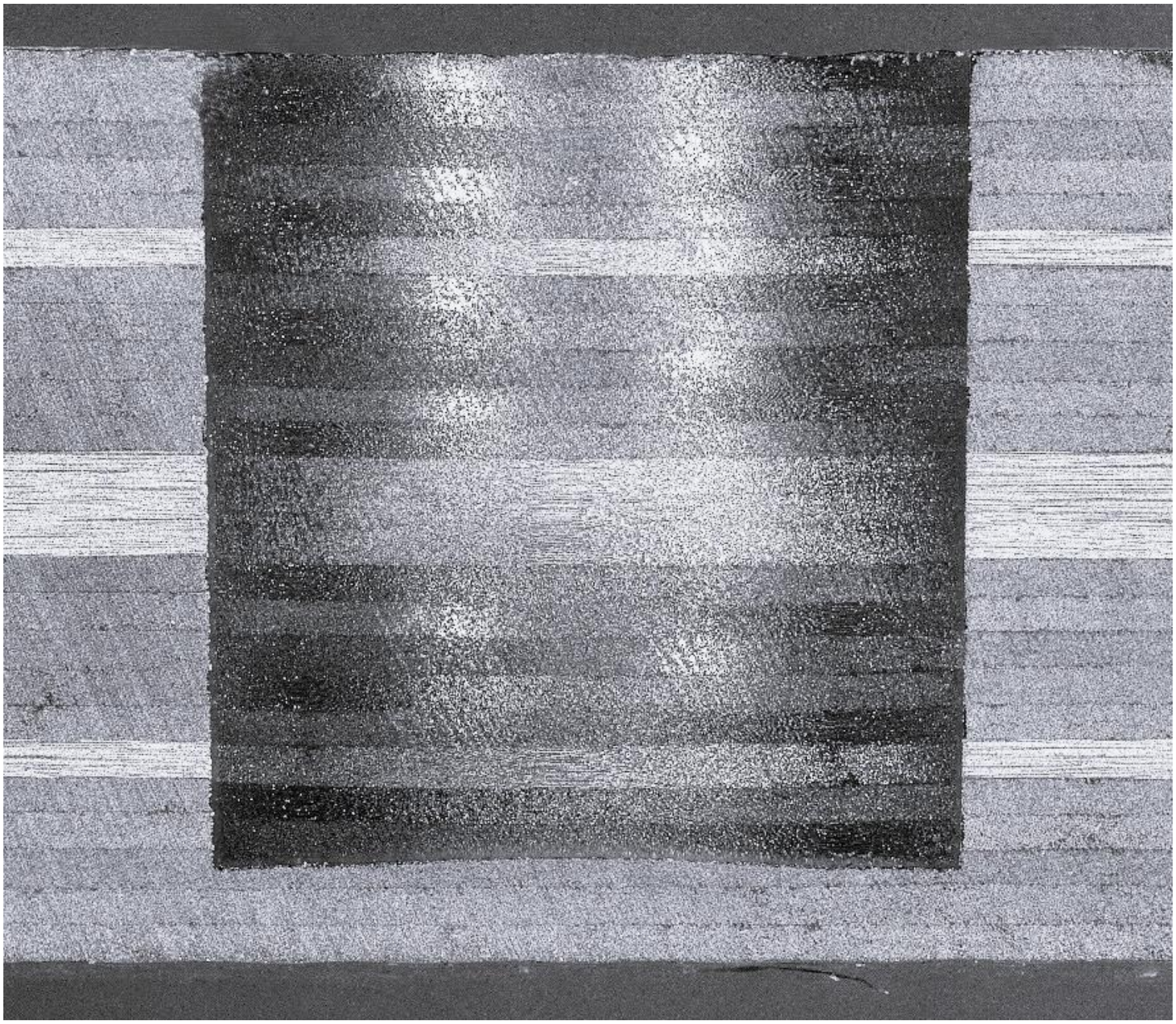

Figure 3.23 Drilled hole #4 on specimen CSAI - RPR - S - 20J – 1. Drilling parameters: Pecking rate: 0.01 in/peck, spindle speed: 2500 rpm, cutting speed: 0.33 peck/s. Tools used: Amamco TDR chased by an End Mill.

### 3.4.3 Debris-Free Drilled Holes

An additional batch of drilled specimens was produced in which half were drilled without the vacuum jig attachment described in Section 3.2.2 and the other half were drilled using the vacuum jig. For the holes drilled without the jig, a dry vacuum nozzle was held adjacent to the drill to remove as much composite debris as possible during drilling as it is conventionally done. Furthermore, a casting epoxy resin was carefully inserted into the holes immediately after drilling to capture the remaining contaminants so that they would not be removed when sectioning and polishing for microscopy. Figures 3.24 and 3.25 show the cross-section micrograph of the holes that were drilled without the vacuum jig, and Figures 3.26 and 3.27 show the holes drilled with the vacuum jig. Note none of the holes show drilling-induced damage. In each of these photos, the drilled hole is filled with clear resin, and the debris is suspended in the resin.

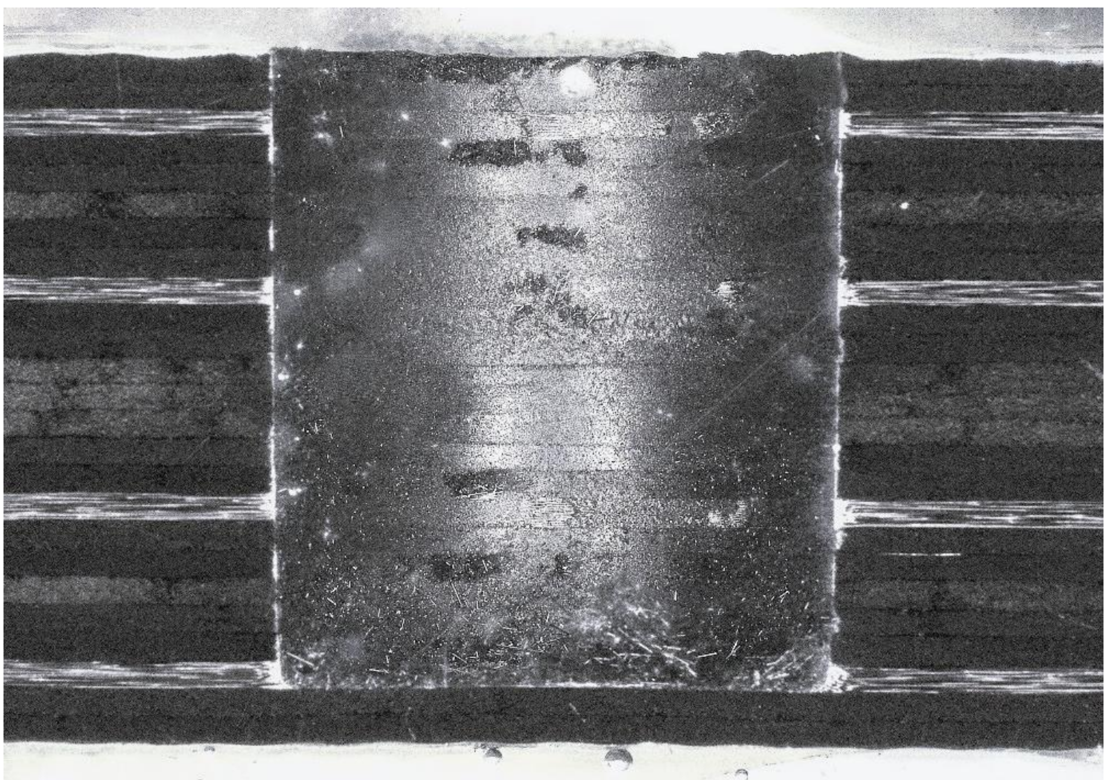

Figure 3.24 Hole NV-01: Drilled hole **without** vacuum jig of specimen CSAI - RPR - S - 20J – 1. Tools used: Amamco TDR chased by an End Mill.

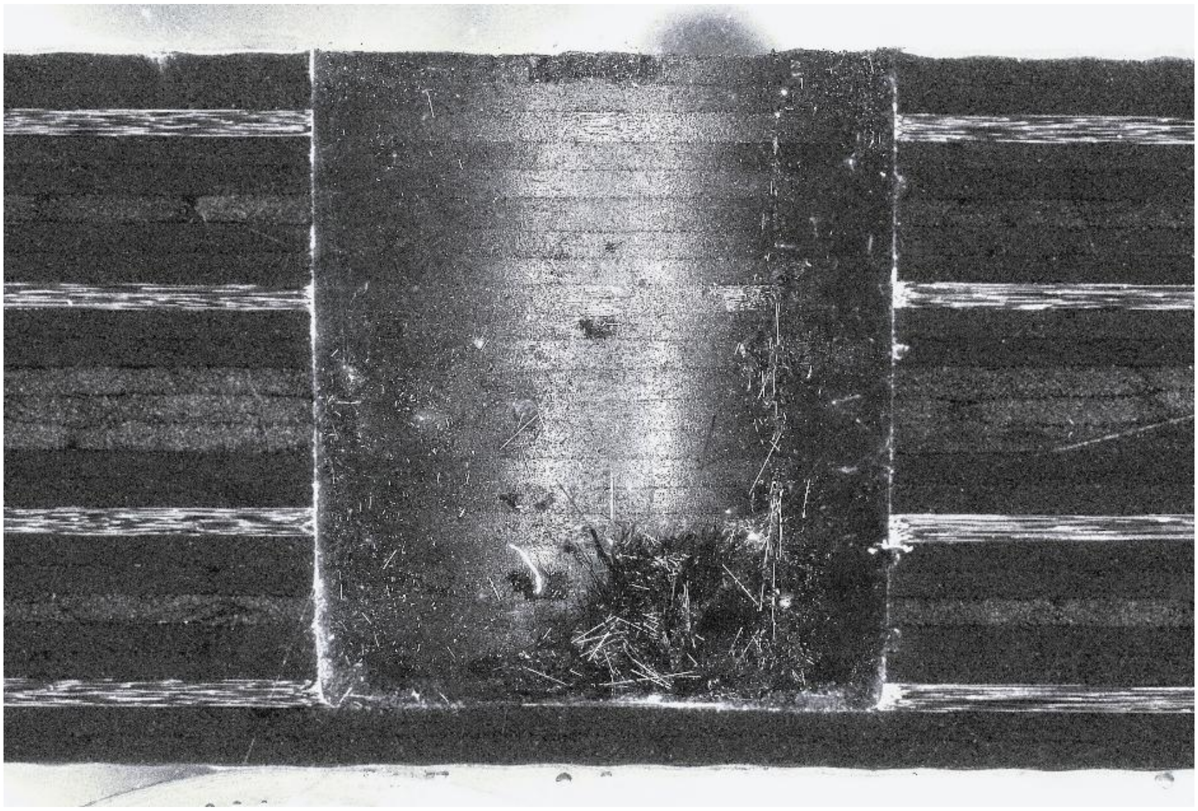

Figure 3.25 Hole NV-02: Drilled hole **without** vacuum jig of specimen CSAI - RPR - S - 20J - 1. Tools used: Amamco TDR chased by an End Mill.

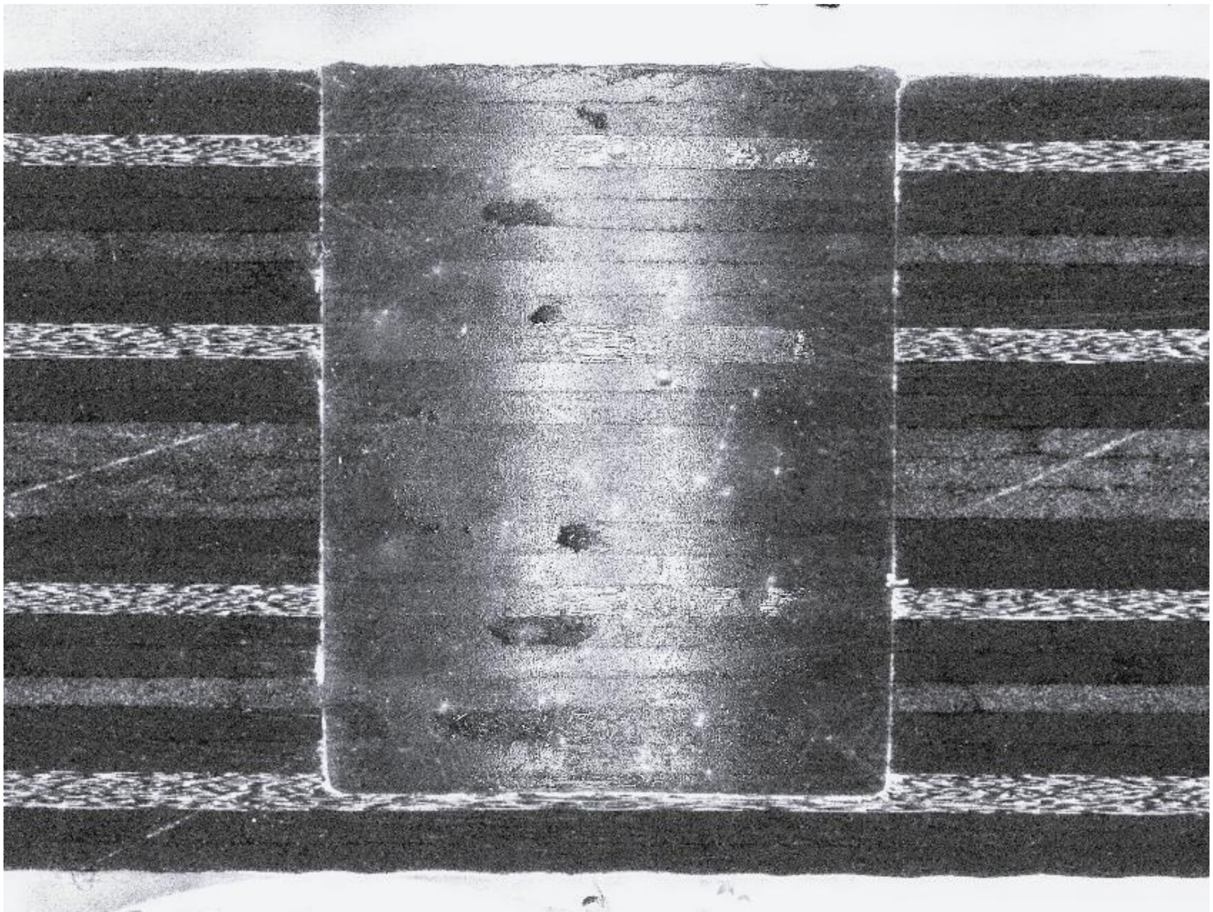

Figure 3.26 Hole V-01: Drilled hole **with** vacuum jig of specimen CSAI - RPR - S - 20J - 1.
Tools used: Amamco TDR chased by an End Mill.

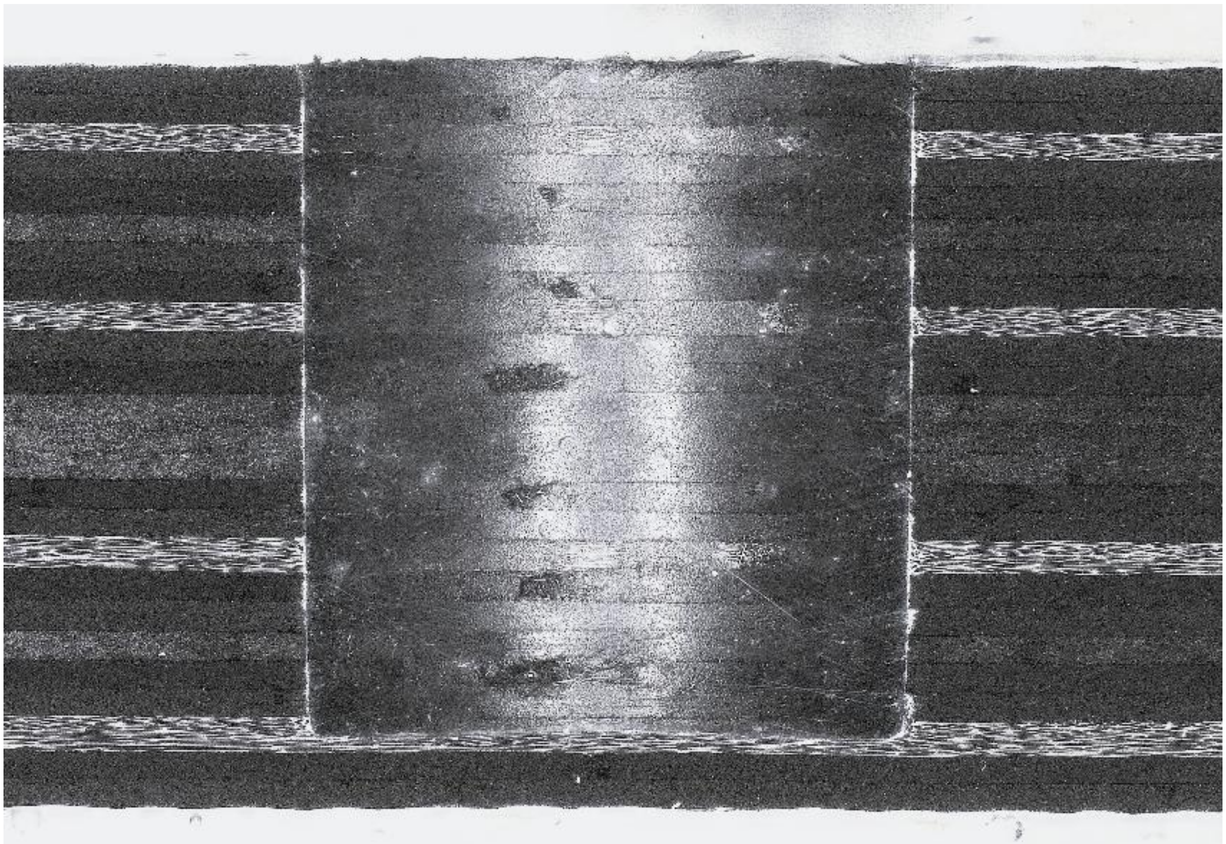

Figure 3.27 Hole V-02: Drilled hole **with** vacuum jig of specimen CSAI - RPR - S - 20J - 1. Tools used: Amamco TDR chased by an End Mill.

Both holes drilled without the vacuum jig exhibit significant quantities of debris either adhered to the hole surface or accumulated at its base. Figure 3.28 shows a close-up view of Hole NV-01, revealing two distinct types of debris contaminants: elongated fiber strands and fine fiber dust. Hole NV-02 exhibits both types of composite debris, albeit in larger quantities, as seen in Figure 3.29. In contrast, Holes V-01 and V-02 exhibit no signs of debris contamination, thereby demonstrating the effectiveness of the custom vacuum jig developed as part of this work.

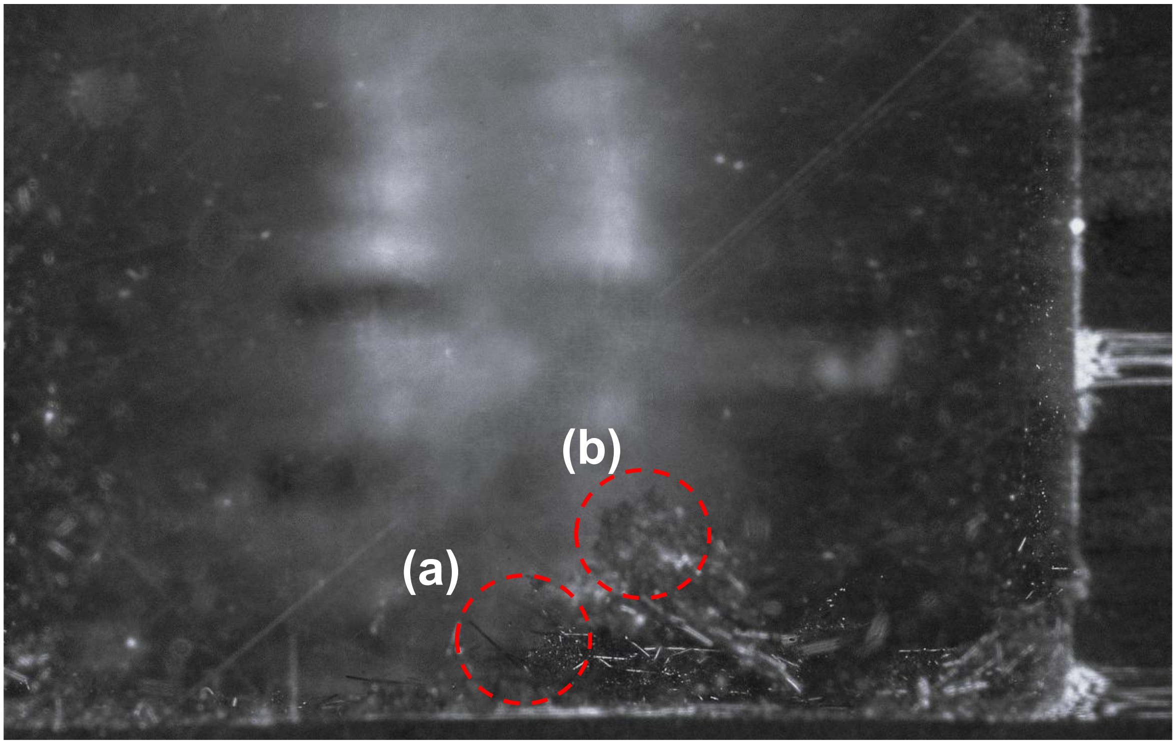


Figure 3.28 Composite debris in Hole NV-01: (a) Fiber strands, and (b) fiber dust.

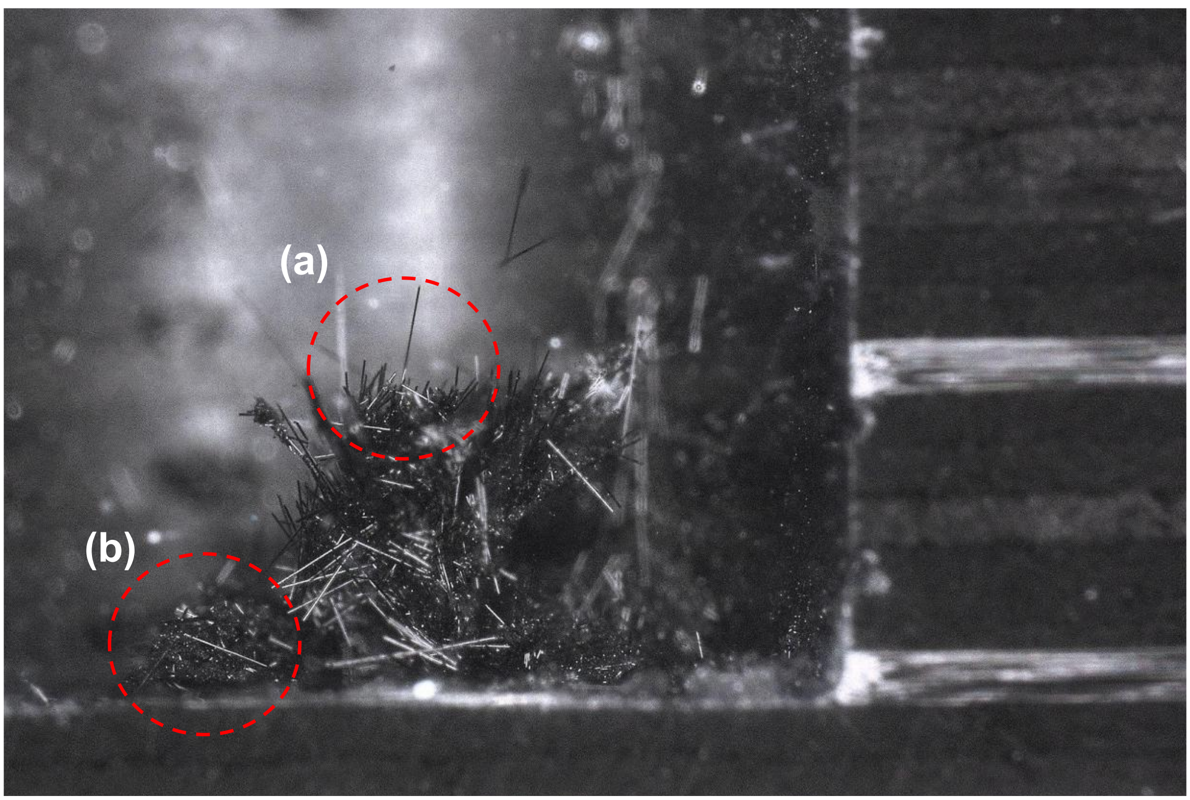


Figure 3.29 Composite debris in Hole NV-02: (a) Fiber strands, and (b) fiber dust.

Moreover, after drilling the holes without the vacuum jig, significant quantities of composite debris were observed adhering to the surface surrounding the holes even after post-drilling vacuum cleaning, as seen in Figure 3.30. This is identified to be a source of hole contamination during drilling, as residual surface debris may fall into the hole prior to resin injection. The principal advantage of the vacuum jig is the continuous, high-speed airflow generated across the hole surface during drilling, which dislodges debris from both the top surface and the interior of the hole, as explained in Section 3.2.2. Nevertheless, it is possible to mitigate debris contamination without the use of a custom vacuum jig by introducing compressed air flowing across the surface of the specimen to enhance the suction mechanism (induced by flow across hole opening) and promote active debris expulsion from the holes.

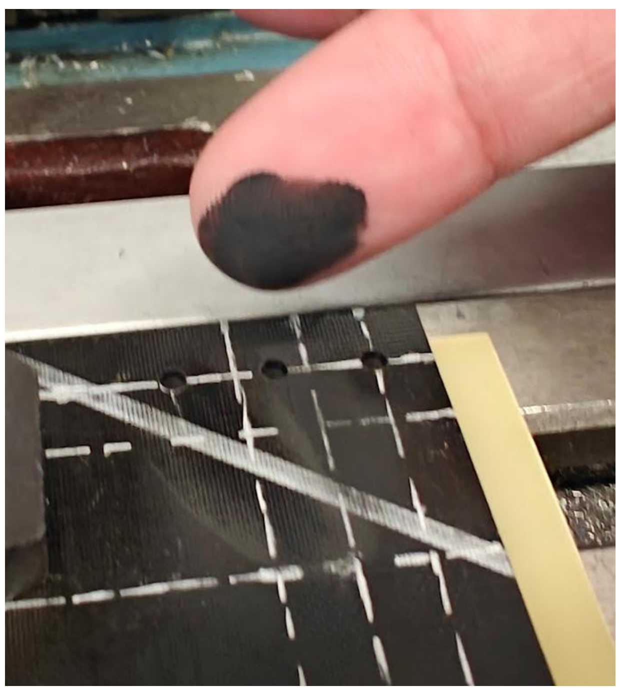

Figure 3.30 Remaining composite debris adhered to surface of specimen after vacuuming.

# CHAPTER 4: DISCUSSION, CONCLUIONS, AND FUTURE WORK

## 4.1 Discussion

While the injection repair process remains under development — as complete delamination fill and strength restoration have not yet been achieved — the work presented in this thesis offers novel contributions to the broader research effort toward qualifying injection repair for strength-restoring applications. These include the development of a Python code that reconstructs C-scan data into three-dimensional plots of delaminations, the development of a novel visualization method that highlights the damage network branches within impacted composites, the establishment of a set of drilling parameters that consistently and repeatably mitigate drilling-induced damage, and the development of a vacuum-assisted debris extraction method that prevents hole contamination and clogging of pre-existing delaminations during drilling. In particular, the use of density maps for NDE-informed injection hole placement may represent a significant advancement in the repair process, by targeting zones containing the most interconnected percolation pathways through which the repair resin can infiltrate the greatest number of delaminations, as seen in Figure 4.1. Compared to previous approaches in which hole placement was determined without quantitative damage mapping, this tool enables a deeper understanding of the complex delamination network and its connectivity via matrix cracks, that can be leveraged for the advancement of injection repair toward structural qualification.

(a)

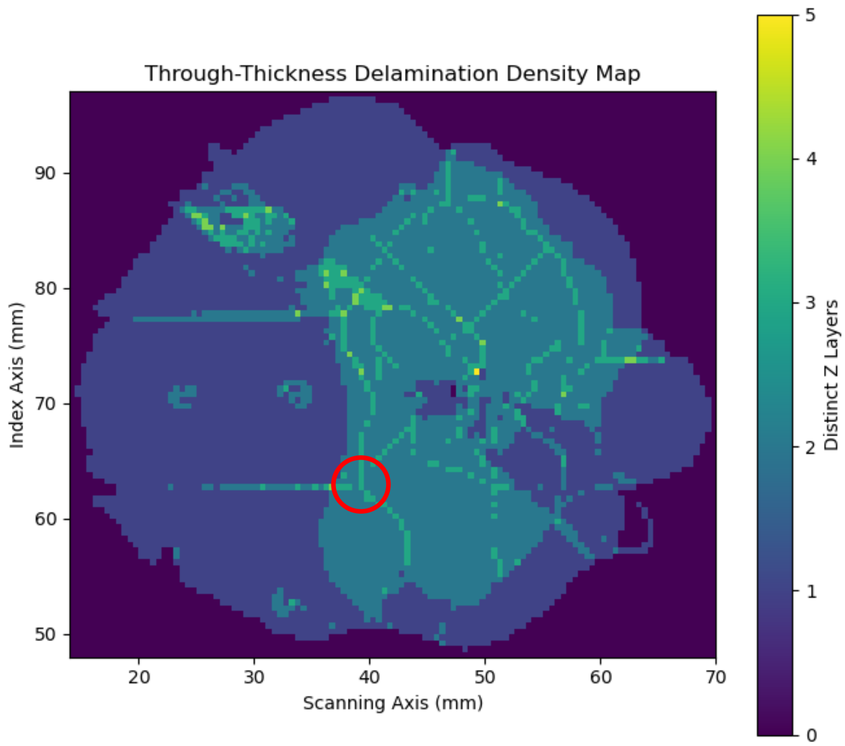


(b)

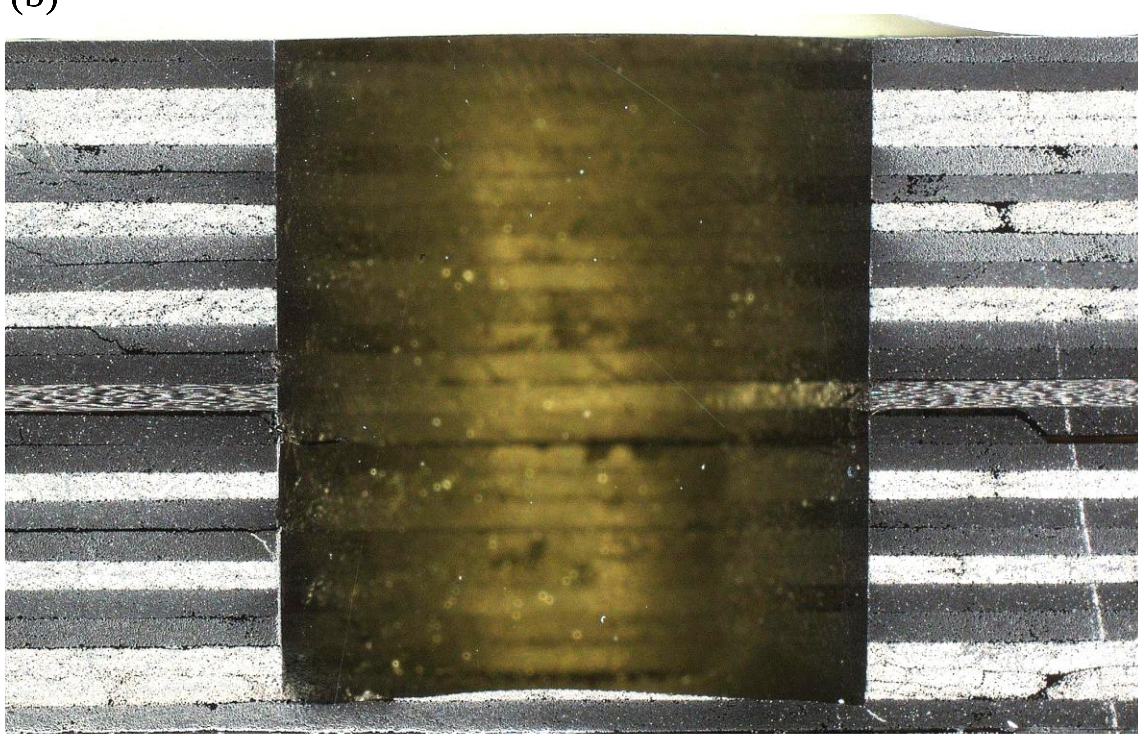

Figure 4.1 Injection repaired CFRP composite: (a) Hole location on delamination density map, and (b) cross section showing the drilled hole connecting different delamination planes.

## 4.2 Conclusions

The Python code presented in this thesis successfully generated two-dimensional and three-dimensional visualizations of waveform data from pulse-echo ultrasonic testing of impact-damaged composite laminates. The numerical transformations performed to reorient the data depending on the surface from which the specimen was scanned proved consistent and reliable. The application of the 95th percentile data population range enabled robust automatic outlier removal for C-scans containing abnormal signal readings (typically at the specimen edges). The use of threshold coefficients and the Euclidean distance successfully isolated damage readings from complete C-scan datasets, regardless of damage network size or morphology. Furthermore, the discovery of the role of delamination having their own finite thickness in the z-direction in the alignment of front- and back-surface C-scans provided a reliable initial offset for the development of combined-hybrid reconstructed C-scans. The use of dataset centroids for automatic spatial alignment also yielded promising results, with several cases in which automatic alignment alone was sufficient when combining front- and back-surface scans. The resulting hybrid plots provided an intuitive visualization of damage in impacted composites, especially following injection repair, where changes in the damage network morphology were more clearly identified versus viewing the datasets only in two dimensions. Finally, the development of density maps that count the number of damage layers in the z-direction incidentally gave rise to a novel visualization method that highlights the delamination network branches, which may enable an enhanced level of impact damage morphology understanding via pulse-echo ultrasonic testing.

The results from the drilling experiments underscore the significant influence of feed rate on the machining of composites. Across both drilling and cutting operations, increasing the feed rate produces greater damage at the machined surface. Cutting speed was also found to be a critical parameter; excessively low cutting speeds promote heat generation, tool vibration, and accelerated damage to the composite. In summary, small drill bit diameters (< 0.118 in.), high spindle speeds (> 2,000 rpm), low helix angles (< 30°), low feed rates (< 0.02 in./peck), and moderate cutting speeds, depending on feed rate, (> 0.33 peck/s) have been shown to minimize drilling-induced damage. In parallel, the implementation of high-velocity airflow across the hole surface during drilling — even without a custom vacuum jig — can effectively prevent both clogging of pre-existing delaminations and debris adhesion to the hole surface, by generating shear forces and pressure differentials that direct loosened debris out of the hole and into the vacuum hose.

## 4.3 Future Work

During the drilling experiments, it was observed that drilling composites with different layup configurations — even when fabricated from the same material— yielded considerably different results despite the application of the same parameters. Therefore, further experiments on composites with various layup configurations and materials are necessary to develop an all-encompassing set of drilling parameters that can be adapted to the material and layup configuration being machined.

The results produced by the density plots, although promising, remain incompletely understood. A more detailed investigation of each individual waveform comprising the delamination network branches is required to determine the extent to which matrix cracks contribute to the reflected signal and how the Python code processes these readings. Furthermore, additional analysis of the three-dimensional C-scans in regions where delaminations intersect is required, as this may reveal key characteristics of how delamination interfaces are detected by the ultrasonic transducer. Finally, in some cases, the network branches identified in the density plots resemble the outline patterns characteristic of stair-step delamination propagation, which is governed by the laminate layup configuration. Further analysis can therefore be conducted to establish correlations between the patterns observed in the density plots and the ply-angle-driven propagation of damage in impacted CFRP composites.

# APPENDIX A: CODE LINKS

**Code:**

GitHub:

https://github.com/CVV-mx/3D-UT-Python

APPENDIX B: MICROGRAPHS OF DRILLED HOLES

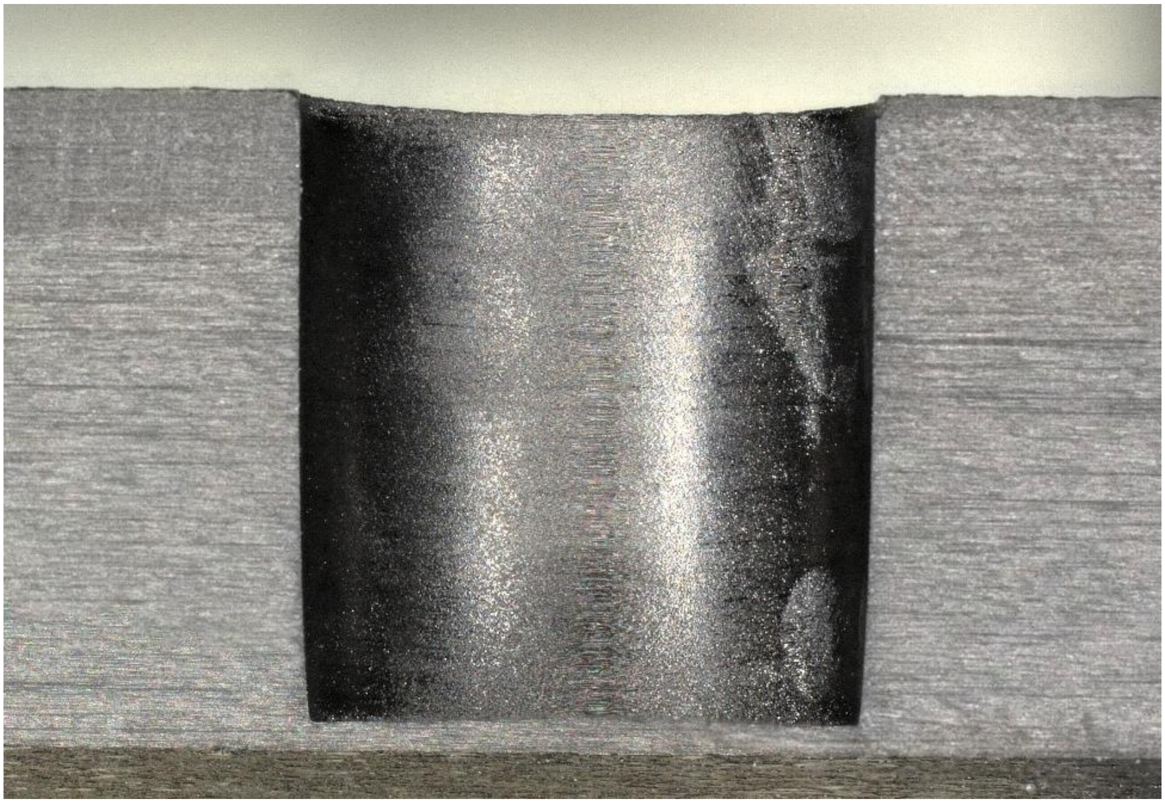

Figure B.1 Cross-section micrograph of drilled hole #1 of ENF Specimen. Drilling parameters: Pecking rate: 0.01 in/pec, spindle speed: 2500 rpm, cutting speed: 0.33 peck/s. Tools used: Amamco TDR chased by an End Mill.

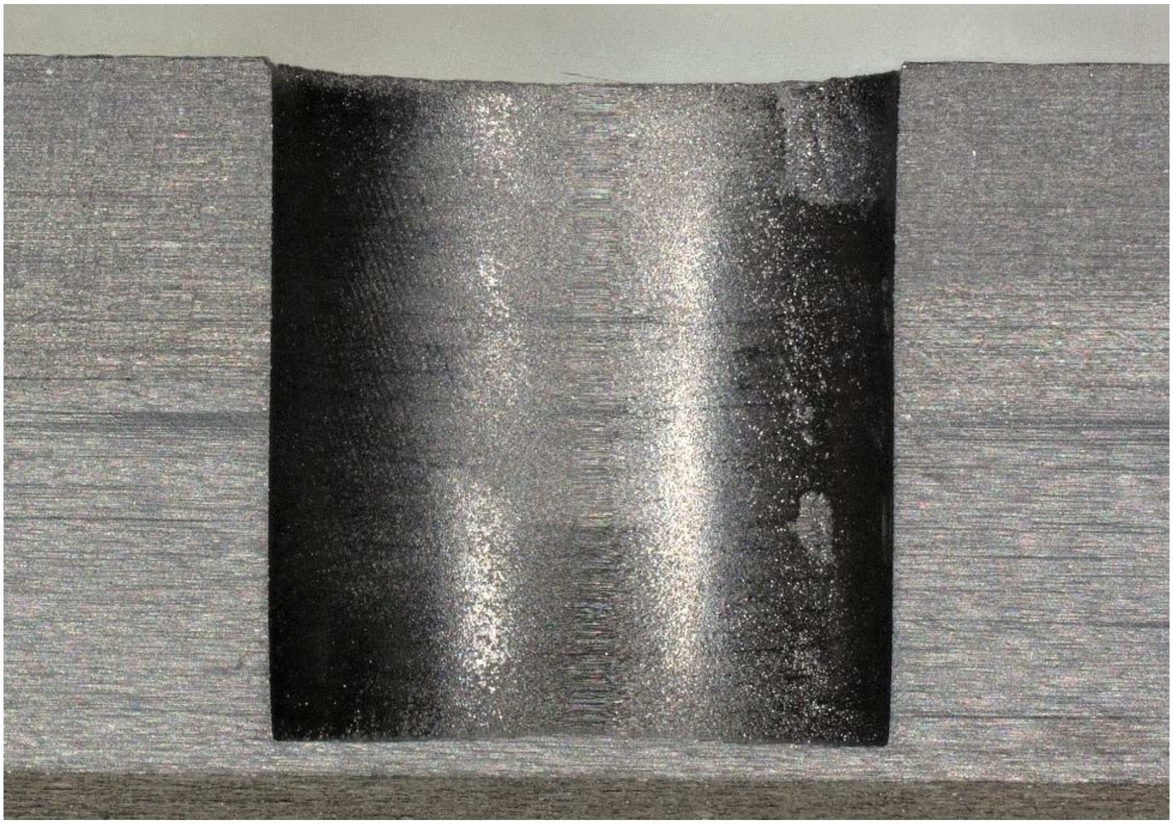

Figure B.2 Cross-section micrograph of drilled hole #2 of ENF Specimen. Drilling parameters: Pecking rate: 0.01 in/pec, spindle speed: 2500 rpm, cutting speed: 0.33 peck/s. Tools used: Amamco TDR chased by an End Mill.

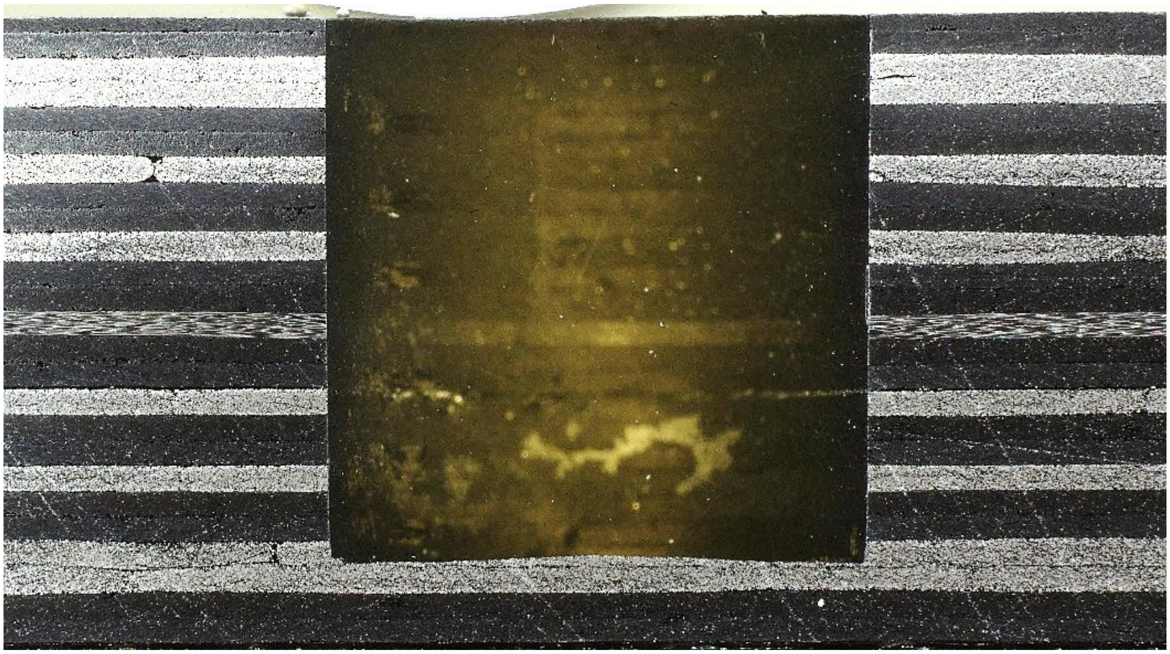

Figure B.3 Cross-section micrograph of drilled hole #1 of CSAI Medium specimen after injection repair. Drilling parameters: Pecking rate: 0.01 in/pec, spindle speed: 2500 rpm, cutting speed: 0.33 peck/s. Tools used: Amamco TDR chased by an End Mill.

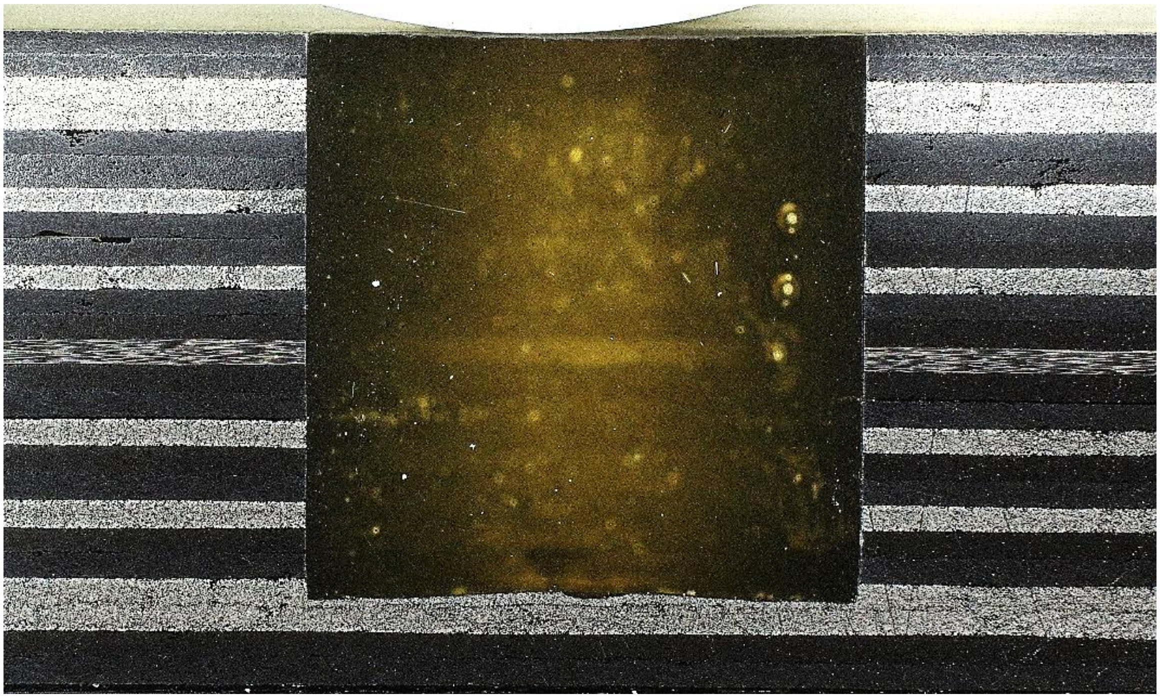

Figure B.4 Cross-section micrograph of drilled hole #2 of CSAI Medium specimen after injection repair. Drilling parameters: Pecking rate: 0.01 in/pec, spindle speed: 2500 rpm, cutting speed: 0.33 peck/s. Tools used: Amamco TDR chased by an End Mill.

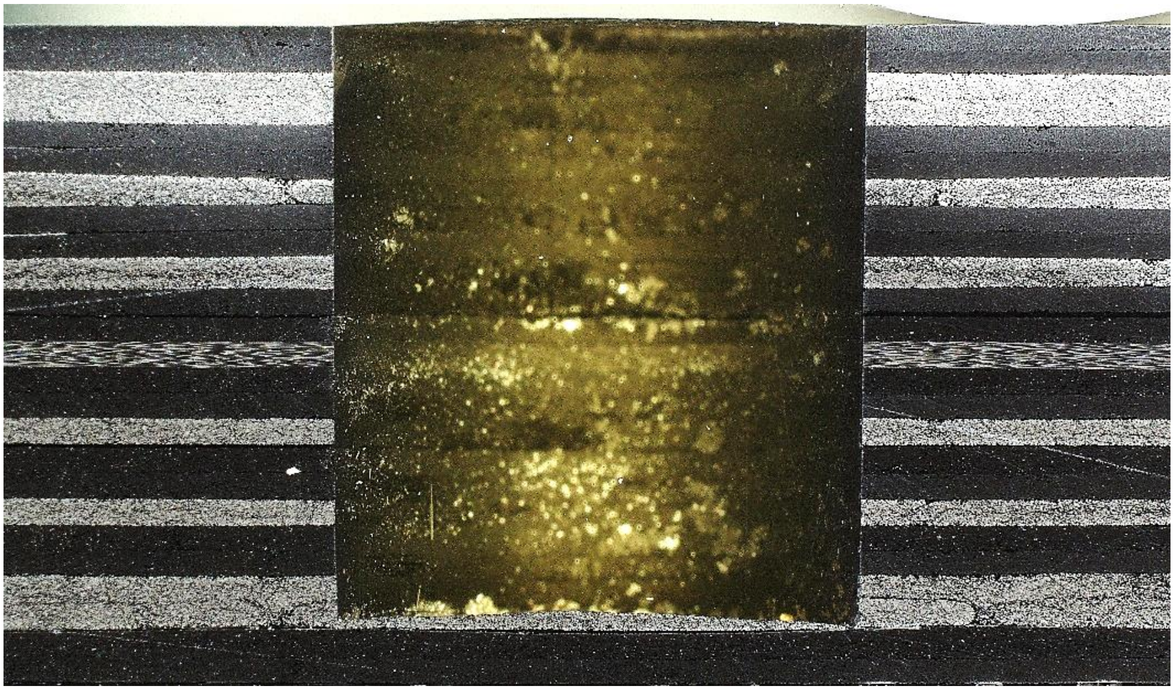

Figure B.5 Cross-section micrograph of drilled hole #3 of CSAI Medium specimen after injection repair. Drilling parameters: Pecking rate: 0.01 in/pec, spindle speed: 2500 rpm, cutting speed: 0.33 peck/s. Tools used: Amamco TDR chased by an End Mill.

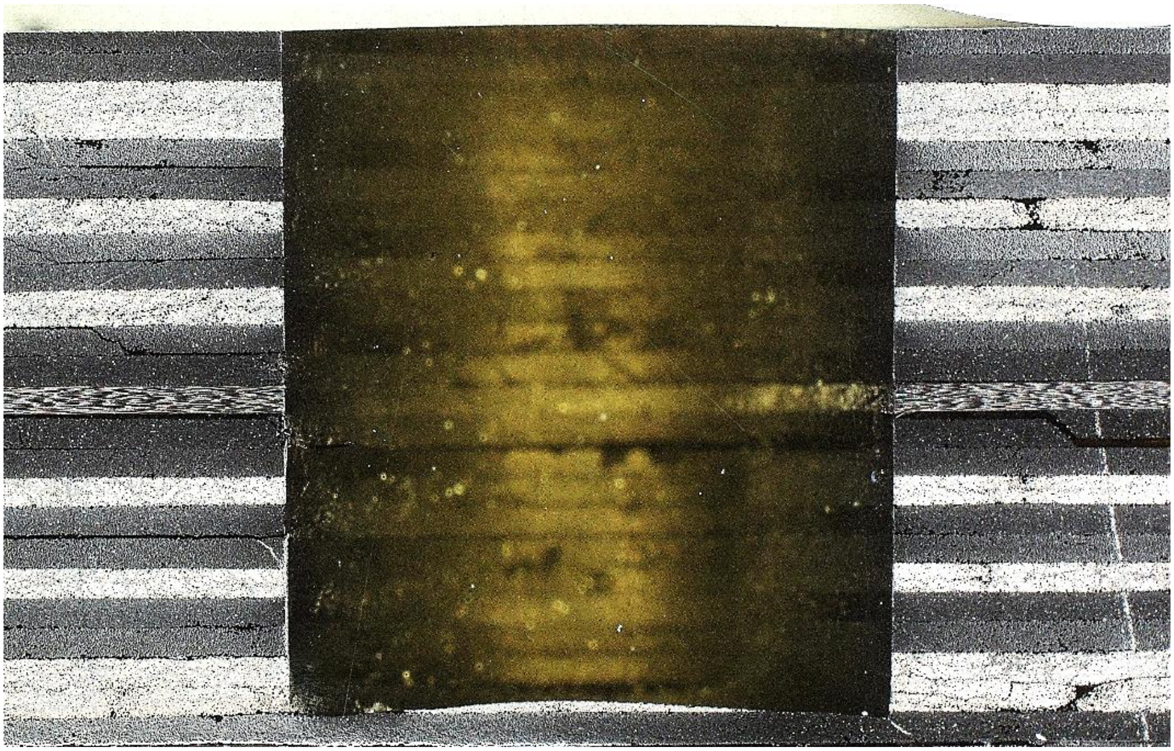

Figure B.6 Cross-section micrograph of drilled hole #4 of CSAI Medium specimen after injection repair. Drilling parameters: Pecking rate: 0.01 in/pec, spindle speed: 2500 rpm, cutting speed: 0.33 peck/s. Tools used: Amamco TDR chased by an End Mill.

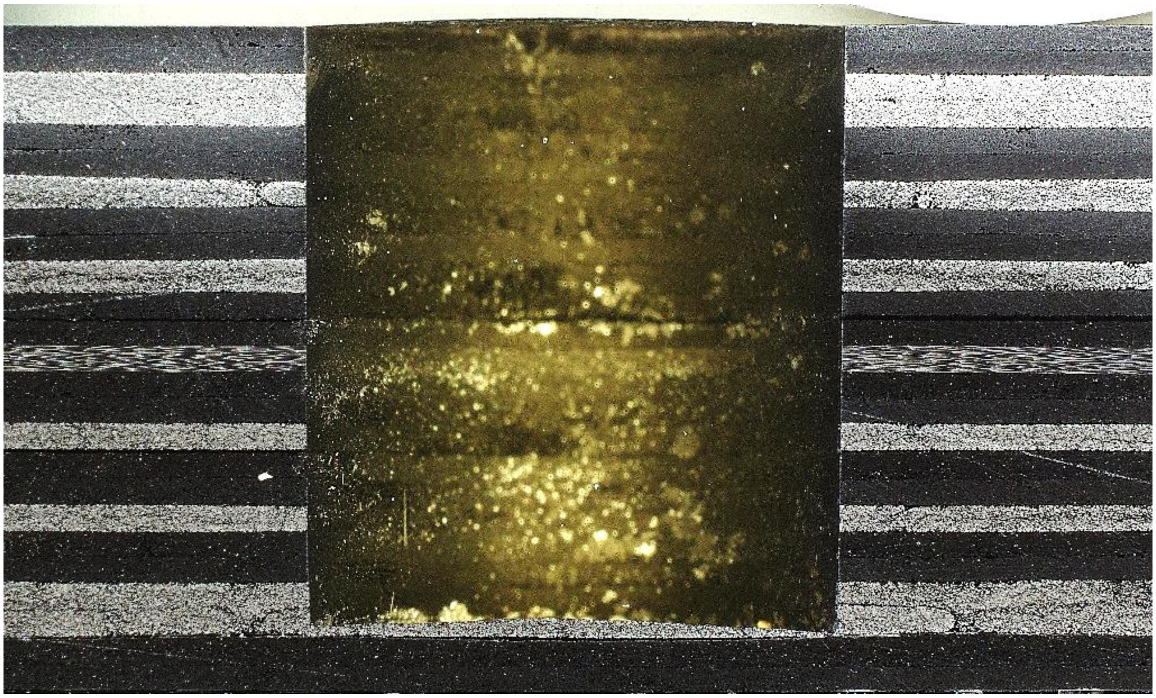

Figure B.7 Cross-section micrograph of drilled hole #5 of CSAI Medium specimen after injection repair. Drilling parameters: Pecking rate: 0.01 in/pec, spindle speed: 2500 rpm, cutting speed: 0.33 peck/s. Tools used: Amamco TDR chased by an End Mill.

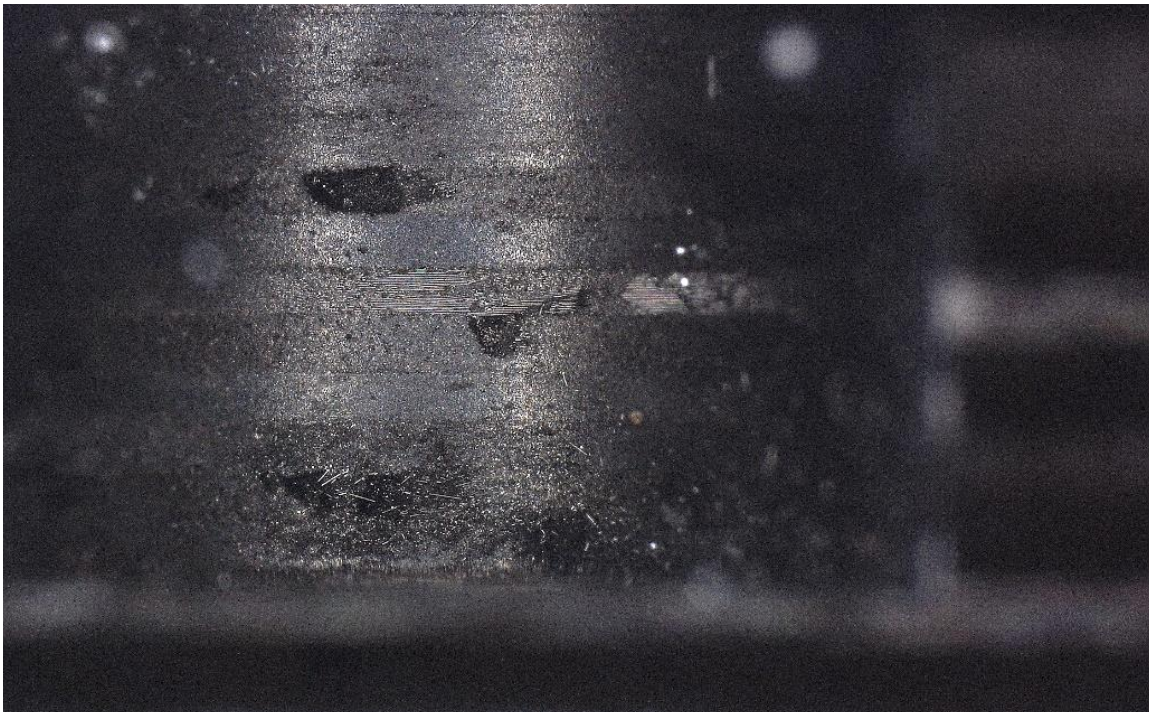

Figure B.8 Micrograph of composite debris trapped inside Hole NV-03 after drilling. Drilling parameters: Pecking rate: 0.01 in/pec, spindle speed: 2500 rpm, cutting speed: 0.33 peck/s. Tools used: Amamco TDR chased by an End Mill.

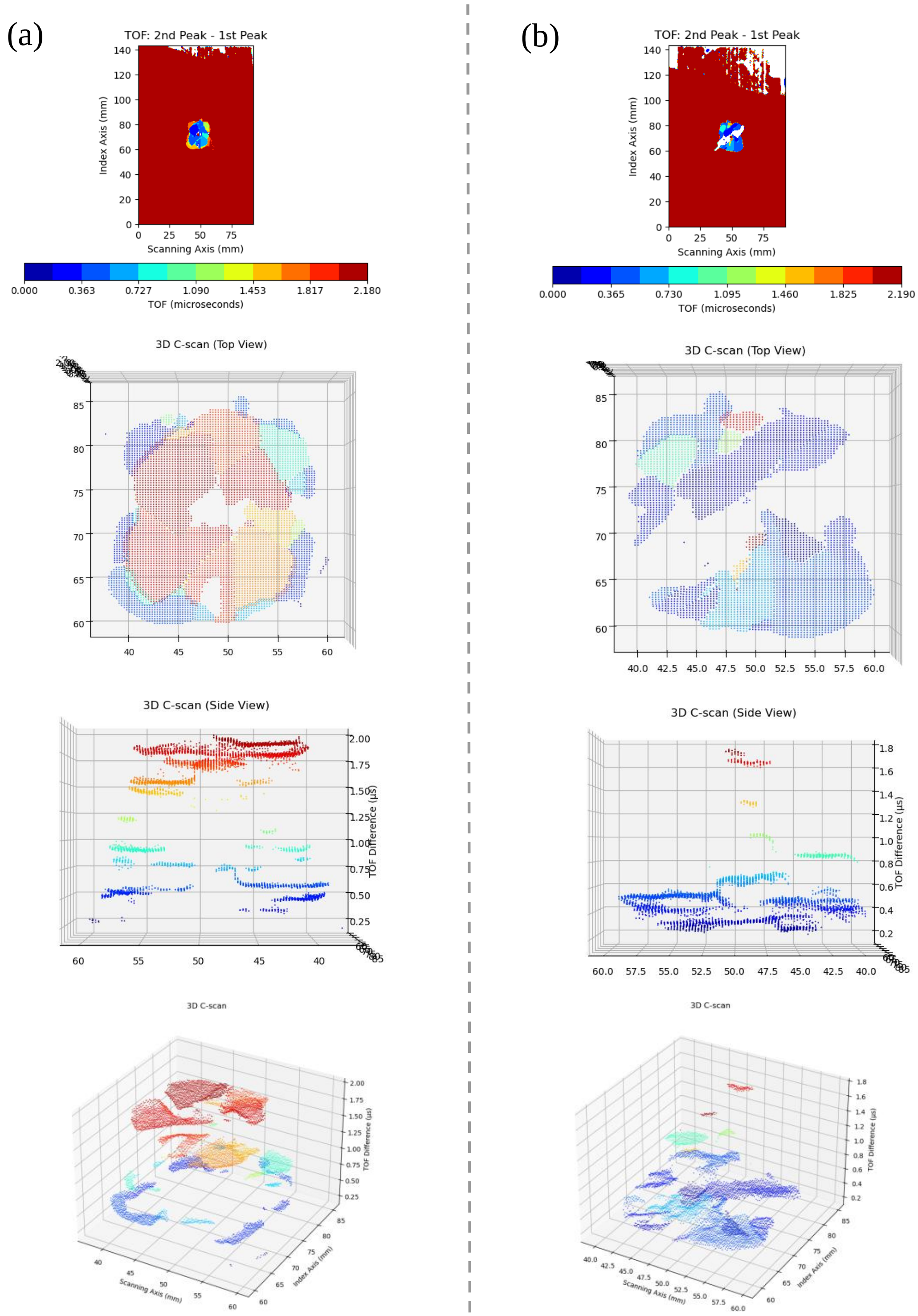


Figure C.1 `cscan_plots()` plot package: Specimen CSAI - CONT - HARD - 10J – 1: (a) Front scan, (b) Back scan.

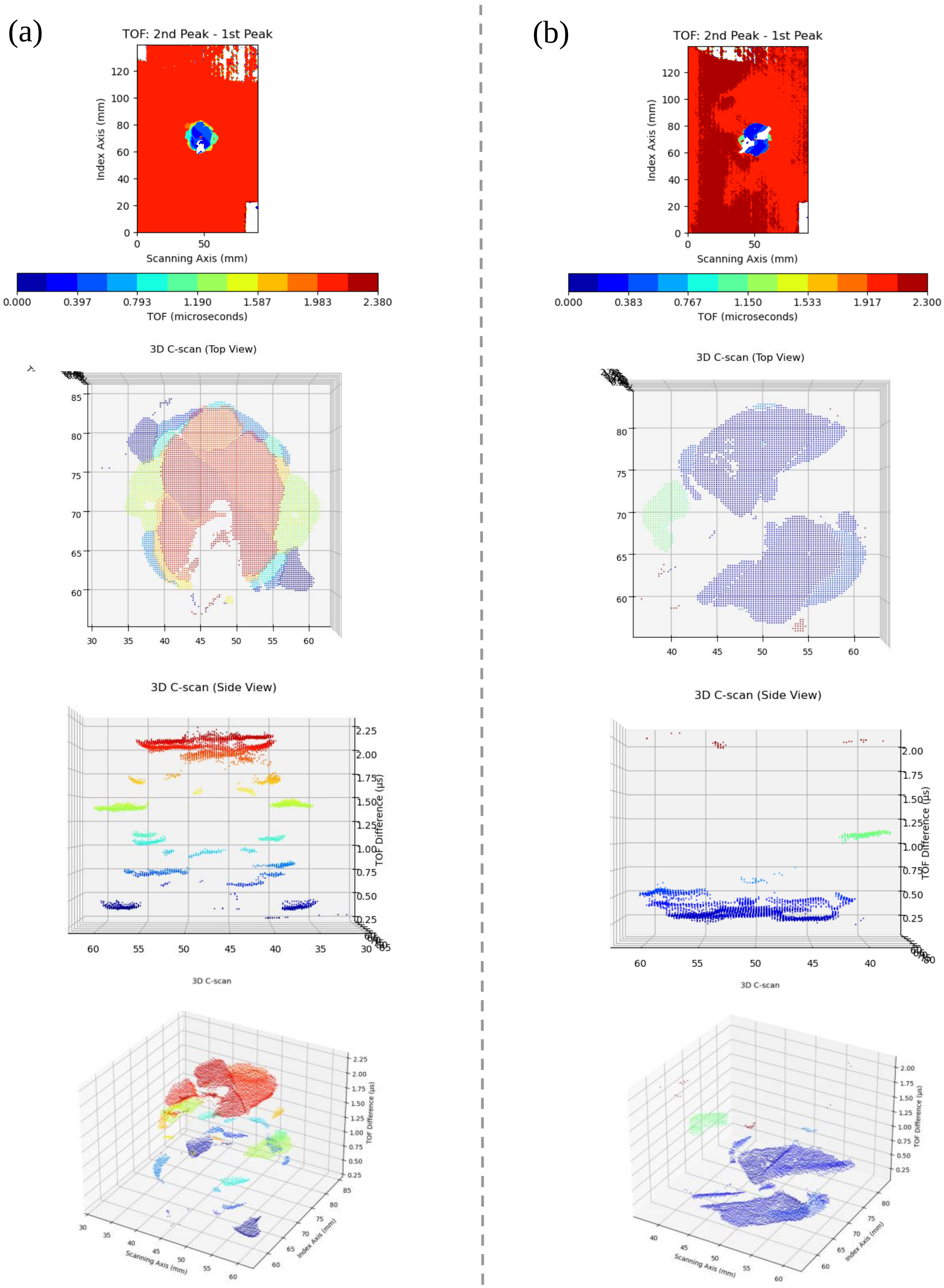


Figure C.2 `cscan_plots()` plot package: Specimen CSAI - RPR - HARD - 10J – 2: (a) Front scan, (b) Back scan.

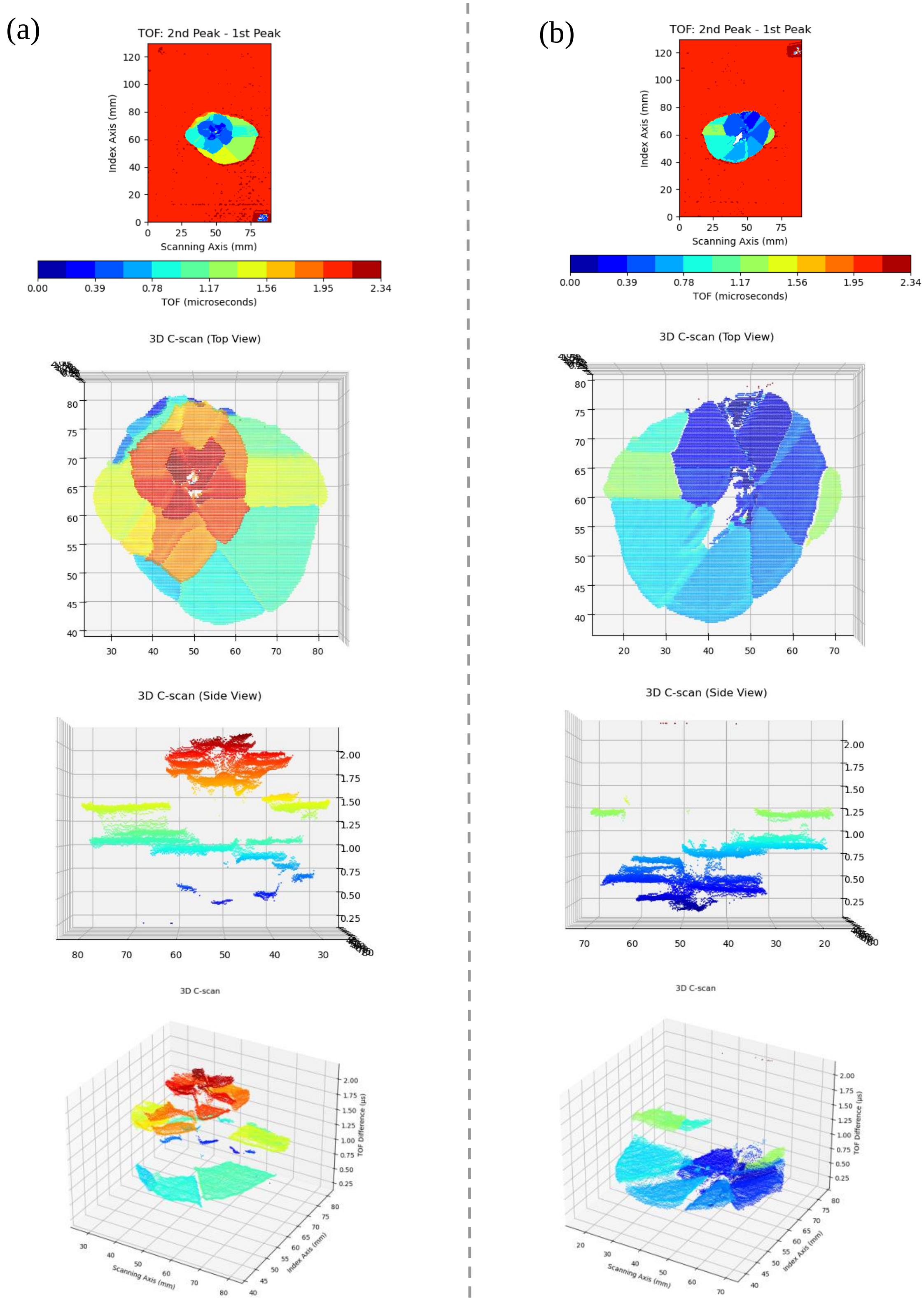


Figure C.3 `cscan_plots()` plot package: Specimen CSAI - RPR - SOFT - 15J – 2: (a) Front scan, (b) Back scan.

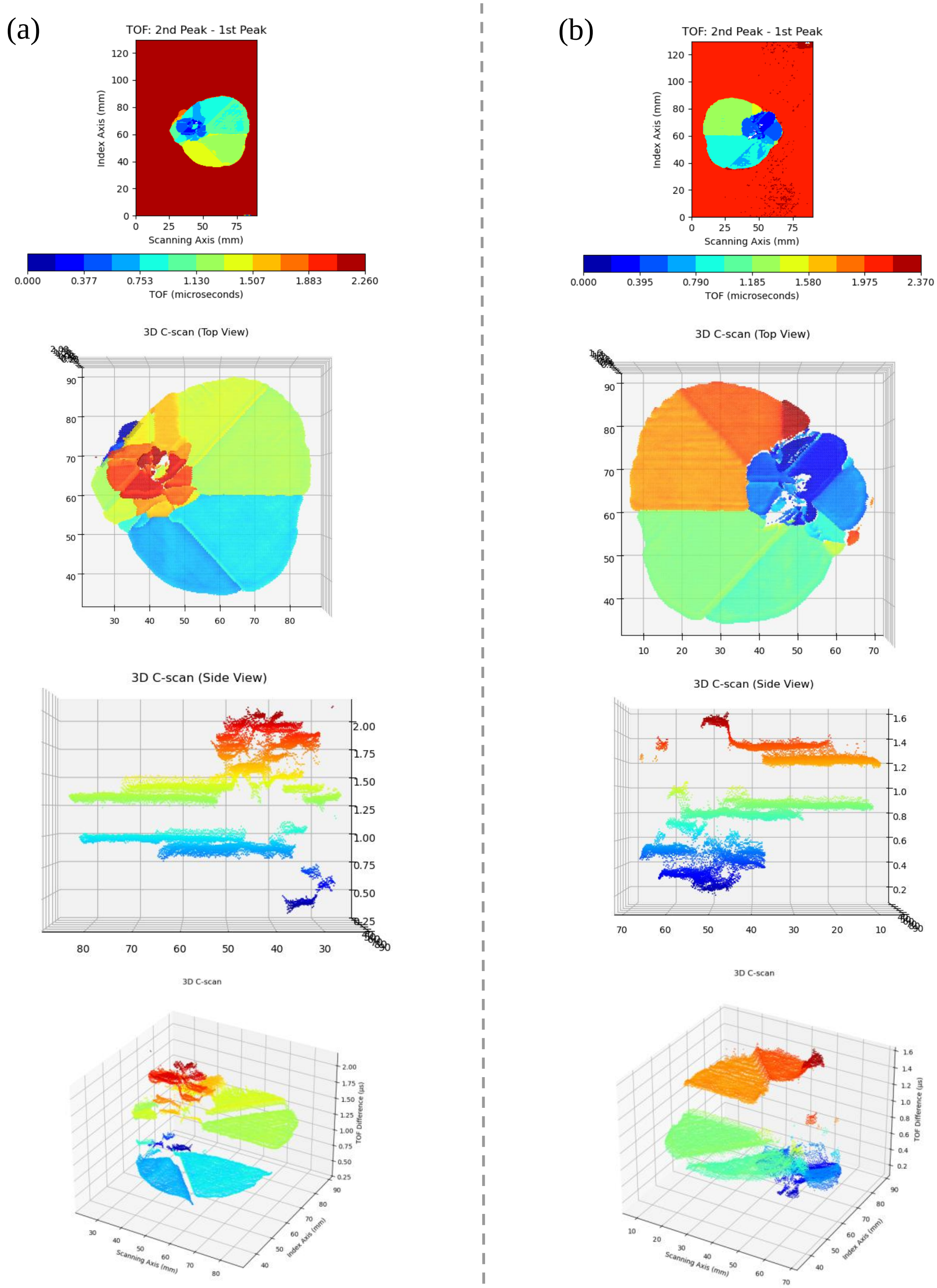


Figure C.4 `cscan_plots()` plot package: Specimen CSAI - RPR - SOFT - 15J – 3: (a) Front scan, (b) Back scan.

## APPENDIX D: `hybrid_cscan_plots()` PLOT EXAMPLES

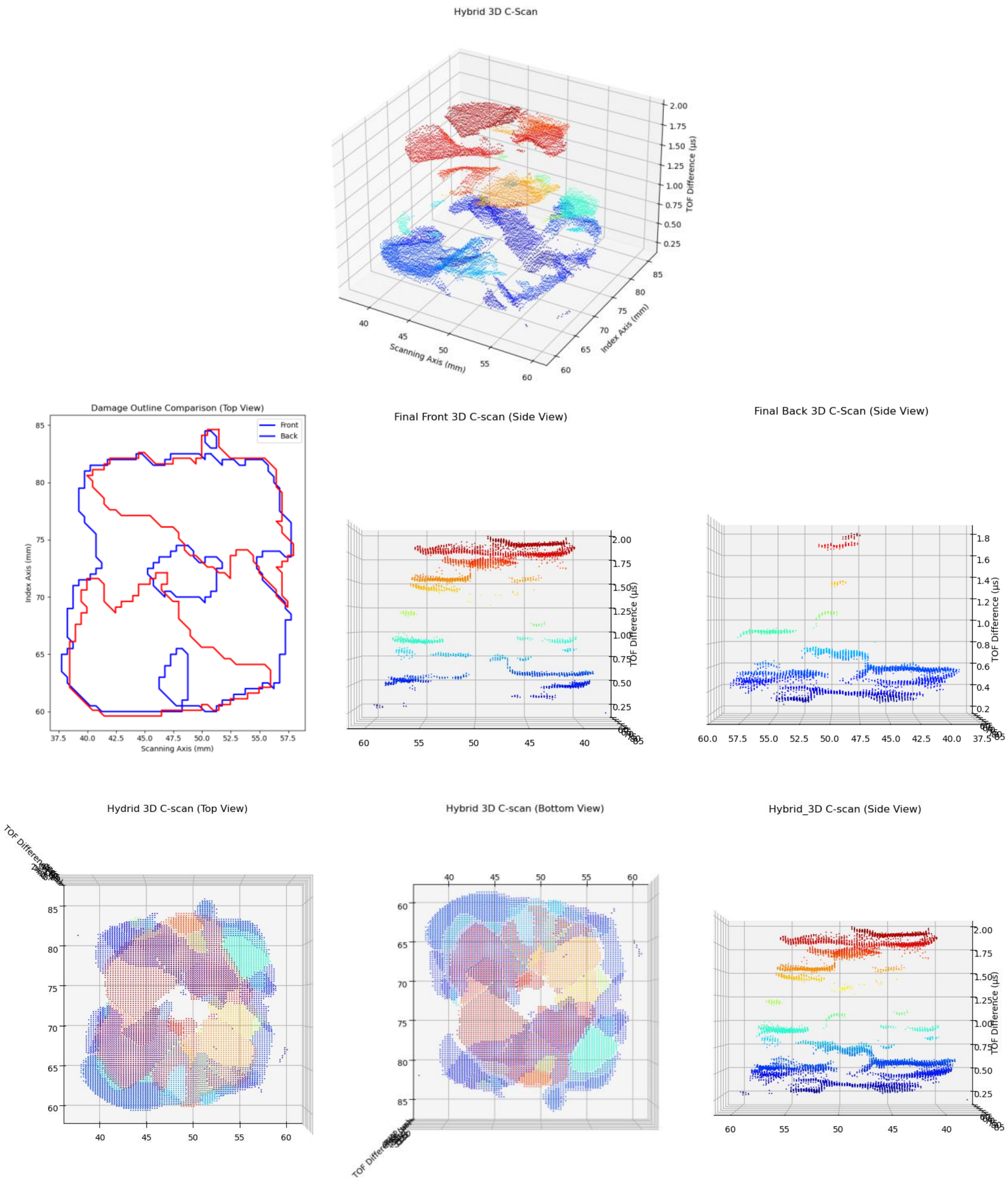


Figure D.1 `hybrid_cscan_plots()` plot package: Specimen CSAI - CONT - HARD - 10J – 1.

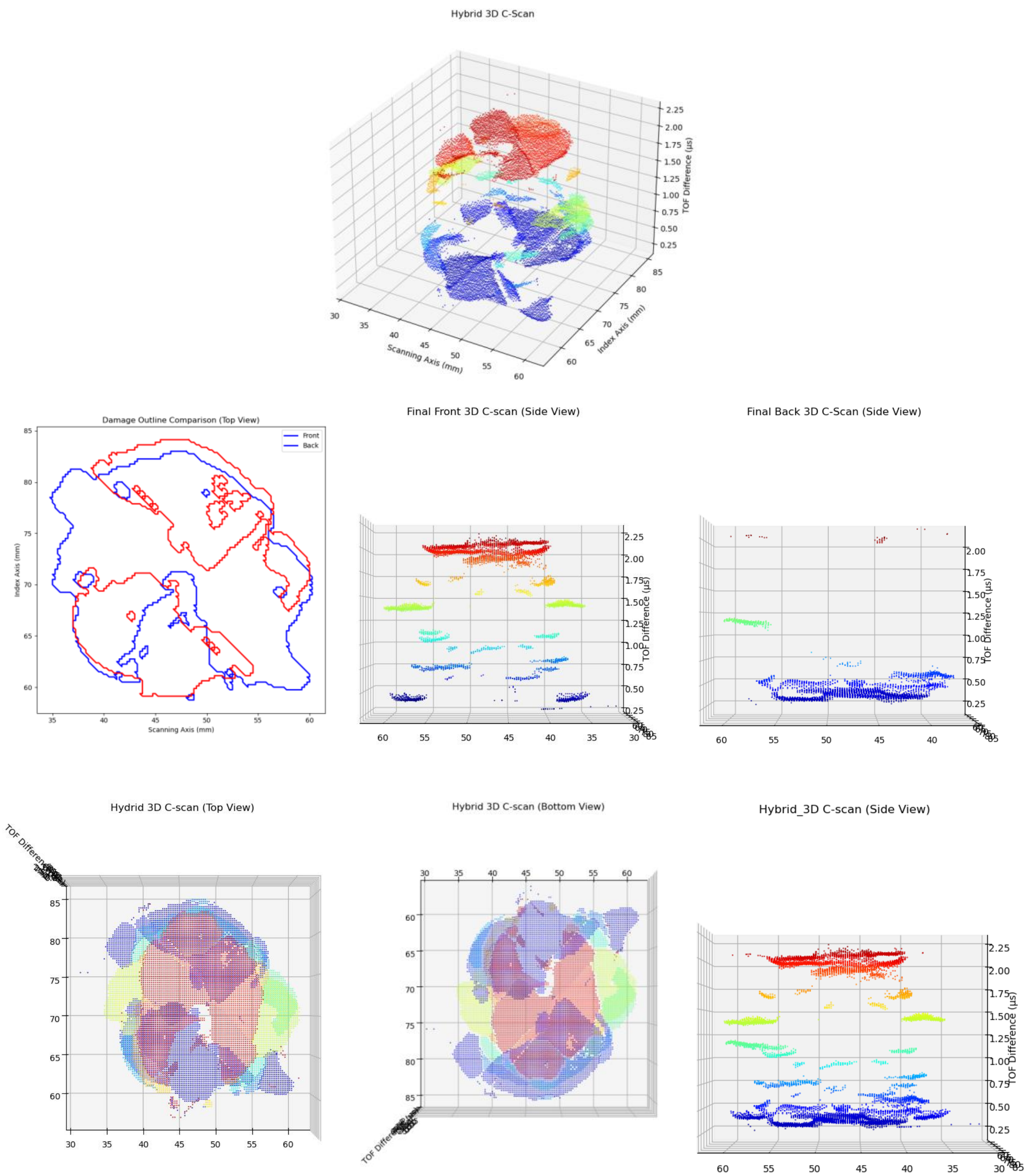


Figure D.2 `hybrid_cscan_plots()` plot package: Specimen CSAI - RPR - HARD - 10J – 2.

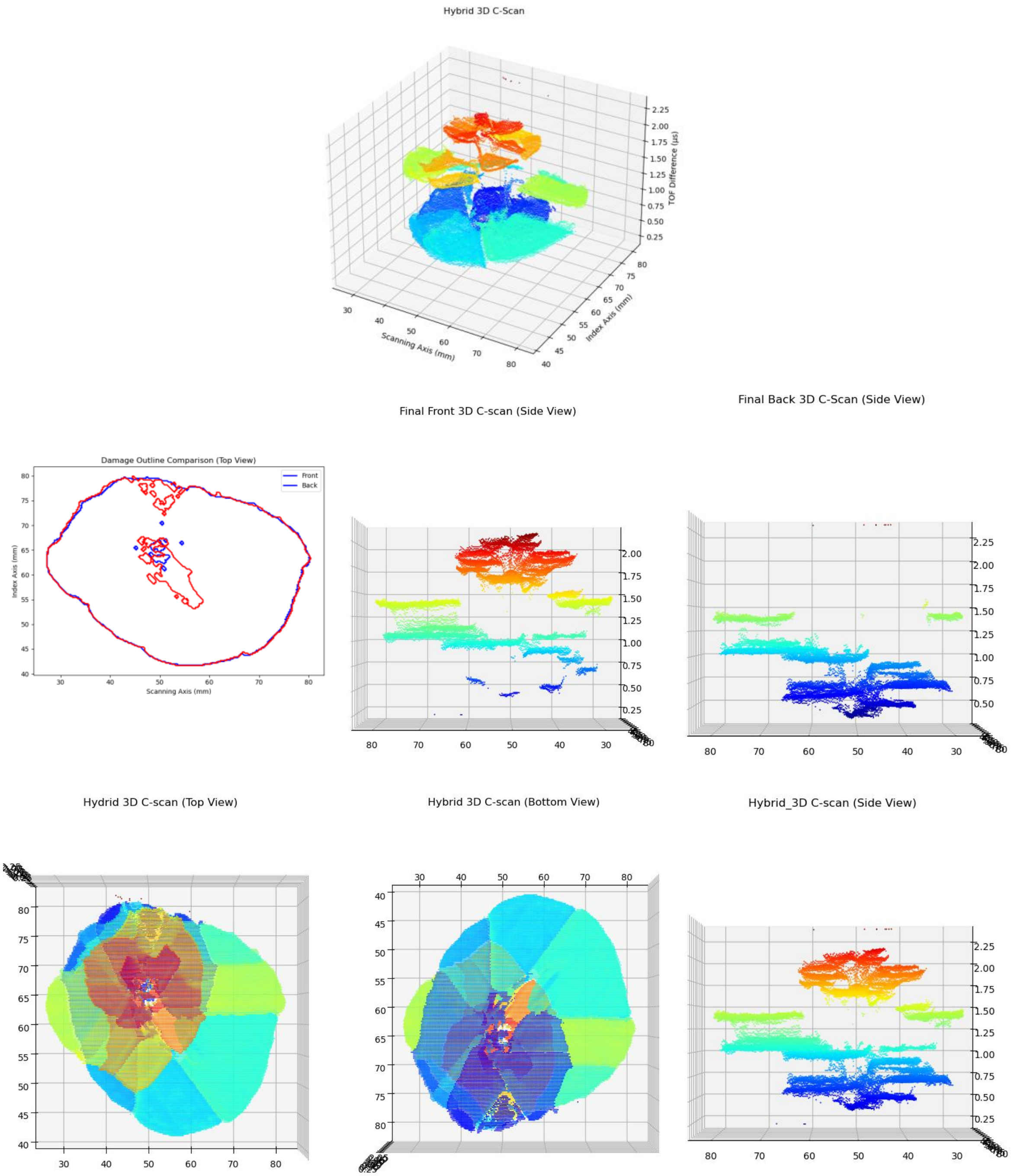


Figure D.3 `hybrid_cscan_plots()` plot package: Specimen CSAI - RPR - SOFT - 15J – 2.

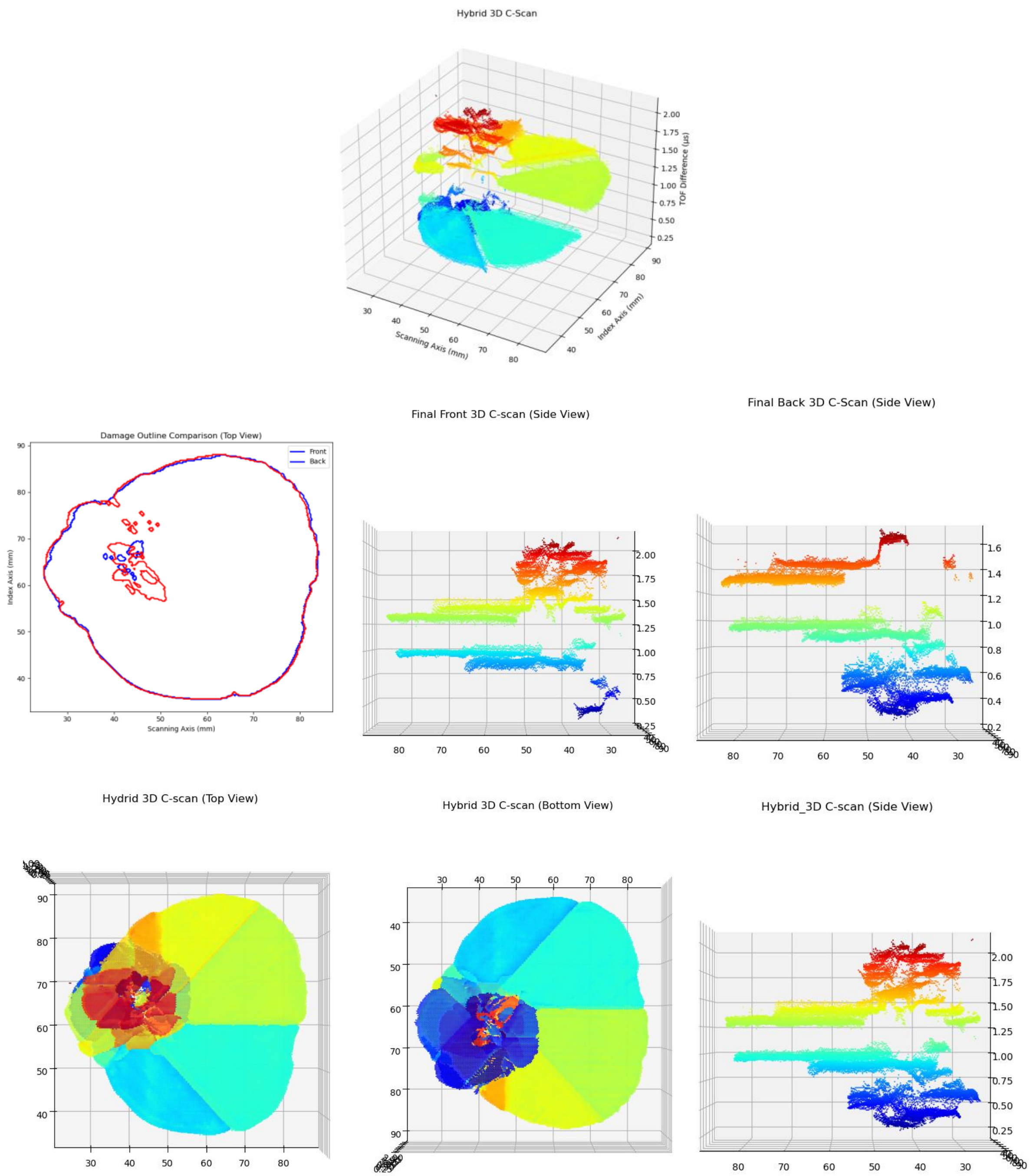


Figure D.4 `hybrid_cscan_plots()` plot package: Specimen CSAI - RPR - SOFT - 15J – 3.

# APPENDIX E: MICROSCOPY SAMPLE MAKING PROCESS

To obtain micrographs of the cross-sectional profiles of the drilled holes, the composite specimens were segmented into pieces of at most 2 inches in length and width using a wet-tile saw. The cross-sectional cuts through the holes were performed using a Struers Accutom-5 precision saw at a feed rate of 0.1 mm/s. All microscopy samples had an average length of 1 inch, which depended on the dimensions of the available mounting molds.

After cutting, the samples were mounted in 1-inch silicone molds using a hot-mounting QuickSet resin manufactured by Allied. Following mounting, the specimens were sanded using silicon carbide (SiC) abrasive paper of grits 500, 800, 1000, and 1200, in that order, mounted on a rotating polishing disk manufactured by Struers. Sanding was performed by applying a downward force at the center of the sample to uniformly distribute the load until the scratch marks from the previous grit were no longer visible. With each grit change, the sample was rotated 90°. Multiple passes with the 800, 1000, and 1200 grit papers may be required to progressively refine the surface until no residual scratch marks were visible under microscopic inspection. After sanding, the samples were polished using a diamond suspension and a dedicated polishing pad.

For the vacuum jig experiments, an off-the-shelf casting epoxy manufactured by Shabebe was used to fill the drilled holes and retain any residual particles prior to sectioning. The casting resin was slowly mixed to reduce bubble formation; once the solution became homogeneous, it was allowed to rest for approximately 5 minutes, enabling any residual air bubbles to rise to the surface. Once the epoxy was ready, it was slowly injected into the hole using a disposable plastic pipette with a fine-tip attachment, starting at the base of the hole, and advancing gradually toward the surface to prevent large air bubbles from becoming trapped during injection. Following injection, an additional layer of epoxy was applied over the hole opening to compensate for resin evaporation or infiltration into voids within the composite.

REFERENCES

Bi, Z. (2011). Design and simulation of dust extraction for composite drilling. *International Journal of Advanced Manufacturing Technology*, *54*(5–8), 629–638. https://doi.org/10.1007/s00170-010-2971-1

Chan, J. (2023). 3D Reconstruction and Segmentation of Barely Visible Impact Damage in Composites from Pulse-Echo Ultrasonic C-Scans [Master's Thesis 3D Reconstruction and Segmentation of Barely Visible Impact Damage in Composites from Pulse-Echo Ultrasonic C-Scans]. https://escholarship.org/uc/item/1wp2k035

Delaney, M., & Hyonny K. (2026). Simultaneous Surface Contour Mapping and Internal Damage Detection Using Ultrasonic C-Scan Inspection. 4–5.

Ellison, A. C. (2020). Segmentation of X-ray CT and Ultrasonic Scans of Impacted Composite Structures for Damage State Interpretation and Model Generation. eScholarship, University of California.

Federal Aviation Administration. (2009). Advisory Circular: Composite Aircraft Structure (AC No. 20-107B). U.S. Department of Transportation.

Hall, N. (2021, May 13). Bernoulli's Equation. Www.grc.nasa.gov; NASA. https://www.grc.nasa.gov/WWW/K-12/airplane/bern.html

Hocheng, H. (2012). Machining Technology for Composite Materials - Principles and Practice (1st ed.). Woodhead Publishing. 17-64. https://doi.org/10.1533/9780857095145

Hocheng, H., & Tsao, C. C. (2005). The path towards delamination-free drilling of composite materials. *Journal of Materials Processing Technology*, *167*(2), 251–264. https://doi.org/10.1016/j.jmatprotec.2005.06.039

Huang, T., & Bobyr, N. I. (2023). A Review of Delamination Damage of Composite Materials. Journal of Composites Science, 7(11), 468–468. https://doi.org/10.3390/jcs7110468

Ismail, S. O., & Dhakal, H. N. (2017). Philosophical Study on Composites and Their Drilling Techniques. In V. K. Thakur & M. K. Thakur (Eds.), Functional Biopolymers (pp. 239–

280). Springer International Publishing AG. https://doi.org/10.1007/978-3-319-66417-0_9

Jain, S., & Yang, D. C. H. (1993). Effects of Feedrate and Chisel Edge on Delamination in Composites Drilling. Journal of Engineering for Industry, 115(4), 398–405. https://doi.org/10.1115/1.2901782

Latha, B., Senthilkumar, V. S., & Palanikumar, K. (2011). Influence of drill geometry on thrust force in drilling GFRP composites. Journal of Reinforced Plastics and Composites, 30(6), 463–472. https://doi.org/10.1177/0731684410397681

Lin, S. C., & Chen, I. K. (1996). Drilling carbon fiber-reinforced composite material at high speed. *Wear, 194*(1), 156–162. https://doi.org/10.1016/0043-1648(95)06831-7

Liu, Y., Huang, J., Wang, T., Sun, P., & Zhou, H. (2024). Thermo-mechanical coupled three-dimensional finite element simulation analysis of drilling thermoplastic braided carbon fiber composite and optimization of process parameters. *Thin-Walled Structures*, *204*, Article 112263. https://doi.org/10.1016/j.tws.2024.112263

Liu, Y., Li, Q., Qi, Z., & Chen, W. (2021). Scale-span modelling of dynamic progressive failure in drilling CFRPs using a tapered drill-reamer. *Composite Structures, 278,* Article 114710. https://doi.org/10.1016/j.compstruct.2021.114710

Macmanus, D., & Eaton, J. (1996, January 1). Micro-scale three-dimensional Navier-Stokes investigation of laminar flow control suction hole configurations. *American Institute of Aeronautics and Astronautics. AIAA Meeting Papers*.

Massey, J. T. (2023). Novel Quantitative Composite Delamination Injection Repair Procedure and Characterization for Strength Restoration. ProQuest Dissertations & Theses.

Perera, H. (2025). Evaluation of Low Viscosity Epoxy Repair Resins for Injection Repair of Delaminations in Composite Laminates / Hiruni Perera. University of California, San Diego.

Romasko, B. W. (2022). Flat Composite Panel Impact Testing and Characterization by Ultrasonic Non-destructive Evaluation. ProQuest Dissertations & Theses.

Seneviratne, W., Tomblin, J., & Saathoff, B. (2017). Foundations for Composite Fuselage Repair Methods FY2017 Final Report [Review of Foundations for Composite Fuselage Repair Methods FY2017 Final Report]. Kansas Aviation Research & Technology Growth Initiative (KART).

Shahabaz S.M, Shetty, N., Sharma, S., K, J. P., S. Divakara Shetty, & Naik, N. (2024). Optimization of Drilling Parameters on Delamination and Burr Formation in Drilling of Neat CFRP and Hybrid CFRP Nano-Composites. Materials Research Express. https://doi.org/10.1088/2053-1591/ad3522

Shahzad, H., Hickel, S., & Modesti, D. (2022). Permeability and Turbulence Over Perforated Plates. *Flow*, *Turbulence and Combustion*, *109*(4), 1241–1254. https://doi.org/10.1007/s10494-022-00337-7

Srinivasan, T., Palanikumar, K., Rajagopal, K., & Latha, B. (2017). Optimization of delamination factor in drilling GFR-polypropylene composites. *Materials and Manufacturing Processes*, *32*(2), 226–233. https://doi.org/10.1080/10426914.2016.1151038

Sun, C., & Saleh, M. N. (2024). 1 - An introduction to the impact damage of composite materials. In Non-destructive Testing of Impact Damage in Fiber-reinforced Polymer Composites (pp. 1–41). Elsevier Ltd. https://doi.org/10.1016/B978-0-443-14120-1.00001-7

Wei, Y. Y., Xu, J. Y., Cai, X. J., An, Q. L., & Chen, M. (2013). Effect of Drills with Different Drill Bits on Delamination in Drilling Composite Materials. Key Engineering Materials, 589-590, 173–178. https://doi.org/10.4028/www.scientific.net/kem.589-590.173

Wiggers de Souza, C. (2022). Damage Initiation, Progression and Modeling of High Energy Wide Area Blunt Impacts to Aircraft Structures. ProQuest Dissertations & Theses.

Zhao, J., Das, R., & Khatibi, A. A. (2023). Application of Acoustic Metamaterials in Pulse-Echo Ultrasonic Evaluation of Thick Hybrid Composite Laminates. Journal of Composites Science, 7(6), 257. https://doi.org/10.3390/jcs7060257